



HAL
open science

Tensor Network approaches to Open Quantum Systems at Finite Temperature with applications to Spectroscopy

Angus Dunnett

► **To cite this version:**

Angus Dunnett. Tensor Network approaches to Open Quantum Systems at Finite Temperature with applications to Spectroscopy. Quantum Physics [quant-ph]. Sorbonne Université, 2021. English. NNT : 2021SORUS318 . tel-03551506

HAL Id: tel-03551506

<https://theses.hal.science/tel-03551506v1>

Submitted on 1 Feb 2022

HAL is a multi-disciplinary open access archive for the deposit and dissemination of scientific research documents, whether they are published or not. The documents may come from teaching and research institutions in France or abroad, or from public or private research centers.

L'archive ouverte pluridisciplinaire **HAL**, est destinée au dépôt et à la diffusion de documents scientifiques de niveau recherche, publiés ou non, émanant des établissements d'enseignement et de recherche français ou étrangers, des laboratoires publics ou privés.

**THÈSE DE DOCTORAT
DE SORBONNE UNIVERSITÉ**

Spécialité : Physique

École doctorale n°564: Physique en Île-de-France

réalisée

à l'Institut des NanoSciences de Paris

sous la direction de Dr Alex Chin

présentée par

Angus DUNNETT

pour obtenir le grade de :

DOCTEUR DE SORBONNE UNIVERSITÉ

Sujet de la thèse :

**Décrire les systèmes quantiques ouverts à température
non-nulle à l'aide de Réseaux de Tenseurs avec application à
la Spectroscopie**

soutenue le 3 décembre 2021

devant le jury composé de :

Mme Susana HUELGA	Rapporteuse
M. Johannes SCHACHENMAYER	Rapporteur
Mme Michèle DESOUTER-LECOMTE	Examinatrice
M. Riccardo SPEZIA	Examinateur
M. David REICHMAN	Examinateur
M. Alex CHIN	Directeur de thèse

**Tensor Network approaches to Open Quantum Systems at
Finite Temperature with applications to Spectroscopy**

Contents

1	Introduction: Open Quantum Systems	1
1.1	Dynamics of Open Quantum Systems	2
1.2	Non-Markovian Methods	4
1.3	Outline of Chapters	5
2	Methods	7
2.1	Tensor Networks	7
2.1.1	Matrix-Product States	9
2.1.2	Matrix-Product Operators	11
2.1.3	Singular Value Decomposition	12
2.1.4	Canonical Forms	13
2.1.5	QR Decomposition	18
2.2	Time Evolution	19
2.2.1	Time-Dependent-Variational-Principle	22
2.2.2	Increasing the Bond Dimension	27
2.3	Tree-MPS	30
2.4	Tensor Networks for Open Quantum Systems	31
2.4.1	Chain mapping	33
2.4.2	Finite temperatures	34
2.5	Constructing MPOs	39
2.6	Code - MPSDynamics.jl	42
2.A	Appendix - Chain mapping	43
3	Models	47
3.1	Independent Boson Model	47
3.2	Spin-Boson Model	50
3.2.1	Thermalisation	52
3.2.2	Rabi Oscillations	53
3.2.3	Localisation Transition	56
3.3	Electron transfer	57
3.4	Two-bath Spin-Boson Model	63
3.4.1	Heat flow	64
3.5	Chain Dynamics	65

3.5.1	Performance for long-time dynamics	70
4	Linear Absorption Spectroscopy	77
4.1	Case Study: Methylene Blue	77
4.1.1	Brownian Oscillator Model	78
4.1.2	Linear Vibronic Coupling Model	82
4.1.3	Molecular Dynamics and Electronic Structure Calculations	83
4.1.4	Calculating the Response Function	84
4.1.5	Bath Correlations	87
4.1.6	Parameterising the Correlated LVC Hamiltonian	89
4.1.7	The Chain Mapping in the Correlated LVC model	90
4.1.8	Results	91
4.2	Conclusion	95
5	Adaptive 1TDVP	101
5.1	Method	102
5.1.1	Full QR Decomposition	102
5.1.2	Sub-space Expansion in the one-site Projector	103
5.1.3	Projection Error	105
5.1.4	Convergence criterion	107
5.1.5	Summary	109
5.2	Numerical Verification	109
5.3	Optimising the Sub-space Expansion	112
5.4	Conclusion	115
6	Conclusions and Prospects	119

To Kim

Acknowledgements

There are many people without whom the three and a bit years of work that went into this thesis would not have been possible, and many more without whom it may have been possible, but infinitely less fun.

First and foremost I wish to thank my supervisor, Alex, for a number of things: for giving me the opportunity to work on a project that I have found thoroughly rewarding and worthwhile; for your constant support and guidance, right from the beginning, when I arrived in Paris for the first time, clueless and bewildered, to the end; and for your indefatigable enthusiasm and good humour which have been my mainstay throughout this project.

Next I would like to thank our collaborators: Tim Zuehlsdorff, Christine Isborn and Duncan Gowland, who enabled us to take our work into the real world and without whom a whole chapter of this thesis would not exist. I would particularly like to thank Duncan for a number of enlightening exchanges which helped me to understand many things.

My time at the INSP would not have been the same without the all the people who surrounded me during my time there. At the heart of this group of people is my team, and I would like to extend a huge thanks to all the members of PHOCOS, past and present, for your friendship and support. In particular I would like to thank Thierry Barisien, Laurent Legrand, Maria Chamarro and Frederick Bernardot for welcoming me into the team and for making it the warm working environment that it is, and also for the help you have given me on countless occasions; Thibaut Lacroix for the many scientific and non-scientific discussions we have had and also for the help with the non-English parts of this manuscript; and Guadalupe for being such a wonderful office-mate and friend during my first year.

Beyond PHOCOS, I would like to thank all the support staff whose work is indispensable to everyone at the INSP. I also thank all of my fellow PhD students and post-docs, many of who: Mathis; Oliviero; Sunniva; Ronei; have become my good friends, and have defined my experience of life in Paris. I would especially like to thank all of the PhD representatives who have served throughout my time at the INSP: Clément Livache, Roman Delalande, Marine Bossert and Niccolo Avallone, for creating a sense of community and making me feel at home in a place that was initially unfamiliar and strange to me.

Finally, I could not have got through the last three years without the support of those who are closest to me: my family and Violette, thanks for everything.

Chapter 1

Introduction: Open Quantum Systems

Despite the passage of nearly a century since the quantum nature of matter at the smallest scales was unequivocally revealed, the goal of harnessing this, no longer new, physics and turning it to our advantage, remains, in large part, elusive. The full realisation of this goal would represent a ‘quantum revolution’ which would change the way we communicate securely, and transform the way we solve problems in science and engineering, and thus have dramatic and far-reaching effects on society. The difficulty of the problem stems from the fragile nature of the quantum state, which, upon the slightest external disturbance, will lose its vital property of coherence. Nonetheless, our ability to create and manipulate quantum states continues to advance steadily [1, 2, 3, 4], bringing the question of the nature of the interaction of a quantum system with its environment to the forefront of theoretical quantum research. This question is the subject of the theory of open quantum system (OQS).

Loss of coherence in a quantum system, known as *decoherence*, comes about as a result of the inevitable interaction of the system with its environment. By environment, we refer to all relevant degrees of freedom which are not part of the system. In principal, ‘all relevant degrees of freedom’ means everything; thus, environments are characterised by being large and complex. This interaction leads to the system’s states becoming entangled with the macroscopic states of the environment. Tracing out the environment’s degrees of freedom, we find that a certain set of system states (or sub-spaces) is selected, between which, any coherence decays extremely rapidly, while the states (or sub-spaces) themselves are stable. Strictly speaking then, decoherence, does not mean that the system loses the property of coherence; indeed, since the definition of coherence is dependent on the choice of basis, coherence can not even be called a *property*. Instead, since the observation of any non-trivial quantum effects, arising from coherence, requires driving the system out of its preferred basis, decoherence will lead to the loss of these quantum effects, or at least, a reduction of the time-scale over which such effects play a role.

A microscopic understanding of decoherence, and, what often accompanies it, dis-

sipation, can provide insights into how these processes might be suppressed, or even exploited [5] in potential applications. For example, a proper treatment of decoherence and dissipation is key to understanding the process of singlet fission [6] which offers the possibility of solar cells that surpass the Shockley-Queisser limit [7]. In addition, ultra-fast spectroscopic measurements of the photosynthetic Fenna-Mathews-Olson complex, have raised the fascinating possibility that long-lived (~ 1 ps) electronic coherences are able to exist in the warm and noisy environment of biological cells [8], suggesting that natural selection might have invented solutions for slowing decoherence and exploiting quantum effects. And although the reality of these coherences, and whether, if they are real, they have any function, remain hotly debated subjects [9, 10], the possibility of quantum effects at non-cryogenic temperatures has ignited intense interest in the question of how the system-environment interaction could be engineered to preserve coherence and how such coherence could be exploited [11].

Decoherence is also of *fundamental* importance, since it forms the basis of the dynamical theory of quantum measurement [12]. The measurement process consists of the interaction between the system and a probe which are both coupled to an environment. The state of the probe is assumed to be known to the experimenters. The coupling of the system to the probe leads to their states becoming entangled. Following this, the interaction with the environment leads to the selection of a measurement basis (often referred to as a *pointer basis*), consisting of products of system and probe states. The environment degrees of freedom are inaccessible to experiment and so must be traced out. On doing this, we find that the system and probe are described by a statistical mixture of the measurement basis states, representing the probabilistic outcome of an experiment. The system and probe states are perfectly correlated, allowing the system's state to be inferred by reading the state of the probe. The theory of quantum measurement provides insight into the foundations of quantum mechanics, although does not allow us to solve the famous 'measurement problem', because it does not provide a mechanism by which the system and probe evolve into a *specific* state of the measurement basis, which is of course what happens during an experimental measurement.

1.1 Dynamics of Open Quantum Systems

As alluded to above, in OQS theory one assumes that the total Hilbert space \mathcal{H} can be partitioned into a sub-space called the 'system' \mathcal{H}_S and a sub-space called the 'environment' \mathcal{H}_E , where $\mathcal{H} = \mathcal{H}_S \otimes \mathcal{H}_E$. The system typically consists of just a few degrees of freedom and represents what is accessible to an experiment. The environment on the other hand, is unobservable and very large, containing a practically infinite number of degrees of freedom. The system is never truly isolated from its environment but is coupled to it via what is known as the interaction Hamiltonian \hat{H}_I , which operates in the global Hilbert space $\hat{H}_I \in \mathcal{H}$. It is usually assumed that the combined system+environment, which we will refer to as S+E, is closed and thus undergoes unitary evolution described by a Hamiltonian

$$\hat{H} = \hat{H}_S \otimes \mathbb{1}_E + \hat{H}_I + \hat{H}_E \otimes \mathbb{1}_S, \quad (1.1)$$

where \hat{H}_S and \hat{H}_E are, respectively, the free Hamiltonians of the system and the environment, and $\mathbb{1}_S$ and $\mathbb{1}_E$ are the identities of the Hilbert spaces \mathcal{H}_S and \mathcal{H}_E . One could also include an explicit time dependence in \hat{H} although this will not be necessary for our purposes. This situation is represented schematically in Fig. 1.1.

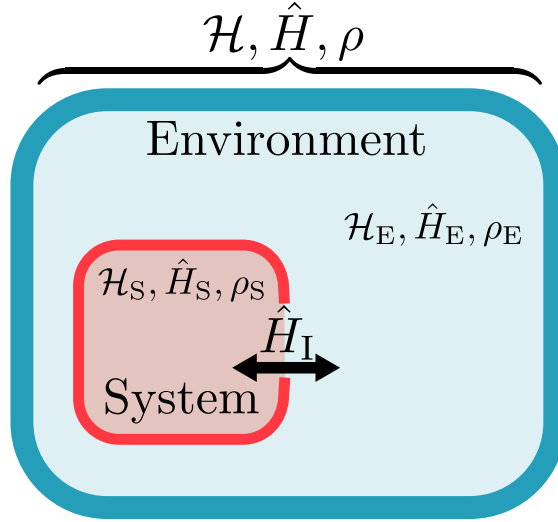


Figure 1.1: An open quantum system

The state of S+E at a time t is described by the density operator $\rho(t)$. This density operator undergoes unitary evolution in the Schrodinger picture governed by $U(t)$:

$$\rho(t) = U(t)\rho(0)U^\dagger(t), \quad (1.2)$$

where

$$U(t) = e^{-i\hat{H}t}. \quad (1.3)$$

Since the system, S, is the only part which is observable, the outcome of any experiment is described by the system's *reduced density operator* ρ_S obtained by performing the *partial trace* over the environment's degrees of freedom:

$$\rho_S = \text{Tr}_E \{ \rho \}. \quad (1.4)$$

The goal of OQS theory is to find out how the system's reduced density operator evolves in time. Formally, the solution is given by

$$\rho_S(t) = \text{Tr}_E \left\{ U(t-t_0)\rho(t_0)U^\dagger(t-t_0) \right\}. \quad (1.5)$$

The combined function given by Eq. (1.5), consisting of the unitary transformation followed by the partial trace, defines what is known as a dynamical map $V(t, t_0)$, which describes how the system changes over time, incorporating the bare system dynamics with the environment-induced decoherence and dissipation:

$$\rho_S(t) = V(t, t_0)\rho_S(t_0). \quad (1.6)$$

In general $V(t, t_0)$ can be highly complex. The difficulty of obtaining $V(t, t_0)$ exactly arises from the sheer size of the environment; one cannot simply evaluate Eq. (1.5) by applying the unitary transformation and taking the partial trace since the dimension of $U(t)$ and $\rho(t)$ is, in principle, infinite. Furthermore, in many cases the environment is just too complex for its Hamiltonian to even be known.

On the other hand, in situations, such as those often encountered in quantum optics, where a separation of timescales exists between the dynamics of the system and those of the environment, $V(t, t_0)$ may actually be quite simple. In particular, when the relaxation time of the environment is very fast compared to the timescale over which the system's state changes, $\rho_S(t)$ can be determined as the solution to a time-local equation known as a *master equation* [13, 12, 14, 15, 16]. Under these assumptions the OQS is said to be *Markovian*. A precise definition of Markovianity for a quantum system is more difficult to obtain than for a classical one [17] but the concept can be intuitively understood in the following way. In a Markovian OQS the environment is *memory-less* in the sense that it quickly ‘forgets’ the past state of the system since any perturbation that the system produces in the environment decays rapidly, and will be gone before the system state has changed (See Fig. 1.2(a)). The dynamics of a *non-Markovian* system, on the other hand will be much more involved as the environment ‘remembers’ the previous states of the system, meaning that the system's evolution depends not just on its current state but also on its entire *history* (See Fig. 1.2(b)). This assumption of Markovianity is very severe and, when applied to systems with long coherence times, is likely to miss some of the most interesting physics [18, 19].

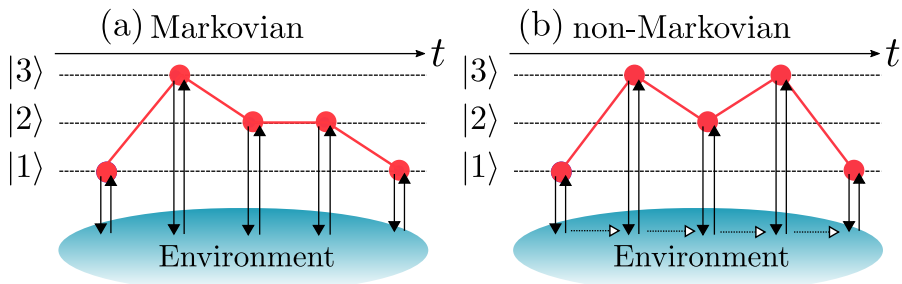


Figure 1.2: Markovian versus non-Markovian open quantum systems. In a Markovian OQS, information about the system is quickly lost in the environment due to its fast relaxation time, leading to a time-local evolution for the system. In non-Markovian OQS on the other hand, the environment ‘remembers’ the system's history.

1.2 Non-Markovian Methods

Many techniques, including master equations, which go beyond the Markov approximation have been developed, and an excellent review can be found in Ref. [20].

Here we will mainly be interested in numerically exact methods. Such methods typically assume that the environment can be modelled as a bosonic bath which is

initially in a Gaussian state and is linearly coupled to the system. One prominent approach is the hierarchical of equation of motions (HEOM) method [21, 22, 23, 18, 24] in which one solves Eq. (1.5) by deriving an infinite set of equations of motions from the Feynman-Vernon influence functional [25]. This infinite set of equations has a hierarchical structure which may be terminated at a certain depth, chosen to ensure convergence.

Another approach which is based on the influence functional formalism, is the quasi-adiabatic path integral (QUAPI) [26, 27]. The idea of this approach is to consider a discrete set of time steps and evaluate the path integral as though one were propagating an object known as the augmented density tensor (ADT), which describes, not only the system's current state but also its *history*. Since the system's history stretches further back in time upon each time step, the ADT grows in size as it evolves. However, thanks to the product structure of the influence functional under the assumption of a Gaussian bath, there exists a natural basis for truncating the ADT propagator. This is to assume that the memory of the bath is finite such that any contributions to the influence functional which look further back in time than a chosen cut-off, can be ignored. Such an approach is extremely interesting as its numerical cost is directly linked to the non-Markovianity of the problem. Unfortunately, even with the finite memory approximation, the size of the ADT limits this approach to small systems with short memory times. It was only when tensor network methods were introduced, via the identification of the underlying matrix-product state (MPS) structure of the influence functional, to form the time-evolving matrix-product operator (TEMPO) method [28], that this approach has become a practical alternative [29].

Both of the non-Markovian methods described above are based on computing $\rho_S(t)$ directly, without at any point needing to deal with the full S+E density operator ρ . They achieve this by making analytical progress in formally tracing out the environment ahead of any numerical evaluation. This approach makes sense from the traditional open systems point of view which assumes that environmental degrees of freedom are unobservable and therefore of no use. However, in complex molecular systems, drawing the boundary between the 'system' and the 'environment' can often be rather arbitrary [5]. In such cases it is desirable to have access to the full density matrix ρ [30, 6]; thus, the open system problem becomes the many-body problem. Of course, a numerical solution to the many-body problem in quantum mechanics is only possible if one is able to find an efficient reduced description of the state. The Multi-Layered Multi-Configurational Time-Dependent Hartree (ML-MCTDH) method [31] is an example of such a many-body approach to OQS, which is particularly widely used in the field of theoretical chemistry.

In this thesis we will follow the many-body approach, however our means of reducing the state space will be the powerful tensor network methods which were evoked above.

1.3 Outline of Chapters

The material of this thesis is organised as follows. In chapter 2 we will introduce the methods, starting with a somewhat pedagogical development of the concept of a tensor

network, focusing on matrix-product states, and then moving on to time evolution. A particular attention has been paid to introducing these concepts because they will be relied upon later in chapter 5. We also present the chain mapping technique and the innovation by Tamascelli et al. which has lead to these methods becoming applicable at finite temperatures. Then, in chapter 3 we present results for a range of model OQS problems in non-perturbative regimes and at finite temperatures. In chapter 4 we move beyond model systems to a theoretical study of the absorption of Methylene blue in water. This is where the real power of our methodology will be demonstrated. Finally, in chapter 5 we present some work towards improving the underlying time evolution methods that we have made use of, with a particular focus on open quantum systems.

Chapter 2

Methods

In this chapter we will set out the tensor network methods that will be central to this thesis.

2.1 Tensor Networks

In this section we will introduce the notion of a tensor network (TN) and establish the diagrammatic notation which will be used throughout this thesis. We use the term ‘tensor’ here in the sense of an n -dimensional array of complex numbers, rather than to imply any kind of transformation properties. The tensor *rank* (not to be confused with the rank of a matrix) will here refer to the number of indices of the tensor; thus, a rank-0 tensor is a scalar, a rank-1 tensor is a vector, and a rank-2 tensor is a matrix. Tensors can be represented diagrammatically in the following way

$$v_i = \begin{array}{c} | \\ \circ \\ | \end{array}, \quad A_{ij} = \begin{array}{c} | \\ \circ \\ | \end{array}, \quad T_{ijk} = \begin{array}{c} | \\ \circ \\ | \end{array} \text{---}, \quad \text{etc}, \quad (2.1)$$

where each ‘leg’ corresponds to an index of the tensor. In this way we can easily express tensors of arbitrary rank. Where necessary, legs will be labelled to show which tensor indices they correspond to. The rank of a tensor represented in this way can be determined by simply counting the number of legs. Each leg of a tensor has a property known as the *dimension* which is equal to the number of values that the index to which it refers can take.

Almost all operations that we will want to perform between tensors can be cast in terms of *contractions*. A contraction is an operation in which a pair of indices, either on the same tensor or across two different tensors, *annihilate* one another, as a result of being *summed over*. A familiar example of a contraction is the product of a matrix and a vector

$$\sum_{\beta=1}^D A_{\alpha\beta} v_{\beta} = u_{\alpha}. \quad (2.2)$$

Here, we sum over the index β , corresponding to the column index of the matrix A and

row index of the vector v . The index β is absent from the resulting vector which only has one index α corresponding to the row index of A which was not summed over.

The real power of the diagrammatic notation introduced above lies in its ability to express contractions. Instead of writing Eq. (2.2) we can represent the same operation with

$$\text{---} \bigcirc A \text{---} \bigcirc v = \text{---} \bigcirc u, \quad (2.3)$$

where we understand the joining of the two legs as meaning ‘sum over that index’. Whenever two legs are joined together in this way it will be referred to as a *bond*. Two legs may only be joined if their dimensions are the same. The dimension of the two legs which make up a bond is known as the *bond dimension*. For example, in Eq. (2.3) the bond dimension is D . Some common operations in linear algebra are given in diagrammatic form below:

$$\text{vector-vector scalar product: } \bigcirc \text{---} \bigcirc; \quad (2.4)$$

$$\text{matrix-matrix product: } \text{---} \bigcirc \text{---} \bigcirc \text{---}; \quad (2.5)$$

$$\text{matrix trace: } \bigcirc \text{---} \bigcirc. \quad (2.6)$$

In this manner we may express tensor contractions of arbitrary complexity in an intuitive and easy-to-read way. A more complicated example could be:

$$\sum_{\beta\gamma\delta\nu\mu=1}^{\chi} A_{\alpha\beta\gamma\delta} B_{\delta\nu} C_{\gamma\mu\nu} D_{\beta\omega\mu} = \text{---} \bigcirc A \text{---} \bigcirc B \text{---} \bigcirc C \text{---} \bigcirc D \text{---} \bigcirc \omega. \quad (2.7)$$

Every summed over index is represented as a bond while the other indices correspond to the *free* legs, i.e. legs which are not joined to form bonds. In Eq. (2.7) we have explicitly labelled all the legs with their dimensions along with the indices they correspond to. We make use of the convention that labels for dimensions will appear in the middle of the leg, while labels for indices will appear next to the leg.

By writing tensor contractions in this way one can immediately determine the rank of the resulting tensor simply by counting the number of free legs. In the above example the result of the contraction will be a rank-2 tensor (a matrix) since there are two free legs. In Eq. (2.4) and (2.6), on the other hand, there are no free legs and thus the result is a scalar.

Equation (2.7) is an example of what is known as a *tensor network* [32]; that is, a collection of tensors along with a specification for how their indices should be contracted. The diagrammatic notation used to define a tensor network is known as a *tensor network diagram*. While a tensor network may always be contracted to form a single tensor by

carrying out the summations prescribed by its bonds, it is often extremely useful, as we shall later see, not to immediately perform these contractions but instead to consider the tensor network as an algebraic object in its own right.

2.1.1 Matrix-Product States

Considering thus, a tensor network as its own algebraic object, one may immediately conceive of the vast variety of forms that such an object may take; and indeed this variety is mirrored in the scope of their applications across the fields of physics [32], mathematics [33, 34] and computer science [35, 36]. For more than fifty years, physicists have known of a class of tensor network that offer a powerful representation for quantum states. These so called Matrix-Product States (MPS), were first employed as a tool for analytical studies of quantum lattices [37] and were later recognised as defining a class of states known as finitely correlated states [38]. A key development in the history of MPS in physics was the proof that the ground state of the AKLT (Affleck, Kennedy, Lieb and Tasaki) Hamiltonian could be expressed exactly by an MPS [39].

However, the full power of MPS, and more generally tensor network states (TNS), in physics, was not realised until the identification of the underlying MPS structure of White's Density Matrix Renormalisation Group (DMRG) method [40, 41] for finding ground states of 1D Hamiltonians. The identification, and later reformulation of DMRG in terms of MPS [42, 43, 44, 45], paved the way for numerous extensions to the DMRG algorithm which would have been difficult to conceive of without the language and way of thinking brought by MPS and TNS. Indeed, since TNS have been established as a tool in quantum science they have inspired burgeoning interest and have been applied to areas including but not limited to: real-time evolution [46, 47], fermionic systems [48, 49, 48], continuous states [50], tree structured systems [49, 51], and 2D and 3D systems [52, 53].

An MPS is an ansatz for a many-body wave function. Consider a many-body quantum system consisting of N coupled systems, each consisting of d states $\{|1\rangle, |2\rangle, \dots, |d\rangle\}$. The Hilbert space for such a system has d^N basis vectors of the form $|i_1\rangle \otimes |i_2\rangle \otimes \dots \otimes |i_N\rangle$, corresponding to all the ways of occupying N distinguishable d level systems. We can express a generic wave function in this basis as follows:

$$|\psi\rangle = \sum_{i_1, i_2, \dots, i_N=1}^d c_{i_1, i_2, \dots, i_N} |i_1\rangle \otimes |i_2\rangle \otimes \dots \otimes |i_N\rangle. \quad (2.8)$$

Each sub-system contributes an index that must be independently summed over and thus adds a multiplicative factor to the number of basis states. This exponential growth in the Hilbert space dimension with system size is a fundamental feature of quantum mechanics and marks a profound contrast to classical mechanics, in which the state space dimension grows linearly with system size. This feature represents, at the same time, the promise of quantum states for use in computation, and, more pertinently to the present work, the barrier to storing and simulating them on classical computers .

We see from Eq. (2.8) that all the information required to describe a generic wave function in this large Hilbert space is contained in the object c_{i_1, i_2, \dots, i_N} which we recognise as being nothing more than a rank- N tensor. This observation gives us a means of using the diagrammatic notation introduced above to express the wave function:

$$|\psi\rangle = \text{---} \overbrace{\text{---} \text{---} \text{---} \text{---} \text{---} \text{---} \text{---}}^c \text{---} \quad (2.9)$$

$i_1 \quad i_2 \quad i_3 \quad \dots \quad i_{N-1} \quad i_N$

Each of the free legs of the tensor c represents an index which runs over the d states of one of the N sub-systems of our total system. We will refer to this kind of leg as a *physical leg* because it runs over a set of physical states. The tensor c stores all the d^N coefficients required to describe ψ ; by selecting values between 1 and d for each of the N sub-systems we pick out one of the d^N basis states, and by fixing these values for the physical legs of c we obtain the complex number coefficient for that state.

Describing the wave function in this way, we are extremely limited by the size of N . Suppose we wished to consider a chain of N spin- $\frac{1}{2}$ s. In this case we would have $d = 2$ and the tensor c would contain 2^N complex numbers. Even for the modest value of $N = 30$ we would need 8Gb of memory in order to store the 2^N complex numbers with standard floating point precision, and that capacity would need to increase by a factor of 2 for every further spin that we add. By the time N reached 160, we could just about store the state if we were able to write a bit on every atom on earth.

We may ask however whether such a dense description of the state is really necessary; after all, the description above applies to *any* wave function ψ , and one is rarely interested in *any* wave function but rather the specific wave functions which are likely to appear as states of real physical systems.

The MPS ansatz consists of replacing c with the following tensor network:

$$|\psi\rangle = \text{---} 1 \text{---} \bigcirc_{A^1} \text{---} D_1 \text{---} \bigcirc_{A^2} \text{---} D_2 \text{---} \bigcirc_{A^3} \text{---} \dots \text{---} \bigcirc_{A^{N-1}} \text{---} D_{N-1} \text{---} \bigcirc_{A^N} \text{---} 1 \text{---} , \quad (2.10)$$

$i_1 \quad i_2 \quad i_3 \quad \dots \quad i_{N-1} \quad i_N$

where now, instead of one rank- N tensor, we have N tensors A^j which each have a rank of 3. We refer to the tensors A^j as *sites* of the MPS. In addition to a physical leg, each MPS site has two legs which are often referred to as *virtual legs* (because not physical). For uniformity, we have added *dummy* legs with dimension 1 to the end sites. The MPS has a set of bond dimensions $\{D_1, D_2, \dots, D_{N-1}\}$. It is often convenient to characterise the MPS by its largest bond dimension; thus we define the *MPS bond dimension* as being $D_{\max} = \max\{D_1, D_2, \dots, D_{N-1}\}$.

The physical legs of the MPS in Eq. (2.10) are the same as for the tensor c and so this tensor network also serves as a description for ψ . However, instead of having to store a separate complex number for every possible basis state, the coefficient for a particular set of physical indices $(i'_1, i'_2, \dots, i'_N)$ is given by the *product* of matrices (hence

matrix-product state) defined by Eq. (2.10) when one sets the selected values for the physical legs:

$$\langle i'_1, i'_2, \dots, i'_N | \psi \rangle = \text{Tr} \left[A^1(i_1 = i'_1) A^2(i_2 = i'_2) \cdots A^N(i_N = i'_N) \right]. \quad (2.11)$$

The result of the above contraction is a 1×1 matrix, i.e. a (complex) number.

Extracting a coefficient from an MPS thus requires a small amount of computation, in contrast to the description in terms of c where the coefficient is simply stored. However, given that matrix multiplications are perhaps the fastest algebraic operations that can be performed on a computer, this is a small price to pay for the reduction in memory required to store ψ . Assuming for simplicity that all the bond dimensions are the same ($D_i = D$), the number of complex numbers needed to store the MPS is just ND^2d , which grows linearly in N ! Of course, this size still depends on D and we do not yet know how large D will be and whether it will itself depend on N . Indeed if $D \sim \exp(N)$ all will be lost. However, in section 2.1.4 we shall show that D is related to how entangled ψ is, and so by restricting ourselves to states with relatively low entanglement, we can use an MPS to store the wave function of very large systems using a computationally viable number of parameters [54].

2.1.2 Matrix-Product Operators

In perfect analogy with MPS, one may express an operator using a similar TN structure, called a Matrix-Product Operator (MPO):

$$\hat{O} = \text{Tr} \left[M^1 M^2 M^3 \cdots M^N \right]. \quad (2.12)$$

Each MPO site tensor has two physical indices since contracting all the bonds of an MPO should yield a matrix. Again, we add dummy indices on the two end sites for uniformity. We use the convention that a downward pointing leg corresponds to the ket and an upward pointing leg corresponds to the bra. Thus, applying this MPO to an MPS would look like:

$$\hat{O} |\psi\rangle = \text{Tr} \left[A^1 A^2 A^3 \cdots A^N \right]. \quad (2.13)$$

Of course, if $m = n$ the forms 2.18 and 2.20 coincide.

Strictly speaking, the above definition is for a version of the SVD known as the *thin*, or sometimes, the *compact* SVD. There is also a version called the *full* SVD, which we will not use here, but which we will mention later on.

2.1.4 Canonical Forms

By iteratively performing SVDs along an MPS, we may put it into a number of useful gauges. For example, starting from an MPS in an arbitrary gauge, we may proceed as follows:

$$|\psi\rangle = \text{reshape} \left[\begin{array}{c} \text{---} A^1 \text{---} A^2 \text{---} A^3 \text{---} A^4 \text{---} A^5 \text{---} \\ | \\ | \\ | \\ | \\ | \end{array} \right] \quad (2.21)$$

$$= \text{SVD} \left[\begin{array}{c} \text{---} A^1 \text{---} A^2 \text{---} A^3 \text{---} A^4 \text{---} A^5 \text{---} \\ | \\ | \\ | \\ | \\ | \end{array} \right] \quad (2.22)$$

$$= \text{contract} \rightarrow A^2 \left[\begin{array}{c} L^1 \text{---} S \text{---} V \text{---} A^2 \text{---} A^3 \text{---} A^4 \text{---} A^5 \text{---} \\ | \\ | \\ | \\ | \\ | \end{array} \right] \quad (2.23)$$

$$= \text{reshape} \left[\begin{array}{c} L^1 \text{---} A^2 \text{---} A^3 \text{---} A^4 \text{---} A^5 \text{---} \\ | \\ | \\ | \\ | \\ | \end{array} \right] \quad (2.24)$$

$$= \left[\begin{array}{c} L^1 \text{---} A^2 \text{---} A^3 \text{---} A^4 \text{---} A^5 \text{---} \\ | \\ | \\ | \\ | \\ | \end{array} \right] \cdot \quad (2.25)$$

In going from (2.21) to (2.22) we have ‘reshaped’ the tensor A^1 so that its left bond and the physical leg are combined into one ‘thick’ leg whose dimension will be the product of the left bond dimension and the physical dimension.

Repeating steps 2.21 through 2.25 starting from A^2 and so on until the end of the chain, we obtain an MPS in the *left canonical gauge*:

$$|\psi\rangle = \left[\begin{array}{c} L^1 \text{---} L^2 \text{---} L^3 \text{---} L^4 \text{---} L^5 \text{---} \\ | \\ | \\ | \\ | \\ | \end{array} \right] \cdot \quad (2.26)$$

We refer to the sites L^j as being *left normalised* or sometimes *left orthogonal*. One may wonder what happened to the S and V matrices from the last site, however, remembering

that the first and final bond dimensions are 1, we see that these matrices must contain only one element, and, provided the MPS is normalised ($\langle\psi|\psi\rangle = 1$), this element will just be the number 1.

Of course, we could equally have started from the right. In which case we would have obtained an MPS in the *right canonical gauge*:

$$|\psi\rangle = \begin{array}{c} \leftarrow R^1 \text{---} R^2 \text{---} R^3 \text{---} R^4 \text{---} R^5 \rightarrow \\ | \quad | \quad | \quad | \quad | \end{array} , \quad (2.27)$$

where the sites R^j are *right normalised* or *right orthogonal*.

In Eq. (2.22) we have written the right leg of A^1 as thicker than its left, indicating that the SVD will have the form of Eq. (2.18). This highlights an important point regarding MPS which is the following: for any MPS site with physical dimension d , and right and left bond dimensions D_R and D_L , we will always have $dD_L \geq D_R$. This is because the MPS sites act like *basis rotations and truncations*: an MPS site tensor takes in D_L states from its left, combines them with its own d states to make dD_L states, and outputs D_R linear combinations of these dD_L states to the next site along the chain to its right. Clearly then, the site tensor may not output more than dD_L states to its right; however, and herein lies the whole utility of the MPS, it may output *fewer*. Indeed, one can think of the D_R output states as representing the most *relevant* linear combinations of the dD_L input states. This enables the MPS to approximate the wave function to a high degree of accuracy whilst throwing away unimportant information. Of course, how many states we need to keep will depend on ψ and also on how accurate we want to be. We will return to this point later. We note for the moment that if no states are thrown away by the MPS site tensors, the MPS is capable of describing *any* wave function in the full d^N dimensional Hilbert space. In this case however, D would grow exponentially along the chain and so we would gain nothing by using an MPS instead of the tensor c in Eq. (2.8). Nevertheless, it is useful to know that by increasing the bond dimension we should always be able to converge to the right result.

Obviously, an MPS cares nothing for our notions of ‘left’ and ‘right’ and so the above argument is equally true if we replace L for R and R for L everywhere. Thus, when we start performing SVDs from the right of the MPS our SVD will look like Eq. (2.20).

Starting from an MPS in the right canonical gauge we can form the so called *mixed canonical gauges*:

$$|\psi\rangle = \text{reshape} \left[\begin{array}{c} \text{---} R^1 \text{---} R^2 \text{---} R^3 \text{---} R^4 \text{---} R^5 \text{---} \\ | \quad | \quad | \quad | \quad | \end{array} \right] \quad (2.28)$$

$$= \text{SVD} \left[\begin{array}{c} \text{---} R^1 \text{---} R^2 \text{---} R^3 \text{---} R^4 \text{---} R^5 \text{---} \\ | \quad | \quad | \quad | \quad | \end{array} \right] \quad (2.29)$$

$$= \text{reshape} \left[\begin{array}{c} \text{---} L^1 \text{---} S \text{---} V \text{---} R^2 \text{---} R^3 \text{---} R^4 \text{---} R^5 \text{---} \\ | \quad | \quad | \quad | \quad | \quad | \quad | \end{array} \right] \quad (2.30)$$

$$= \text{contract} \rightarrow A_C^2 \left[\begin{array}{c} \text{---} L^1 \text{---} S \text{---} V \text{---} R^2 \text{---} R^3 \text{---} R^4 \text{---} R^5 \text{---} \\ | \quad | \quad | \quad | \quad | \quad | \quad | \end{array} \right] \quad (2.31)$$

$$= \begin{array}{c} \text{---} L^1 \text{---} A_C^2 \text{---} R^3 \text{---} R^4 \text{---} R^5 \text{---} \\ | \quad | \quad | \quad | \quad | \end{array} \quad (2.32)$$

The site A_C^2 is known as the *orthogonality centre* (OC) as all sites to its left are left orthogonal and all sites to its right are right orthogonal. By repeating steps 2.28 through 2.32 starting from A_C^2 and iterating, the OC may be placed on any site of the MPS.

Instead of contracting S , V and R^2 into one site, we may have done the following starting from step 2.31:

$$= \text{contract} \rightarrow R_7^2 \left[\begin{array}{c} \text{---} L^1 \text{---} S \text{---} V \text{---} R^2 \text{---} R^3 \text{---} R^4 \text{---} R^5 \text{---} \\ | \quad | \quad | \quad | \quad | \quad | \quad | \end{array} \right] \quad (2.33)$$

$$= \begin{array}{c} \text{---} L^1 \text{---} S \text{---} R^2 \text{---} R^3 \text{---} R^4 \text{---} R^5 \text{---} \\ | \quad | \quad | \quad | \quad | \quad | \end{array} \quad (2.34)$$

In this gauge the OC is the ‘bond-centred’ diagonal matrix S which has no physical index. Again, by iterating, we may place S between any two sites.

The elements along the diagonal of the S matrices in the mixed canonical gauge correspond to the Schmidt coefficients λ_i of the bi-partition of the system at the point

where S is situated. Note that this is only true in the *mixed* canonical gauge, i.e., when all the site tensors to the left of S are left normalised and all the site tensors to its right are right normalised. The Schmidt coefficients are in turn related to the von Neumann entropy via

$$S_v = - \sum_i \lambda_i^2 \log(\lambda_i^2), \quad (2.35)$$

which is a measure of entanglement between the two parts of the system separated by the partition. We observe that if S is on a bond with bond dimension D the number of Schmidt coefficients will be equal to D . This observation may be used to derive a relation between the dimension of a bond and the maximum entanglement that can exist between the two sub-systems linked by that bond. Noting that the Schmidt coefficients must be non-negative, the maximum value of S_v will be obtained when all the Schmidt coefficients are equal ($\lambda_i = \lambda \forall i$). Further noting that the Schmidt coefficients are constrained by $\sum_{i=1}^D \lambda_i^2 = 1$, we see that $\lambda_i^2 = \frac{1}{D} \forall i$. Substituting this value into Eq. (2.35) we find that the maximum entanglement between two sub-systems linked by a bond with dimension D is

$$\max(S_v) = \log(D). \quad (2.36)$$

Reversing Eq. (2.36), we have

$$D \geq \exp(S_v), \quad (2.37)$$

which tells us that the minimum MPS bond dimension required to represent a wave function exactly is determined by how strongly the individual sub-systems are entangled.

This relation gives us a physical criterion for the suitability of the MPS ansatz for a particular a wave function. In order for the MPS ansatz to be efficient we require that the bond dimension D grow sub-exponentially with N . We may also be stricter and require that the D is constant in N such that the memory required to store the MPS grows linearly with N . Applying Eq. (2.37), this requirement becomes that the entropy of entanglement of a bi-partition be constant in N ,

$$S_v \sim \text{const.} \quad (2.38)$$

Equation (2.38) is in fact a special case of a more general condition known as the *area law* [55]. The area law states that the entropy of entanglement between two sub-systems is proportional to the *area of the boundary* that separates them; thus, in one dimension, when the boundary of the two sub-systems is zero-dimensional, the entropy of entanglement is independent of the sizes of the two sub-systems, i.e., independent of N . In two dimensions, the area of the boundary would grow linearly with system size and in three dimensions, quadratically. The class of states which obey the area law are known as area law states; it is sufficient for a state to belong to this class in order for the MPS ansatz to be efficient. It is known that the ground states of local, gapped, 1D Hamiltonians are area law states [56, 57]. Another class of states are the volume law states, whose entanglement entropy grows with the *volume* of the separated sub-systems. In 1D this would mean that $S_v \sim N$ and thus $D \geq \exp(N)$; so, volume law states cannot be efficiently represented by an MPS.

Often our goal in using an MPS will not be to represent a wave function *exactly* but instead to provide a good approximation. For this, the MPS ansatz is applicable outside the class of area law states.

We conclude this section by presenting the construction of a final gauge known simply as the *canonical gauge*. We start from an MPS in a mixed canonical gauge with the OC between the first and second site, as in Eq. (2.34) and perform SVDs as follows:

$$|\psi\rangle = \begin{array}{c} \text{contract} \rightarrow A^2 \\ \text{---} L^1 \text{---} S_1 \text{---} R^2 \text{---} R^3 \text{---} R^4 \text{---} R^5 \end{array} \quad (2.39)$$

$$= \begin{array}{c} \text{reshape} \\ \text{---} L^1 \text{---} A^2 \text{---} R^3 \text{---} R^4 \text{---} R^5 \end{array} \quad (2.40)$$

$$= \begin{array}{c} \text{SVD} \\ \text{---} L^1 \text{---} A^2 \text{---} R^3 \text{---} R^4 \text{---} R^5 \end{array} \quad (2.41)$$

$$= \begin{array}{c} \text{reshape} \quad \text{contract} \rightarrow R^3 \\ \text{---} L^1 \text{---} L^2 \text{---} S_2 \text{---} V \text{---} R^3 \text{---} R^4 \text{---} R^5 \end{array} \quad (2.42)$$

$$= \begin{array}{c} \text{---} L^1 \text{---} L^2 \text{---} S_2 \text{---} R^3 \text{---} R^4 \text{---} R^5 \end{array} \quad (2.43)$$

$$= \begin{array}{c} \text{contract} \rightarrow \Gamma^2 \\ \text{---} L^1 \text{---} S_1 \text{---} S_1^{-1} \text{---} L^2 \text{---} S_2 \text{---} R^3 \text{---} R^4 \text{---} R^5 \end{array} \quad (2.44)$$

$$= \begin{array}{c} \text{---} L^1 \text{---} S_1 \text{---} \Gamma^2 \text{---} S_2 \text{---} R^3 \text{---} R^4 \text{---} R^5 \end{array} \quad (2.45)$$

then, shifting one site to the right and repeating steps (2.39) through (2.44)...

$$= \begin{array}{c} \text{---} L^1 \text{---} S_1 \text{---} \Gamma^2 \text{---} S_2 \text{---} \Gamma^3 \text{---} S_3 \text{---} \Gamma^4 \text{---} S_4 \text{---} R^5 \end{array} . \quad (2.46)$$

In the canonical gauge the Schmidt coefficients are immediately available for every possible partition via the matrices S^j . In addition, every site can be made either left or right normalised by contracting the tensor Γ^j with the S matrix to its left or its right respectively:

$$\begin{array}{c} \text{---} \Gamma^j \text{---} S^j \text{---} \\ | \\ \text{---} R^j \text{---} \end{array}; \quad \begin{array}{c} \text{---} S^j \text{---} \Gamma^j \text{---} \\ | \\ \text{---} L^j \text{---} \end{array}. \quad (2.47)$$

There are numerous reasons for wanting to cast an MPS into one of the canonical gauges introduced above. For example, the orthogonality properties of the site tensors can be used as a short cut to computing expectation values of observables. Take the expectation value of the one site operator \hat{O}_j which is an operator that acts only on the site j . To calculate the expectation $\langle \psi | \hat{O}_j | \psi \rangle$ where $|\psi\rangle$ is expressed as an MPS, we would in general have to contract the following tensor network

$$\langle \psi | \hat{O}_j | \psi \rangle = \begin{array}{c} \dots \text{---} \text{---} \text{---} A^j \text{---} \text{---} \text{---} \dots \\ | \quad | \quad | \quad | \quad | \\ \dots \text{---} \text{---} \text{---} A^j \text{---} \text{---} \text{---} \dots \\ \quad \quad \quad \text{---} O \text{---} \end{array}; \quad (2.48)$$

where, in constructing the bra, it is implicit in Eq. (2.48) that the elements of the MPS site tensors have been complex conjugated. However, if the MPS is in the canonical gauge this reduces to

$$\langle \psi | \hat{O}_j | \psi \rangle = \begin{array}{c} \text{---} \Gamma^j \text{---} \\ | \\ \text{---} O \text{---} \\ | \\ \text{---} \Gamma^j \text{---} \end{array}. \quad (2.49)$$

As we shall see in section 2.2 however, there is another, more important reason for introducing these forms. Namely, they will be used to construct the projectors that will allow us to compute the time evolution for an MPS restricted to a fixed bond dimension manifold.

2.1.5 QR Decomposition

Instead of an SVD, one can often perform a computationally cheaper operation known as the QR decomposition. This takes an $m \times n$ matrix M , where $m \geq n$ and decomposes it as,

$$\text{---} m \text{---} \text{---} M \text{---} n \text{---} = \text{---} m \text{---} \text{---} Q \text{---} n \text{---} \text{---} R \text{---} n \text{---}. \quad (2.50)$$

The matrix R is upper triangular. The QR decomposition can be used in place of the SVD to form all of the gauges introduced in section 2.1.4, with the caveat that the inter-site matrices present in the mixed canonical and canonical gauges will now be upper

triangular R matrices rather than diagonal S matrices. This of course means that the Schmidt coefficients cannot not be read off from an MPS gauged in this way and thus one cannot calculate the entanglement using QRs alone. This indeed is the price one has to pay for the computational speed-up; however, we will see that in many situations it is only the orthogonality properties that we are interested in and for this a QR suffices.

The mirror image of the QR decomposition, defined for $n \geq m$ is known as the LQ decomposition:

$$-m- \textcircled{M} -n- = -m- \textcircled{L} -m- \textcircled{Q} -n-, \quad (2.51)$$

which is necessary for producing right normalised site tensors.

Just as with the SVD there exists a *thin* QR and a *full* QR. The above defines the thin QR and we will introduce the full version when the need arises.

2.2 Time Evolution

In the preceding sections we have introduced the MPS ansatz and shown that under certain conditions it can provide an efficient representation of a many-body wave function. Furthermore, we have shown that useful information, such as overlaps and expectation values of observables may be extracted efficiently from the MPS. So far however, we have not addressed the question of how one may actually construct an MPS for a wave function that one wishes to approximate.

In this thesis we will principally be interested in constructing MPS for wave functions that have been time evolved under some Hamiltonian \hat{H} from a simple initial condition: $|\psi(0)\rangle$; i.e., we want to find an MPS for $|\psi(t)\rangle$ where

$$|\psi(t)\rangle = e^{-iHt} |\psi(0)\rangle. \quad (2.52)$$

By simple initial condition we typically mean a product state of the form

$$|\psi(0)\rangle = |\phi_1\rangle \otimes |\phi_2\rangle \otimes \dots \otimes |\phi_N\rangle, \quad (2.53)$$

where $|\phi_j\rangle$ are states for the individual sub-systems. Constructing an MPS for a product state is trivial since the entropy of entanglement between each sub-system is zero and hence, by Eq. (2.37), we have $D = 1$.

Throughout this thesis we will make use of the following index ordering for the MPS site tensors:

$$A_{\alpha_l, \alpha_r, i} = \frac{\alpha_l}{\textcircled{A}} \frac{\alpha_r}{\textcircled{A}}; \quad (2.54)$$

that is, the first index corresponds to the left bond, the second to the right, and the third to the physical index. The product state $|\psi(0)\rangle$ may be written as an MPS consisting of site tensors:

$$A^j[1, 1, :] = |\phi_j\rangle. \quad (2.55)$$

The square brackets in Eq. (2.55) represent a programming inspired notation for specifying slices of multi-dimensional arrays. We use the convention that index values start from 1 and that a colon means that the index is expanded.

Far more difficult however, is the problem of finding an MPS for $|\psi(t)\rangle$; the Hamiltonian evolution will, in general, generate entanglement between MPS sites leading to a growing bond dimension which must be restricted in some way. The development of methods to tackle this problem has been the subject of intense research for a number of years. Broadly speaking, two approaches to time evolving an MPS have emerged [58].

In the first approach, one evaluates the right-hand side of Eq. (2.52) by breaking the unitary operator into a number of discrete time steps: $e^{-iHt} = e^{-iH\delta}e^{-iH\delta}\dots e^{-iH\delta}$, and finds a reduced expression for the operator $U(\delta) = e^{-iH\delta}$, usually in the form of an MPO, which may then be efficiently applied to the MPS $|\psi(t)\rangle$ in the manner of Eq. (2.13) to obtain $|\psi(t + \delta)\rangle$. In applying the MPO, the MPS bond dimension D will increase by a factor of the MPO bond dimension w , leading to an exponential growth with the number of time steps and thus necessitating a truncation after each step.

Most notably, the Time-Evolving-Block-Decimation (TEBD) algorithm [47], which was for a long time by far the most widely used MPS time evolution scheme, belongs to this class. In TEBD one splits the Hamiltonian into a sum of terms which each act on a set of neighbouring sites. These individual terms are ideally chosen to be small enough so that they may be exponentiated and applied with little computational effort. The unitary $U(\delta)$ is then constructed from these individually exponentiated terms in the manner of a Suzuki-Trotter splitting [59]. TEBD is most naturally suited to nearest-neighbour Hamiltonians although it can be extended in many cases to treat long-range interactions using so-called swap-gates [60, 61]. TEBD has some disadvantages: approximating $U(\delta)$ by splitting it into local terms incurs a rather large error, which may only be reduced, either at the cost of a more expensive update step (employing higher order splitting schemes) [62], or by using a smaller time step δ (necessitating more updates); due to the necessary bond dimension truncation the evolution will be neither unitary nor energy conserving; and finally, the construction of the integrator is rather Hamiltonian dependent, particularly when long-range couplings are involved, and so does not present a ‘black-box’ method which may be immediately applied to generic problems.

More recently, the MPO $W^{I,II}$ [63] has been proposed which uses a different approach to constructing an MPO approximation for $U(\delta)$, based on a second order Taylor expansion of the exponential. This method offers two levels of accuracy in approximating $U(\delta)$, namely W^I and W^{II} . Under the simpler W^I approach, the MPO can be constructed directly from the knowledge of the MPO representation of \hat{H} . This represents an important advantage over TEBD as it means that one need only know how to express \hat{H} as an MPO (a problem that we will discuss in Sec. 2.5) in order to apply the method. In particular, it means that long-range couplings can be treated naturally with no extra algorithmic complexity. However, W^I comes with serious limitations. Specifically, in the Taylor expansion of $U(\delta)$ one ignores all products which contain overlapping operators, i.e., operators which act on the same site. As a result, the W^I fails to reproduce even site-local evolution. The W^{II} variant aims to remedy this by including overlapping

products, albeit at the cost of a significantly more complicated MPO construction. As with TEBD, the Suzuki-Trotter spitting of the time evolution operator introduces a large time step error, and furthermore, even without the MPS bond dimension truncation, the MPO approximation of $U(\delta)$ will in general break unitarity.

In the second approach, instead of trying to approximate the unitary operator itself, one attempts to approximate its *action* on $|\psi(t)\rangle$ to produce $|\psi(t + \delta)\rangle$ directly. Central to this latter approach is the Krylov sub-space method for approximating matrix exponentials [64]. One may approximate the action of $U(\delta)$ on $|\psi\rangle$ by projecting the Hamiltonian \hat{H} onto a Krylov sub-space \mathcal{K}_n , defined as $\mathcal{K}_n = \text{span}\{|\psi\rangle, \hat{H}|\psi\rangle, \dots, \hat{H}^{n-1}|\psi\rangle\}$. Due to the structure of the Krylov sub-space, the matrix exponential $e^{-i\hat{H}\delta}$ converges quickly in the sub-space dimension n and thus one may choose $n \ll \text{dim}(\hat{H})$. The projectors onto the Krylov sub-space are constructed from the so-called Krylov vectors which are a set of orthonormal vectors $\{|v_1\rangle, |v_2\rangle, \dots, |v_n\rangle\}$ which span \mathcal{K}_n . The Krylov vectors can be constructed recursively, starting by setting $|v_1\rangle$ to $|\psi\rangle$ normalised to 1, and then calculating $|v_i\rangle$ by applying \hat{H} to $|v_{i-1}\rangle$, and orthonormalising with respect to the two previously calculated Krylov vectors. The Hamiltonian is tri-diagonal in the Krylov basis and so may be efficiently diagonalised and subsequently exponentiated. Indeed, projecting the Hamiltonian onto the Krylov sub-space is equivalent to performing the Lanczos algorithm.

The most direct application of the Krylov method to time evolving a quantum state is via exact diagonalisation (ED), where the Hamiltonian \hat{H} is a sparse matrix and the wave function $|\psi(t)\rangle$ and Krylov vectors $|v_i\rangle$ are represented by dense vectors [65, 66]. This approach may be translated into the world of TN in the so-called ‘global Krylov’ method by using an MPO to represent the Hamiltonian, and MPS to represent the wave function and Krylov vectors [58, 67, 68]. Doing so can improve the scalability and the efficiency of certain operations; however, the repeated applications of the MPO \hat{H} on the MPS Krylov vectors generates large bond dimensions which must be truncated. This truncation in turn degrades the quality of the Krylov vectors causing their orthogonality properties to be lost and necessitating each Krylov vector to be orthonormalised with respect to *all* previous Krylov vectors. In practice, the need to store the highly entangled Krylov vectors means that, like ED, this method will be limited by system size. The chief advantages of this method are: 1) once the Krylov vectors have been calculated for a given time step δ one may interpolate between $|\psi(t)\rangle$ and $|\psi(t + \delta)\rangle$ on a very fine time grid at almost no extra cost; and 2) once one has an MPO representation of \hat{H} the method can be applied more or less as a ‘black box’.

Finally, we come to the Time-Dependent-Variational-Principle (TDVP) [69, 70]. The TDVP also belongs to the second approach and makes use of the Krylov method, however, rather than attempting to exponentiate the entire many-body Hamiltonian, one is able to update the MPS site-by-site by evolving under a series of effective *local* Hamiltonians. These effective Hamiltonians act on individual MPS sites and so live in a reduced Hilbert space whose dimension depends only on the local MPS dimensions (physical and virtual) rather than the global system size. As a result, one avoids the need to deal with highly entangled global Krylov vectors. As with the global Krylov method, the only

input that TDVP requires is the initial MPS $|\psi(0)\rangle$ and an MPO representation of \hat{H} , and thus it qualifies as what we call a ‘black box’ method. In addition, TDVP offers a unique advantage over all other methods in that the evolution it generates is unitary and conserves the energy along with all other constants of motion. It has also been shown recently that TDVP has the potential for parallelisation [71], offering significant performance improvements. Moreover, TDVP is efficient and easy to implement which makes it the ideal choice for the present work. All results presented in this thesis were obtained using TDVP and variants thereof. In the next section we will present the TDVP method in more detail.

2.2.1 Time-Dependent-Variational-Principle

The Time-Dependent-Variational-Principle (TDVP) is an approach due to Dirac and Frenkel to approximating the solution of a high-dimensional tensor differential equation on a lower dimensional manifold. In its original form, one has a differential equation of the form $\dot{A} = F(t, A)$, where A and F are tensors in a high dimensional manifold and one wishes to find the time-dependent tensor $Y(t)$ which lives on some lower dimensional, smooth, manifold \mathcal{M} , and which best approximates the solution. Formally, one wishes to find $Y(t) \in \mathcal{M}$ such that $\|\dot{Y}(t) - \dot{A}(t)\|$, or equivalently $\|\dot{Y}(t) - F(A, t)\|$, is minimised.

When $\|\cdot\|$ represents the Euclidean norm, $Y(t)$ satisfies the differential equation $\dot{Y}(t) = P_{T_{Y(t)}, \mathcal{M}} \dot{A}(t)$, where $P_{T_{Y(t)}, \mathcal{M}}$ is the orthogonal projector onto the tangent space of \mathcal{M} at the point $Y(t)$.

More recently the TDVP has been applied to the case where the tensor $Y(t)$ is represented in the MPS format and the manifold \mathcal{M} is the space of *full-ranked* MPS with a certain set of bond dimensions [72, 69, 70]. By full-ranked we mean that all of the Schmidt coefficients at every bi-partition are non-vanishing; or, in other words, the bond dimensions of the MPS could not be reduced without introducing some truncation error. Without this condition the manifold \mathcal{M} would not satisfy the necessary condition of smoothness and the tangent space projector $P_{T_{Y(t)}, \mathcal{M}}$ would not always be well defined. Specifically, rank-deficient MPS would correspond to singular points on the manifold. In fact, if the MPS $Y(t)$ is not full-ranked, the tangent space projector will have a dependence on the *gauge* of $Y(t)$. One could still solve for $Y(t)$ under this condition, however the solution would depend on the choice of MPS gauge [73]. This point is illustrated in Fig. 2.1. We will return to this point later and assume for the moment that all MPS are full-ranked.

In the present case, the high-dimensional tensor differential equation that we want to solve is the time-dependent Schroedinger equation (TDSE)

$$\frac{d}{dt} |\psi(t)\rangle = -i\hat{H} |\psi(t)\rangle, \quad (2.56)$$

and the approximate solution, under the constraint that the bond dimension of $|\psi\rangle$ be constant, is given by

$$\frac{d}{dt} |\psi(t)\rangle = -i\hat{\mathcal{P}}_{T_{|\psi(t)\rangle}, \mathcal{M}} \hat{H} |\psi(t)\rangle. \quad (2.57)$$

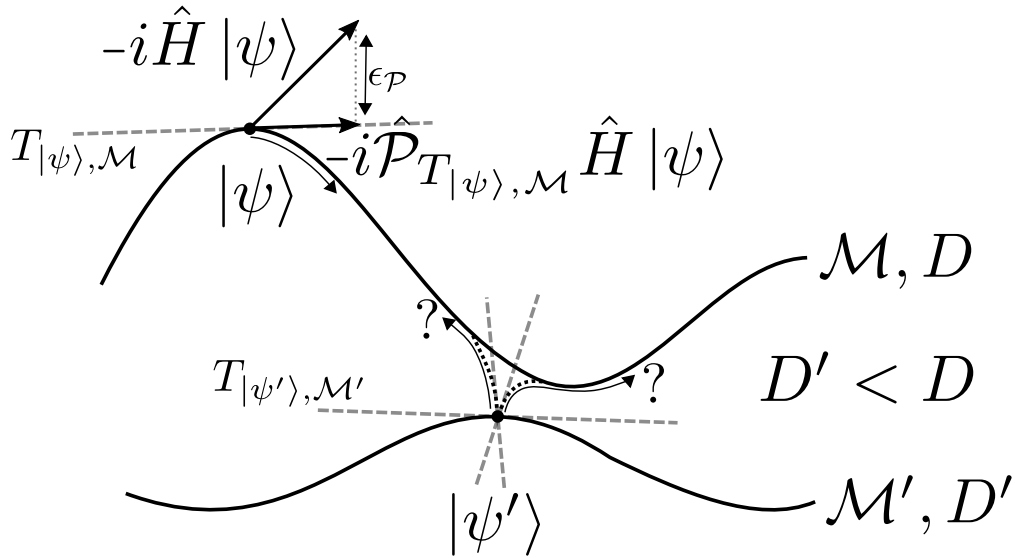


Figure 2.1: A cartoon illustrating the TDVP. The wave function $|\psi\rangle$, with bond dimension D , is a point on the full-ranked fixed bond dimension MPS manifold \mathcal{M} . Evolution under the Hamiltonian \hat{H} would in general take $|\psi\rangle$ out of this manifold and into one of a higher bond dimension. Applying the projector onto the tangent space $T_{|\psi\rangle, \mathcal{M}}$ constrains the evolution to \mathcal{M} . The wave function $|\psi'\rangle$ is a point on the manifold \mathcal{M}' with smaller bond dimension D' . One may extend the manifold \mathcal{M} to include rank-deficient MPS in order to incorporate the point $|\psi'\rangle$. However, $|\psi'\rangle$ would correspond to a singular point on this manifold where there is no unique tangent space. If one applied the TDVP to $|\psi'\rangle$ in the manifold \mathcal{M} , the evolution would be indeterminate. In practice however, this indeterminacy is resolved by the gauge of $|\psi'\rangle$.

Note that, throughout this thesis, we work in units for which $\hbar = 1$. Figure 2.1 gives a graphical representation of the dynamics generated by this equation. The action of the Hamiltonian on $|\psi\rangle$ produces a vector which would, in general, take $|\psi\rangle$ outside the manifold \mathcal{M} - causing the bond dimension to increase; applying the tangent space projector generates an effective Hamiltonian $\hat{\mathcal{P}}_{T_{|\psi(t)\rangle, \mathcal{M}}} \hat{H}$ under which the dynamics are constrained to \mathcal{M} . Applying the projector will of course introduce an error ϵ_P known as the *projection error*. Remarkably however, the projection error does not produce an error either in the norm of $|\psi\rangle$ nor in any of the quantities conserved by \hat{H} , such as the energy. The solution $|\psi(t)\rangle$ represents the wave function on \mathcal{M} nearest to the solution of the TDSE.

Equation (2.57) represents a complicated set of coupled differential equations. Indeed, on the face of it, the dependence of the tangent space projector on $|\psi(t)\rangle$ appears to increase the complexity with respect to the TDSE. Early attempts at solving these equations using an Euler integration scheme lacked numerical stability due to the need to calculate inverses of matrices containing small singular values. A key development was an analytic decomposition of the projector which dramatically simplified the resolution

of Eq. (2.57). The decomposition is the following:

$$\hat{\mathcal{P}}_{T_{|\psi\rangle}, \mathcal{M}} = \sum_{j=1}^N \hat{P}_{j-1}^{L, |\psi\rangle} \otimes \hat{\mathbf{1}}_j \otimes \hat{P}_{j+1}^{R, |\psi\rangle} - \sum_{j=1}^{N-1} \hat{P}_j^{L, |\psi\rangle} \otimes \hat{P}_{j+1}^{R, |\psi\rangle}, \quad (2.58)$$

where the projectors $\hat{P}_j^{L(R), |\psi\rangle}$ are defined in terms of the left (right) orthonormalised site tensors of $|\psi\rangle$:

$$\hat{P}_j^{L, |\psi\rangle} := \begin{array}{c} \dots \\ \dots \end{array} \begin{array}{c} i'_{j-2} \\ i'_{j-1} \\ i'_j \end{array} \begin{array}{c} \text{---} L \text{---} \\ \text{---} L \text{---} \\ \text{---} L \text{---} \end{array} \begin{array}{c} \dots \\ \dots \end{array}; \quad (2.59)$$

$$\hat{P}_j^{R, |\psi\rangle} := \begin{array}{c} i'_j \\ i'_{j+1} \\ i'_{j+2} \end{array} \begin{array}{c} \text{---} R \text{---} \\ \text{---} R \text{---} \\ \text{---} R \text{---} \end{array} \begin{array}{c} \dots \\ \dots \end{array} \begin{array}{c} i_j \\ i_{j+1} \\ i_{j+2} \end{array}. \quad (2.60)$$

As previously mentioned, an upward pointing physical leg on an MPS site implies that the elements are complex conjugated.

The proof of Eq. (2.58) is given in Ref. [69]. The form of the decomposition can be understood as follows: the tangent space of \mathcal{M} at $|\psi\rangle$ is constructed from basis vectors corresponding to all the one-site variations of $|\psi\rangle$; that is, changes to the MPS that affect one-site only. Applying the projector $\hat{\mathcal{P}}_{T_{|\psi\rangle}, \mathcal{M}}$ to some arbitrary MPS wave function $|\phi\rangle$, the first sum of terms in Eq. (2.58) has the effect of filtering out all contributions to $|\phi\rangle$ that differ from $|\psi\rangle$ at more than one site. If we were to only apply this first part of the projector to $|\phi\rangle$, the resulting MPS would be a linear sum of MPS that differ at only one site from $|\psi\rangle$, and would therefore lie in the tangent space; however, the normalisation of the state would be lost. Indeed, applying just the first part of the projector to $|\psi\rangle$ would yield $N|\psi\rangle$. The second sum is thus required to filter out all contributions that coincide with the state $|\psi\rangle$, such that $\hat{\mathcal{P}}_{T_{|\psi\rangle}, \mathcal{M}} |\psi\rangle = |\psi\rangle$.

We assume that the Hamiltonian \hat{H} can be expressed with the following MPO:

$$\hat{H} = \begin{array}{c} | \\ | \\ | \\ | \\ | \end{array} \begin{array}{c} \boxed{H^1} \\ \boxed{H^2} \\ \boxed{H^3} \\ \dots \\ \boxed{H^N} \end{array} \begin{array}{c} \text{---} \\ \text{---} \\ \text{---} \\ \text{---} \\ \text{---} \end{array} \begin{array}{c} | \\ | \\ | \\ | \\ | \end{array}. \quad (2.61)$$

Inserting the decomposition of the projector into Eq. (2.57), the right hand side will contain $2N - 1$ terms with the following tensor network structures

$$\hat{P}_{j-1}^{L,|\psi\rangle} \otimes \hat{\mathbf{1}}_j \otimes \hat{P}_{j+1}^{R,|\psi\rangle} \hat{H} |\psi\rangle = \left. \begin{array}{c} \dots \\ \dots \\ \dots \\ \dots \end{array} \right\} =: \hat{H}_{\text{eff}}^j ; \quad (2.62)$$

and

$$\hat{P}_j^{L,|\psi\rangle} \otimes \hat{P}_{j+1}^{R,|\psi\rangle} \hat{H} |\psi\rangle = \left. \begin{array}{c} \dots \\ \dots \\ \dots \\ \dots \end{array} \right\} =: \hat{K}_{\text{eff}}^j ; \quad (2.63)$$

where for each term we have gauged the MPS $|\psi\rangle$ so that its sites coincide with those that appear in the projector. We note that the matrices C^j will not typically correspond to the diagonal matrices S , as seen in Sec. 2.1.4, as the gauge transformations are usually performed using QR decompositions.

In Eq. (2.62) and (2.63) we have identified effective *local* Hamiltonians \hat{H}_{eff}^j and \hat{K}_{eff}^j which act on the MPS tensors A_C^j and C^j respectively. Each term on the right hand side of Eq. (2.57) consists simply of the original MPS with one tensor modified by the action of either \hat{H}_{eff}^j or \hat{K}_{eff}^j . Equation (2.57) can thus be decomposed into the following $2N - 1$ differential equations

$$\frac{d}{dt} A_C^j(t) = -i \hat{H}_{\text{eff}}^j A_C^j(t) \text{ for } j \in [1, N] \quad (2.64)$$

$$\frac{d}{dt} C^j(t) = +i \hat{K}_{\text{eff}}^j C^j(t) \text{ for } j \in [1, N - 1]. \quad (2.65)$$

Of course, although implicit in Eq. (2.64) and (2.65), the effective Hamiltonians \hat{H}_{eff}^j and \hat{K}_{eff}^j have a dependence on all tensors A_C^i and C^i for $i \neq j$; and thus, these $2N - 1$

differential equations are not uncoupled. However, if one assumes that all other tensors are constant in time, the Eq. (2.64) and (2.65) may be solved exactly:

$$A_C^j(t) = \exp(-i\hat{H}_{\text{eff}}^j t) A_C^j(0) \quad (2.66)$$

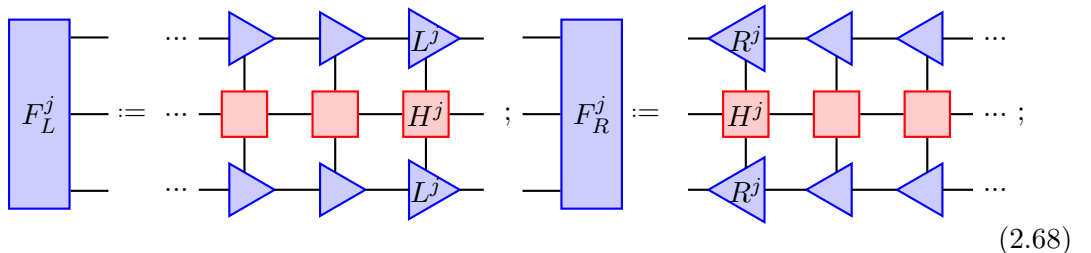
$$C^j(t) = \exp(+i\hat{K}_{\text{eff}}^j t) C^j(0). \quad (2.67)$$

The system of $2N - 1$ differential equations may thus be numerically integrated via a Lie-Trotter splitting whereby each tensor is evolved sequentially by a time step Δt , $A_C^j(t) \rightarrow A_C^j(t + \Delta t)$, $C^j(t) \rightarrow C^j(t + \Delta t)$, with the effective Hamiltonians updated after each local evolution. Each local evolution is performed using the Krylov sup-space method as explained in the preceding section.

The MPS format presents a natural order in which to update the tensors; namely, one starts with an MPS with the OC on, say, site 1; evolves $A_C^1(t) \rightarrow A_C^1(t + \Delta t)$; then, moves the OC to between sites 1 and 2, using QR or SVD; evolves $C^1(t) \rightarrow C^1(t + \Delta t)$; moves the OC to site 2, and so on until the end of the chain. The effective Hamiltonians are formed at each step using the tensors L^j from the previously time evolved sites. Performing one sweep in this way will produce the total MPS time-evolved by one time step Δt , i.e. $|\psi(t + \Delta t)\rangle$, with a time step error ϵ_T of order $\mathcal{O}(\Delta t^2)$.

This error may be improved if the local evolutions are performed with a time step $\Delta t/2$ and if the left-to-right sweep is composed with a subsequent right-to-left sweep; that is, after having performed the left-to-right sweep, and thus having evolved the MPS by $\Delta t/2$ and moved the OC to site N , one continues, evolving $A_C^N(t + \Delta t/2) \rightarrow A_C^N(t + \Delta t)$; moving the OC to between sites N and $N - 1$; evolving $C^{N-1}(t + \Delta t/2) \rightarrow C^{N-1}(t + \Delta t)$; moving the OC to site $N - 1$; and so on until the OC is back to its original position at site 1 and the MPS has been evolved by Δt . Of course, the two evolutions of the final MPS site may be combined into a single evolution $A_C^N(t) \rightarrow A_C^N(t + \Delta t)$. Naturally, when performing the right-to-left sweep, it is the tensors R^j that are updated in the effective Hamiltonians after each local evolution. This symmetric scheme corresponds to a second order integrator and thus the time step error is of order $\mathcal{O}(\Delta t^3)$. Furthermore, after two sweeps the MPS will be brought back to its initial gauge with the OC on site 1 and thus no further gauge transformations need to be performed before the next time step.

One may construct the effective Hamiltonians efficiently while sweeping the MPS by making use of previously computed tensor contractions; specifically, defining the set of *left and right environment tensors*:



$$F_L^j := \dots \begin{array}{c} \text{---} \triangleleft \text{---} \triangleleft \text{---} \triangleleft L^j \text{---} \\ \text{---} \square \text{---} \square \text{---} \square H^j \text{---} \\ \text{---} \triangleright \text{---} \triangleright \text{---} \triangleright L^j \text{---} \end{array} ; F_R^j := \begin{array}{c} \triangleright R^j \text{---} \triangleright \text{---} \triangleright \text{---} \\ \text{---} \square \text{---} \square \text{---} \square H^j \text{---} \\ \triangleright R^j \text{---} \triangleright \text{---} \triangleright \text{---} \end{array} ; \quad (2.68)$$

the effective Hamiltonians are given by:

$$\hat{H}_{\text{eff}}^j = F_L^{j-1} - H^j - F_R^{j+1}; \hat{K}_{\text{eff}}^j = F_L^j - F_R^{j+1}. \quad (2.69)$$

Now, when sweeping left to right, one has only to compute the next F_L tensor using the previously computed F_L and the L tensor from the last updated site; similarly, during the right-to-left sweep, it is the tensors F_R^j which are updated using the R tensors from the newly evolved A_C tensor:

$$F_L^j = F_L^{j-1} - L^j - H^j - L^j; F_R^j = R^j - H^j - R^j - F_R^{j+1}. \quad (2.70)$$

During the left-to-right sweep the tensors F_R do not have to be re-computed as they will already be available from the previous right-to-left sweep; of course, this also goes for the tensors F_L during the right-to-left sweep. An initialisation step is, however, necessary to compute the tensors F_R^j before the first left-to-right sweep.

We note finally that it is not necessary to store tensors F_L^j and F_R^j for all j simultaneously; instead we need only store N such tensors at any one time. For example, at the moment of evolving $C_{j'}$ during a left-to-right sweep, the tensors stored in memory are: F_R^j , for $j > j'$; and F_L^j , for $j \leq j'$.

2.2.2 Increasing the Bond Dimension

The TDVP is unique among MPS time evolution algorithms in that it does not naturally entail an increase in the bond dimensions. In practically all other approaches, the MPS update step causes the bond dimensions to grow, as a consequence of entanglement induced by sites interacting with one another. This growth, if unchecked, would lead to the size of the MPS becoming unmanageable, and thus it is necessary to compress the MPS by approximating it with one of a smaller bond dimension. This compression often carries with it the disadvantage that unitarity and energy conservation are lost. The TDVP is thus preferable in the sense that the bond dimension can be kept manageable without losing these key properties of quantum dynamics.

However, this poses a problem for our initial condition in Eq. (2.53). The bond dimension of this state is 1 since it is a product state; evolving the state under TDVP, the bond dimension would remain equal to 1, meaning no entanglement could ever arise

between the sites. Indeed, the problem is that when the bond dimension of the projector $\hat{P}_{T_{|\psi\rangle}, \mathcal{M}}$ is 1, all but the site-local evolution is projected out.

One solution to this problem is to use a two-site variant of TDVP, known as 2TDVP. Under 2TDVP one considers the tangent space $T_{|\psi\rangle, \mathcal{M}}^{[2]}$ for which the basis vectors are the *two-site* variations with respect to $|\psi\rangle$. By two-site variations we mean variations to the tensors $A^{[j,j+1]}$ that are obtained by contracting two neighbouring sites:

$$\text{---} \begin{array}{c} j \quad j+1 \\ \circ A \quad \circ A \\ \text{---} \end{array} \text{---} = \text{---} \begin{array}{c} \text{---} A^{[j,j+1]} \text{---} \\ | \quad | \end{array} \text{---} \quad (2.71)$$

These two-site variations live in a larger sub-space which includes MPS of higher bond dimension. The projector onto this tangent space is

$$\hat{P}_{T_{|\psi(t)\rangle, \mathcal{M}}^{[2]}} = \sum_{j=1}^{N-1} \hat{P}_{j-1}^{L, |\psi(t)\rangle} \otimes \hat{\mathbf{1}}_j \otimes \hat{\mathbf{1}}_{j+1} \otimes \hat{P}_{j+2}^{R, |\psi(t)\rangle} - \sum_{j=1}^{N-1} \hat{P}_{j-1}^{L, |\psi(t)\rangle} \otimes \hat{\mathbf{1}}_j \otimes \hat{P}_{j+1}^{R, |\psi(t)\rangle}. \quad (2.72)$$

The equations of motion resulting from inserting this projector into the TDSE may be solved by following exactly the same procedure as described above for the one-site version of TDVP, which we will henceforth refer to as 1TDVP. Where, under 1TDVP, we had the zero-site effective Hamiltonians \hat{K}_{eff}^j , we will now have the one-site effective Hamiltonians \hat{H}_{eff}^j ; and, where we had \hat{H}_{eff}^j , we will now have a *two-site* effective Hamiltonian $\hat{H}_{\text{eff}, [2]}^{j,j+1}$, given by

$$\hat{H}_{\text{eff}, [2]}^{j,j+1} := F_L^{j-1} - H^j - H^{j+1} - F_R^{j+2}. \quad (2.73)$$

After evolving the two-site tensor $A^{[j,j+1]}(t)$ by applying $\exp(-i\hat{H}_{\text{eff}, [2]}^{j,j+1}\Delta t/2)$, the resulting tensor $A^{[j,j+1]}(t + \Delta t/2)$ can be split back into two individual site tensors by applying an SVD:

$$\text{---} \begin{array}{c} -D_l - A^{[j,j+1]} -D_r - \\ | \quad | \\ d \quad d \end{array} \text{---} \xrightarrow{\text{reshape}} \text{---} \begin{array}{c} -dD_l - A^{[j,j+1]} -dD_r - \end{array} \text{---} \xrightarrow{\text{SVD}} \text{---} \begin{array}{c} j \quad j+1 \\ \triangle R \quad \diamond S^j \quad \triangle L \\ -r \quad -r \end{array} \text{---} \quad (2.74)$$

where $r = \min(dD_l, dD_r)$. The bond dimension between sites j and $j+1$ can then be truncated to any value $\leq r$ by throwing away any singular values in S^j that fall below some threshold. In this way, the MPS bond dimension will grow dynamically throughout the course of the evolution to capture entanglement, as and when it emerges.

This solution, however, is not ideal; notably because, as discussed above, the truncation will entail a loss of unitarity, which was one of the main attractions of the TDVP method. Indeed, for a nearest-neighbour Hamiltonian, applying the two-site projector will not entail a projection error, leading to a scheme that is almost identical to TEBD, wherein the error arises solely from the truncation. While an error arising from truncation is not inherently worse than a projection error [74], certain observables can be obtained more accurately with 1TDVP; notably, the 1TDVP projector has been shown to give a smaller error in global observables connected to the energy [74], and also in the long-time dynamics of thermalising systems [75].

Furthermore, 2TDVP scales poorly with the local physical dimension. The dominant cost of 2TDVP is the computation of the tensor network contraction $\hat{H}_{\text{eff},[2]}^{j,j+1} A^{[j,j+1]}$ which has a complexity of $\mathcal{O}(D^2 d^3 w^2 + D^3 d^2 w + D^3 d^3)$ [71]. This scales a factor of d worse than the cost of computing $\hat{H}_{\text{eff}}^j A_C^j$, the dominant operation in 1TDVP, which has a complexity of $\mathcal{O}(D^2 d^2 w^2 + D^3 d w + D^3 d^2)$ [76]. While this poor scaling with d would not be an issue for many problems in condensed matter where d is fixed by the nature of the model, such as a spin- $\frac{1}{2}$ chain where one always has $d = 2$, in the open quantum system problem, as we will see in Sec. 2.4, d corresponds to the size of the truncated Fock basis of the bosonic modes and thus becomes a convergence parameter. As a result, the scaling with respect to d is crucial. In practice, we find 2TDVP to be highly disadvantageous for this reason.

Moreover, we make the observation that there is an inherent inefficiency in computing a large object, namely $A^{[j,j+1]}$, only to partially discard it later on.

An alternative approach is instead to stick with 1TDVP but to *embed* the product state $|\psi(0)\rangle$ in a MPS of a larger bond dimension. This could be achieved, for example, by padding the site tensors with zeros. Thus we could write the state $|\psi(0)\rangle$ with an MPS consisting of sites

$$A^j[\alpha_{jl}, \alpha_{jr}, :] = \delta_{\alpha_{jl}, 1} \delta_{\alpha_{jr}, 1} |\phi_j\rangle, \quad (2.75)$$

where the indices $\alpha_{jr(l)}$ may run up to any positive integer value subject only to the constraints imposed on the bond dimensions by the MPS format (cf. Sec. 2.1.4). Applying the 1TDVP to this MPS, the site tensors will ‘fill out’ and quickly become full-ranked.

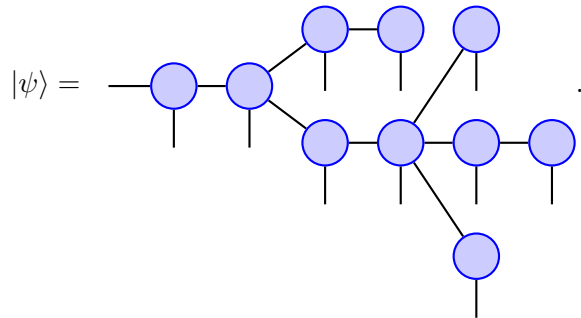
Embedding the MPS in this way achieves the same goal as using the two-site projector; namely, expanding the tangent space. The key difference is that now we must *choose* the new bond dimension in advance of the evolution. On the one hand this is an advantage, as it means that we are not forced to ‘overshoot’ to a bond dimension that is too large, and then truncate to a more manageable one. On the other hand however, there is no *a priori* way to know in advance of the evolution what bond dimensions will give the right balance between speed and accuracy. Typically, one performs the embedding once, on the initial wave function, for some bond dimension; performs the complete time evolution up to the desired time step; and then repeats for a larger bond dimension, and so on, until the observables of interest converge. The main disadvantage of such an approach is that the bond dimensions do not follow the growth of entanglement in the state, and will thus inevitably be non-optimal. Another point to make is the one illustrated by Fig. 2.1, namely that the evolution of a rank-deficient MPS, such as that

of Eq. (2.75), is *gauge dependent*. In other words, the manner in which the MPS is embedded is not arbitrary, but can, in principle, affect the evolution, and thus the quality of the final MPS. A natural question to ask is therefore: *how can this be optimised?*

In chapter 5 we will develop an approach to attempt to address these issues.

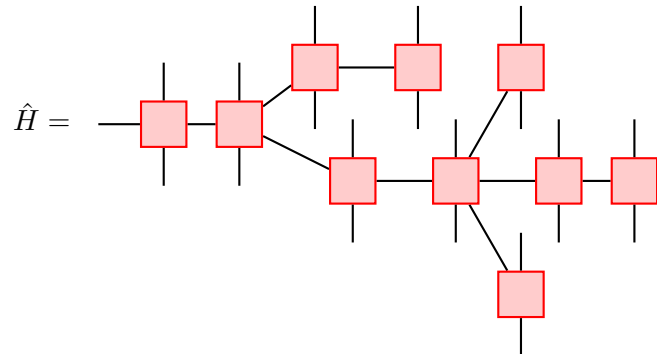
2.3 Tree-MPS

An extension to the MPS format, which we will make much use of in this thesis, is the *tree-MPS*. A tree-MPS is a generalisation of the MPS wherein each site, instead of being connected to only one other site to its right, may be connected to any arbitrary number of *child* sites; for example:



The diagram shows a tree-MPS state $|\psi\rangle$ represented by blue circles (sites) and lines (legs). The leftmost site is connected to a single leg extending to the left. The second site is connected to the first site and has two child sites. The third site is connected to the second site and has two child sites. The fourth site is connected to the third site and has two child sites. The fifth site is connected to the fourth site and has two child sites. The sixth site is connected to the fifth site and has two child sites. The seventh site is connected to the sixth site and has two child sites. The eighth site is connected to the seventh site and has two child sites. The ninth site is connected to the eighth site and has two child sites. The tenth site is connected to the ninth site and has two child sites. The eleventh site is connected to the tenth site and has two child sites. The twelfth site is connected to the eleventh site and has two child sites. The thirteenth site is connected to the twelfth site and has two child sites. The fourteenth site is connected to the thirteenth site and has two child sites. The fifteenth site is connected to the fourteenth site and has two child sites. The sixteenth site is connected to the fifteenth site and has two child sites. The seventeenth site is connected to the sixteenth site and has two child sites. The eighteenth site is connected to the seventeenth site and has two child sites. The nineteenth site is connected to the eighteenth site and has two child sites. The twentieth site is connected to the nineteenth site and has two child sites. The diagram is labeled (2.76).

Naturally, one can also have a tree-MPO:



The diagram shows a tree-MPO state \hat{H} represented by red squares (sites) and lines (legs). The leftmost site is connected to a single leg extending to the left. The second site is connected to the first site and has two child sites. The third site is connected to the second site and has two child sites. The fourth site is connected to the third site and has two child sites. The fifth site is connected to the fourth site and has two child sites. The sixth site is connected to the fifth site and has two child sites. The seventh site is connected to the sixth site and has two child sites. The eighth site is connected to the seventh site and has two child sites. The ninth site is connected to the eighth site and has two child sites. The tenth site is connected to the ninth site and has two child sites. The eleventh site is connected to the tenth site and has two child sites. The twelfth site is connected to the eleventh site and has two child sites. The thirteenth site is connected to the twelfth site and has two child sites. The fourteenth site is connected to the thirteenth site and has two child sites. The fifteenth site is connected to the fourteenth site and has two child sites. The sixteenth site is connected to the fifteenth site and has two child sites. The seventeenth site is connected to the sixteenth site and has two child sites. The eighteenth site is connected to the seventeenth site and has two child sites. The nineteenth site is connected to the eighteenth site and has two child sites. The twentieth site is connected to the nineteenth site and has two child sites. The diagram is labeled (2.77).

Provided the tree does not contain any *loops*, everything that one can do to an MPS/MPO can be extended straight-forwardly to tree-MPS/MPOs. Indeed, the generalisation to trees introduces no new conceptual complexity (only implementational complexity), and so we will not spend any time in generalising the concepts, already introduced, to trees. We will however set out the notational conventions that will be used when talking about tree-MPS/MPO, as these will be useful to us later on.

The sites of a tree-MPS are usually referred to as *nodes*. For our purposes, every node of a tree-MPS/MPO has one *parent* leg pointing to the left, and any number (including zero) of *child* legs pointing to the right. The leftmost node is known as the *head-node*. The parent leg of the head-node connects to no other site and corresponds to a dummy index with dimension 1.

The indices of the site tensors have the following ordering:

$$A_{\alpha,\beta_1,\beta_2,\beta_3,\dots,i} = \alpha \text{ --- } \textcircled{A} \begin{array}{l} \nearrow \beta_1 \\ \rightarrow \beta_2 \\ \searrow \beta_3 \\ \downarrow i \\ \vdots \end{array} ; H_{\alpha,\beta_1,\beta_2,\beta_3,\dots,i,i'} = \alpha \text{ --- } \textcircled{H} \begin{array}{l} \downarrow i' \\ \nearrow \beta_1 \\ \rightarrow \beta_2 \\ \searrow \beta_3 \\ \downarrow i \\ \vdots \end{array} ; \quad (2.78)$$

that is, the first index corresponds to the parent bond; the second to $(n_c + 1)$ th indices correspond to the bonds to the n_c children; and the physical index, or indices for an MPO site, come last. The ordering of the child indices is determined by their graphical representation and is chosen to be from top to bottom. We also apply this index ordering convention to ordinary MPS, which are of course just a special case of tree-MPS.

We note that this convention has a small consequence for the performance of TDVP on an ordinary MPS, which is that the LQ decompositions performed during a right-to-left TDVP sweep will not require any tensor permutations, and will therefore be slightly faster than the corresponding QR decompositions, performed on the left-to-right sweep.

2.4 Tensor Networks for Open Quantum Systems

In this section we make the link between the tensor network methods discussed in Sec. 2.1 and 2.2, and open quantum systems (OQS).

An OQS Hamiltonian takes the following form

$$\hat{H} = \hat{H}_S + \hat{H}_I + \hat{H}_B, \quad (2.79)$$

where \hat{H}_S is a Hamiltonian for the ‘system’, \hat{H}_B is a Hamiltonian for the ‘bath’ and \hat{H}_I is an interaction Hamiltonian describing the coupling between the system and bath. In this section we will consider an OQS with linear coupling to \mathcal{N}_B independent baths each consisting of a continuum of bosonic modes. The general forms of the interaction and bath Hamiltonians are the following

$$\hat{H}_I = \sum_{\alpha=1}^{\mathcal{N}_B} \hat{H}_{I_\alpha}, \quad \hat{H}_B = \sum_{\alpha=1}^{\mathcal{N}_B} \hat{H}_{B_\alpha}, \quad (2.80)$$

with

$$\hat{H}_{I_\alpha} = \hat{A}_\alpha \otimes \int_0^\infty d\omega \sqrt{J_\alpha(\omega)} (b_{\alpha,\omega}^\dagger + b_{\alpha,\omega}), \quad (2.81)$$

$$\hat{H}_{B_\alpha} = \int_0^\infty d\omega \omega b_{\alpha,\omega}^\dagger b_{\alpha,\omega}, \quad (2.82)$$

where $b_{\alpha,\omega}^\dagger$ and $b_{\alpha,\omega}$ are, respectively, the creation and annihilation operators for the bath α , and \hat{A}_α is an operator in the Hilbert space of the system. The functions $J_\alpha(\omega)$ characterise the coupling to the different baths and are known as *spectral densities* (SD).

Formally, the Hilbert space dimension of the above Hamiltonian is infinite; thus, in order to facilitate a numerical treatment, it is necessary to discretise the baths and to apply a cut-off frequency, such that they may be treated as a *finite* collection of \mathcal{N}_m modes k with a *discrete* set of frequencies ω_k :

$$\hat{H}_{I_\alpha} = \hat{A}_\alpha \otimes \sum_{k=1}^{\mathcal{N}_m} g_{\alpha,k} (b_{\alpha,k}^\dagger + b_{\alpha,k}), \quad (2.83)$$

$$\hat{H}_{B_\alpha} = \sum_{k=1}^{\mathcal{N}_m} \omega_{\alpha,k} b_{\alpha,k}^\dagger b_{\alpha,k}, \quad (2.84)$$

where the coefficients $g_{\alpha,k}$ are related to the spectral densities by

$$J_\alpha(\omega) \equiv \sum_k |g_{\alpha,k}|^2 \delta(\omega - \omega_{\alpha,k}). \quad (2.85)$$

In fact, it is often not an approximation to treat the baths in this way; in real-world problems, the bath is frequently not in the thermodynamic limit but really *is* a finite set of modes. Therefore, it is normally more accurate to consider the continuous formulation, in terms of the spectral densities $J_\alpha(\omega)$, as a mathematical *convenience* rather than as the exact model to which we apply approximations. In either case, the number of modes required to give an accurate description of a bath will be large, typically $\mathcal{N}_m \sim 100 - 1000$; thus, truncating the local Hilbert spaces of the harmonic oscillators to include just the first d Fock states, the total Hilbert space dimension of each bath will be of order $\mathcal{O}(d^{100-1000})$, making a numerically exact treatment out of the question.

In principle, one could imagine trying to remedy this problem by applying the MPS ansatz directly to the problem as formulated above. The Hilbert space has a natural product state structure allowing a tensorial representation of the form of Eq. (2.8). Considering, for simplicity, the case where there is just one bath interacting with the system; the first physical leg could correspond to the system, and the other $N - 1$ legs could correspond to the bath modes (the ordering is not important). However, it is easy to see that such a state evolving under the above Hamiltonian would satisfy the *volume law* of entanglement (cf. Sec. 2.1.4). This is because \hat{H}_I couples the system to *all* \mathcal{N}_m bath modes and thus we can expect the system to become simultaneously entangled with every mode. Making a cut at some point along the chain, the entanglement between the two halves will depend on the number of modes separated from the system, i.e. the *volume* of the regions. The MPS ansatz would therefore be worse than useless.

However, by applying a unitary transformation, it is possible to map the OQS Hamiltonian into one with precisely the kind of interactions terms favoured by the MPS representation; namely, local couplings between neighbouring sites. This mapping is known as the chain mapping.

2.4.1 Chain mapping

The chain mapping [77] is a unitary transformation $U_{\alpha,n}(\omega)$ which allows us to define new modes

$$c_{\alpha,n}^{(\dagger)} = \int_0^\infty d\omega U_{\alpha,n}(\omega) b_{\alpha,\omega}^{(\dagger)}, \quad (2.86)$$

for each bath α . The new modes, rather than coupling to the system in a *star-like* fashion, as in Eq. (2.81), where the system couples to *every* mode (See Fig. 2.2(a)), form semi-infinite nearest-neighbour chains where only the first site is coupled to the system (See Fig. 2.2(b)). Under this transformation, the interaction and bath Hamiltonians become

$$\hat{H}_{I_\alpha}^{\text{chain}} = U_\alpha \hat{H}_{I_\alpha}^{\text{star}} U_\alpha^\dagger = \kappa_\alpha \hat{A}_\alpha \otimes (c_{\alpha,0} + c_{\alpha,0}^\dagger), \quad (2.87)$$

and

$$\hat{H}_{B_\alpha}^{\text{chain}} = U_\alpha \hat{H}_{B_\alpha}^{\text{star}} U_\alpha^\dagger = \sum_{n=0}^{\infty} \epsilon_{\alpha,n} c_{\alpha,n}^\dagger c_{\alpha,n} + \sum_{n=0}^{\infty} t_{\alpha,n} (c_{\alpha,n} c_{\alpha,n+1}^\dagger + c_{\alpha,n}^\dagger c_{\alpha,n+1}), \quad (2.88)$$

where we have used the label ‘star’ to refer to the Hamiltonians as defined by Eq. (2.81) and (2.82).

Each bath is mapped separately onto a chain, coupled at one end to the system. If $\mathcal{N}_B = 1$ or 2, the total Hamiltonian $\hat{H}^{\text{chain}} = \hat{H}_S + \sum_{\alpha=1}^{\mathcal{N}_B} \hat{H}_{I_\alpha}^{\text{chain}} + \sum_{\alpha=1}^{\mathcal{N}_B} \hat{H}_{B_\alpha}^{\text{chain}}$ will have a 1D, or chain, topology, leading to a natural representation in the MPS format; however, when $\mathcal{N}_B > 2$, H^{chain} will have a *tree* topology, and so a tree-MPS will be more suitable.

This transformation, which is essentially a ‘tri-diagonalisation’ of the bath Hamiltonians, can be constructed with the help of the theory of *orthogonal polynomials*. The transformation is given by

$$U_{\alpha,n}(\omega) = \sqrt{J_\alpha(\omega)} \tilde{p}_{\alpha,n}(\omega), \quad (2.89)$$

where $\{\tilde{p}_{\alpha,n}(\omega), n = 0, 1, 2, \dots\}$ is the set of polynomials that are orthonormal with respect to the measure $d\omega J_\alpha(\omega)$, i.e., which satisfy

$$\int_0^\infty d\omega J_\alpha(\omega) \tilde{p}_{\alpha,n} \tilde{p}_{\alpha,m} = \delta_{n,m}. \quad (2.90)$$

The forms of the chain Hamiltonians, along with the chain coefficients, $\kappa_\alpha, \epsilon_{\alpha,n}, t_{\alpha,n}$, are derived in Appendix 2.A. The interaction terms in this chain Hamiltonian will only generate entanglement locally, between neighbouring sites, and so we can expect an MPS to be a good ansatz for a wave function evolving under this Hamiltonian.

The semi-infinite chains must then be truncated after some suitable site $n = \mathcal{N}_m - 1$, such they contain the finite number of modes \mathcal{N}_m . We use the same symbol \mathcal{N}_m to represent the number of modes in the chain basis as we used in Eq. (2.83) and (2.84) for the number for modes in the sampling of the continuous spectral densities. This choice of notation is in accordance with the fact that *truncation* in the chain mode basis is equivalent to *sampling* in the original star basis. Indeed, we could have decided to

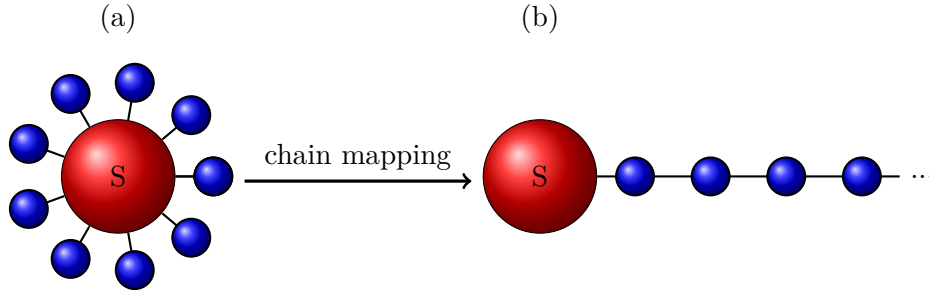


Figure 2.2: Pictorial representation of the chain mapping; the Hamiltonian is mapped from one in which the system couples directly to every mode (a), into one in which the system couples to just one mode, while the modes form a nearest-neighbour chain (b).

perform these two operations in reverse order, i.e., first discretise the spectral densities with \mathcal{N}_m modes and then perform the chain mapping, which, in that case, would just correspond to a tri-diagonalisation of a $\mathcal{N}_m \times \mathcal{N}_m$ matrix and could be carried out via the Lanczos method.

We will see however that the dynamics in the chain mode basis obey a ‘light-cone’ structure, whereby a wave-front travels out along the chain from the system (See Fig. 2.3); any perturbations to the initial state outside of this wave-front are exponentially suppressed [78]. It is natural, therefore, to perform the truncation in the chain basis, since truncating the chain at any point beyond the wave-front will introduce a vanishing error. One can even save time and memory by using a dynamic truncation whereby the chain grows through the simulation to track the expanding wave-front.

2.4.2 Finite temperatures

The chain mapping was first combined with tensor network time evolution methods of the kind discussed in Sec. 2.2 by Prior et al. [79] to form a powerful method for simulating OQS in the non-perturbative, and non-Markovian regimes, which later became known as the Time Evolving Density Operator with Orthogonal Polynomials Algorithm (TEDOPA). However, the method as it currently stands has a major limitation. The initial condition that we would like to simulate is the following:

$$\rho(0) = |\phi_S\rangle \langle \phi_S| \otimes \prod_{\alpha} \rho_{\alpha}(\beta_{\alpha}), \quad (2.91)$$

where ($k_B = 1$)

$$\rho_{\alpha}(\beta_{\alpha}) = \frac{1}{Z_{\alpha}} \exp\left(-\beta_{\alpha} \hat{H}_{B_{\alpha}}\right), \quad (2.92)$$

and where Z_{α} is the partition function of the bath α defined as

$$Z_{\alpha} = \text{Tr} \left\{ e^{-\beta_{\alpha} \hat{H}_{B_{\alpha}}} \right\}. \quad (2.93)$$

Our initial condition is a density matrix, consisting of the product of a pure system state and thermal density matrices for the baths. An MPS on the other hand is an

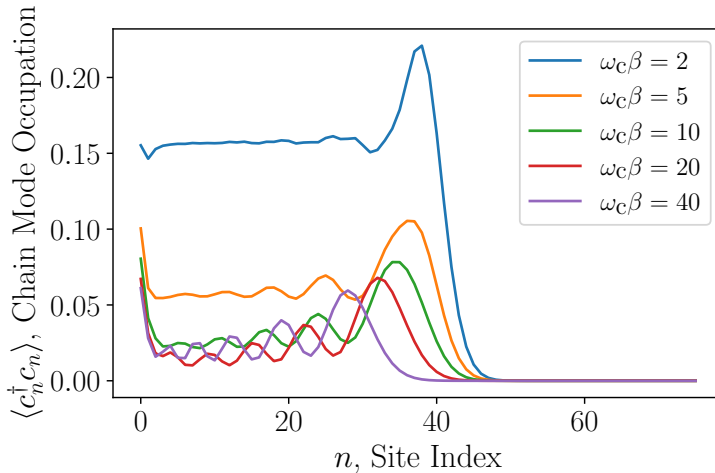


Figure 2.3: Chain mode occupations $\langle c_n^\dagger c_n \rangle$ at different inverse temperatures for a snapshot at $\omega_c t = 45$. The bath is an Ohmic one with a hard cut-off ω_c and $\alpha = 0.1$. The system Hamiltonian is that of the Spin-Boson-Model (SBM), i.e. $\hat{H}_S = \frac{\omega_0}{2} \sigma_z$ and $\hat{A}_S = \sigma_x$. The TLS gap is $\omega_0 = 0.2\omega_c$.

ansatz for a *wave function*, not a density matrix, and so cannot be directly applied to $\rho(0)$. One approach is to extend the notion of MPS to mixed states by representing the density matrix as an MPO, known as a Matrix-Product Density-Operator (MPDO) [80, 81] or equivalently considering the density matrix as a *vector* in Liouville space. In the latter case, the density matrix looks like a wave function and so could be expressed as an MPS. However, the physical dimensions for such an MPS would be d^2 , leading to an overall complexity of $\mathcal{O}(d^4)$ for TDVP, which is undesirable. Furthermore, the construction of the finite temperature MPDO is based on ‘cooling down’ an infinite temperature state to a finite temperature one via an imaginary time evolution; thus, while practical for high temperatures, the algorithm becomes exceedingly expensive for low or intermediate temperatures, although a variant for low temperatures has been proposed [82].

On the other hand, one could consider a sampling approach, as in the Minimally Entangled Typical Thermal State Algorithm [83, 84, 85] or the Multi-Layered Multi-Configurational Time-Dependent Hartree (ML-MCTDH) method [31], where one performs many, pure state simulations with different initial states. However, the cost of an individual MPS simulation, in addition to the rapid growth of the number of possible thermal configurations with temperature, makes such an approach intractably expensive. Only in the case where $\beta = \infty$, i.e., $T = 0$, will direct simulation via MPS be feasible, since in this limit only the ground states of the baths will be occupied: the initial density matrices reduce to pure states

$$\rho_\alpha(\beta \rightarrow \infty) = |0\rangle_\alpha \langle 0|, \quad (2.94)$$

where $|0\rangle_\alpha$ represents the vacuum state of the bath α .

Luckily however, due to a result of Tamascelli et al. [86, 87], one can take advantage of some special properties of the initial condition of Eq. (2.91) to perform a transformation which will render the general finite temperature problem no more complex than the zero temperature case. By special properties we refer to the fact that $\rho(0)$ is a product of system + bath states, and that the thermal initial condition of the bath oscillators is a Gaussian state. Under these conditions, it is known that the reduced system dynamics, i.e., the time evolved reduced density matrix for the system, obtained from tracing out the bath degrees of freedom:

$$\rho_S(t) = \text{Tr}_B \{ \rho(t) \}, \quad (2.95)$$

is fully determined by the equilibrium two-time correlation functions

$$S_\alpha(t) = \int_0^\infty d\omega J_\alpha(\omega) \left\langle \left(b_{\alpha,\omega}^\dagger(t) + b_{\alpha,\omega}(t) \right) \left(b_{\alpha,\omega}^\dagger(0) + b_{\alpha,\omega}(0) \right) \right\rangle, \quad (2.96)$$

where the angled brackets denote the thermal expectation: $\langle \cdot \rangle := \text{Tr} \{ \cdot \rho_B \}$. Crucially, this means that any two baths with the same $S_\alpha(t)$ will give rise to the same reduced system dynamics. This theorem has long been a well-known result in OQS theory. In particular, it is a key result within the Feynman-Vernon influence functional formulation where it is known that for a Gaussian bath, the influence functional can be analytically derived in terms of $S_\alpha(t)$. However, the notion of *equivalence*, that is, the idea that one may substitute one bath for another without affecting $\rho_S(t)$, has only recently been exploited in the present context by Tamascelli et al..

The time evolution in Eq. (2.96) is performed in the interaction picture, according to which the bath operators, $b_{\alpha,\omega}^\dagger$ and $b_{\alpha,\omega}$, evolve under the their respective bath Hamiltonians \hat{H}_{B_α} . Since \hat{H}_{B_α} is diagonal with respect to these operators, their evolution is given simply by

$$b_{\alpha,\omega}(t) = e^{-i\omega t} b_{\alpha,\omega} \quad (2.97)$$

$$b_{\alpha,\omega}^\dagger(t) = e^{+i\omega t} b_{\alpha,\omega}^\dagger \quad (2.98)$$

Substituting these expressions into Eq. (2.96) we have

$$S_\alpha(t) = \int_0^\infty d\omega J_\alpha(\omega) (e^{i\omega t} n_{\beta_\alpha}(\omega) + e^{-i\omega t} (n_{\beta_\alpha}(\omega) + 1)), \quad (2.99)$$

where we have introduced the Boltzmann factors $\langle b_{\alpha,\omega}^\dagger b_{\alpha,\omega} \rangle = n_{\beta_\alpha}(\omega)$. The two-time correlation function for each bath is thus a function only of its temperature and its spectral density.

Since the problem reduces dramatically when $\beta = \infty$, our goal is to find different baths, characterised by different spectral densities, which reproduce exactly the same functions $S_\alpha(t)$ for $\beta = \infty$; that is, we want to find $J_\alpha(\omega, \beta)$ such that

$$S_\alpha(t) = \int_{-\infty}^\infty d\omega J_\alpha(\omega, \beta) e^{-i\omega t}. \quad (2.100)$$

The domain of the above integral has been extended to cover *negative* frequencies, which is necessary in order to include the counter-rotating terms present in the integral

of Eq. (2.99). The effective spectral densities $J_\alpha(\omega, \beta)$ can then be formed by absorbing the temperature-dependent Boltzmann factors into the spectral densities $J_\alpha(\omega)$. Using the relation

$$\frac{1}{2}(1 + \coth(\omega\beta/2)) \equiv \begin{cases} -n_\beta(|\omega|), & \omega < 0 \\ n_\beta(\omega) + 1, & \omega \geq 0 \end{cases}, \quad (2.101)$$

the effective spectral densities are found to be

$$J_\alpha(\omega, \beta) = \text{sign}(\omega) \frac{J_\alpha(|\omega|)}{2} \left(1 + \coth\left(\frac{\omega\beta_\alpha}{2}\right) \right), \quad (2.102)$$

where $\text{sign}(\omega) = 1$ when $\omega \geq 0$ and -1 when $\omega < 0$. Thus, we find that our open system problem is completely equivalent to one in which the system couples to extended baths, governed by the Hamiltonian

$$H = \hat{H}_S + \sum_\alpha \hat{H}_{I_\alpha}^{\text{ext}} + \sum_\alpha \hat{H}_{B_\alpha}^{\text{ext}}, \quad (2.103)$$

where

$$\hat{H}_{B_\alpha}^{\text{ext}} = \hat{A}_\alpha \otimes \int_{-\infty}^{\infty} d\omega \sqrt{J_\alpha(\omega, \beta)} (b_{\alpha, \omega}^\dagger + b_{\alpha, \omega}), \quad (2.104)$$

$$\hat{H}_{I_\alpha}^{\text{ext}} = \int_{-\infty}^{\infty} d\omega \omega b_{\alpha, \omega}^\dagger b_{\alpha, \omega}, \quad (2.105)$$

and which has the pure state initial condition

$$\rho(0) = |\psi(0)\rangle \langle \psi(0)| = |\phi_S\rangle \langle \phi_S| \otimes \prod_\alpha |0\rangle_\alpha \langle 0|. \quad (2.106)$$

These *extended* baths are able to mimic the effects of temperature by encoding the thermal detailed balance between absorption and emission processes in the ratio of the coupling strengths to positive and negative modes, as opposed to in the statistics of the initial state:

$$\frac{J_\alpha(\omega, \beta_\alpha)}{J_\alpha(-\omega, \beta_\alpha)} = e^{\beta_\alpha \omega}. \quad (2.107)$$

Indeed, from the systems point of view, there is no difference between the absorption from an occupied, positive energy, bath mode and the emission into an unoccupied, negative energy, bath mode.

In fact, the equivalence between these two environments goes beyond the reduced system dynamics as there exists a unitary transformation which links the extended environment to the original thermal environment. This means that one is able to reverse the transformation and calculate thermal expectations for the actual bosonic bath such as $\langle b_{\alpha, \omega}^\dagger b_{\alpha, \omega} \rangle_\beta$. This represents an important advantage over master equation or influence functional based methods for OQS which focus on tracing out the bath degrees of freedom *before* the dynamics are resolved: meaning only information pertaining to the system, i.e. $\rho_S(t)$, is available.

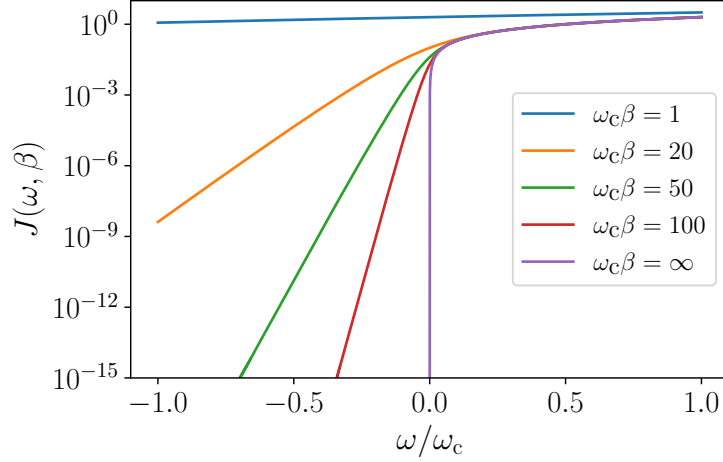


Figure 2.4: The temperature mapped, Ohmic spectral density with a hard cut off ω_c .

In Fig. 2.4 we plot $J(\omega, \beta)$ for a range of inverse temperatures when $J(\omega)$ is an Ohmic spectral density with a hard cut-off at ω_c :

$$J(\omega) = 2\alpha\omega\theta(\omega - \omega_c). \quad (2.108)$$

The function $\theta(\omega - \omega_c)$ denotes the Heaviside step function.

We find that increasing the temperature has the effect of extending the thermal SD into the negative frequency region. In the high temperature limit ($\beta \rightarrow 0$), when emission and absorption processes become equally rapid, the thermal SD tends to become symmetric about the zero frequency line. For intermediate temperatures, the thermal SD is exponentially suppressed in the negative frequency region allowing a natural minimum cut-off frequency ω_{\min} to be identified.

Following this transformation, the baths can be mapped onto chains by applying the mapping described in Sec. 2.4.1 with the *thermal* spectral densities $J_\alpha(\omega, \beta)$ as input. As the initial states for the extended baths are simply vacuum states, they are unaffected by the chain mapping; or rather, they become the vacuum states of the modes of the *chain-mapped*, extended baths. Thus, the many-body initial state may be efficiently propagated using MPS methods and the reduced system density matrix ρ_S extracted by tracing out the bath degrees of freedom after the simulation. Bath observables may also be measured, although it will be necessary to reverse both transformations in order to return to the original mode basis.

In Fig. 2.5 we show the chain parameters generated from the temperature mapped Ohmic spectral density at several temperatures. If the spectral density belongs to the Szegő class (See Ref.[77] Definition II.5) as is the case for $J(\omega, \beta)$ with $J(\omega)$ given by

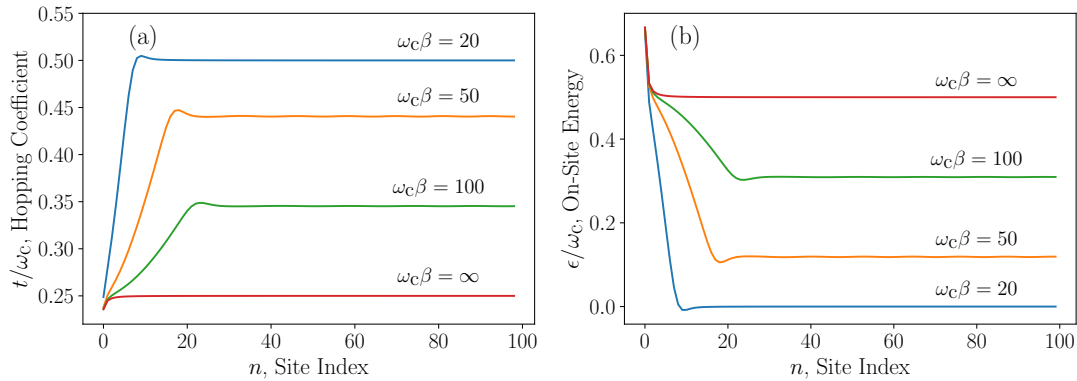


Figure 2.5: Chain parameters for an Ohmic spectral density with a hard cut-off $J(\omega) = 2\alpha\omega\theta(\omega - \omega_c)$ at different inverse temperatures. The hopping coefficients (a) and on-site energies (b) are independent of the coupling strength α .

Eq. (2.108), the chain parameters tend to asymptotic values given by [88]

$$\epsilon_\infty = \lim_{n \rightarrow \infty} \epsilon_n = \frac{\omega_{\max} + \omega_{\min}}{2}, \quad (2.109)$$

$$t_\infty = \lim_{n \rightarrow \infty} t_n = \frac{\omega_{\max} - \omega_{\min}}{4}. \quad (2.110)$$

In all cases where there is a hard cut-off we have $\omega_{\max} = \omega_c$, but ω_{\min} is temperature-dependent. In the zero temperature limit $\omega_{\min} = 0$, and thus we have asymptotic values $\epsilon_\infty = \omega_c/2$ and $t_\infty = \omega_c/4$; while in the high temperature limit $\omega_{\min} = -\omega_c$, and thus we have $\epsilon_\infty = 0$ and $t_\infty = \omega_c/2$. These asymptotic values hold for any spectral density belonging to the Szegő which covers a wide range of physical situations. This leads to the conclusion that the details which characterise a specific spectral density are encoded in a relatively small number of chain sites close to the system.

The combination of the chain mapping with the use of an extended bath is referred to in the literature as T-TEDOPA, for Thermal-TEDOPA. T-TEDOPA is related to the previously developed thermofield method [89]. The key difference is that in the thermofield approach, the positive and negative modes are separated into two independent nearest-neighbour chains, instead of being combined into one. The use of one chain in T-TEDOPA instead of two results in improved efficiency due to the smaller number of oscillators that need to be simulated as well as the reduced complexity of the tensor network structure in cases where there are multiple baths (See Ref. [87], Supplemental Material).

2.5 Constructing MPOs

In Sec. 2.2, when a time evolution method relied solely on an MPO decomposition of the Hamiltonian, we referred to that method as a ‘black box’ type method. This distinction

was based on the fact that an MPO may be generated automatically starting from an almost arbitrary 1D Hamiltonian via the generic MPO construction proposed by Hubig et al. [90]. This approach is based on the idea of first creating MPO representations of the individual operator terms that make up the Hamiltonian, and then adding them together to obtain an MPO for the total Hamiltonian. If one did only this, the resulting MPO would be extremely non-optimal, as the MPO bond dimension increases upon each addition. Hence, the vital step in the generic construction approach is the MPO compression that takes place after each addition. With the right choice of compression algorithm, for simple Hamiltonians with short-range, spatially homogeneous interactions, one can obtain exact MPO representations with optimal bond dimensions; while, for more complex Hamiltonians with medium ranged interactions, one obtains an MPO which is an optimal approximation for the Hamiltonian, and which would be difficult to obtain otherwise. Furthermore, user friendly codes which perform these algorithms are freely distributed online [91].

On the other hand, for many problems, the generic construction approach is unnecessarily complicated, since optimal MPOs can often be written directly from inspection of the Hamiltonian. This is true in particular for the nearest-neighbour type Hamiltonians which arise in the context of OQS (cf. Sec. 2.4.1). Another consideration is that, while, like all MPS/MPO algorithms, the generic MPO construction may be extended to tree-MPOs, at the time of writing, we are not aware of any openly available codes that implement this.

Since we make extensive use of nearest-neighbour tree-MPOs in this thesis, in this section, we provide some simple rules to facilitate their construction.

The generic Hamiltonian for which we want to construct an MPO is the following

$$\hat{H} = \sum_i \hat{H}_S^i + \sum_{\langle i,j \rangle_{\text{tree}}} \hat{J}_{i,j}, \quad (2.111)$$

where $\sum_{\langle i,j \rangle_{\text{tree}}}$ stands for the sum over all pairs of neighbouring sites on some given tree topology. The Hamiltonians \hat{H}_S^i are local to sites i and the interaction operators $\hat{J}_{i,j}$ act on both sites i and j . We assume that the interaction operators can always be written as a sum of products of local operators:

$$\hat{J}_{i,j} = \sum_{\alpha=1}^n \hat{h}_\alpha^{i \rightarrow j} \hat{h}_\alpha^{j \rightarrow i}, \quad (2.112)$$

where $\hat{h}_\alpha^{i \rightarrow j}$ acts locally on site i and $\hat{h}_\alpha^{j \rightarrow i}$ acts locally on site j .

In order to populate the MPO site tensors, we make use of the programming style, slice notation introduced in Sec. 2.2, Eq. (2.55). In addition, we will require the following extensions to this notation:

- The number ‘-1’ represents the largest value that the index can take

- The symbol ‘ \uparrow ’ indicates that the index is expanded in *increasing* index value order (this is identical to ‘:’)
- The symbol ‘ \downarrow ’ indicates that the index is expanded in *decreasing* index value order

For example, if M is a matrix given by:

$$M = \begin{pmatrix} 0 & 1 & 4 & 2 \\ 2 & -5 & -2 & 1 \\ 1 & 0 & 3 & 7 \\ 0 & -3 & 1 & 6 \end{pmatrix}, \quad (2.113)$$

two examples of slices specified with this notation are

$$M[\uparrow, 1] = \begin{pmatrix} 0 & 2 & 1 & 0 \end{pmatrix}, \quad M[-1, \downarrow] = \begin{pmatrix} 6 & 1 & -3 & 0 \end{pmatrix}. \quad (2.114)$$

Note that the distinction between a row vector and a column vector is not important here.

We demonstrate the construction of a tree-MPO via a simple example. Consider the following tree structure:

$$1 \text{ --- } 2 \text{ --- } 3 \begin{cases} \diagup 4 \text{ --- } 5 \\ \diagdown 6 \text{ --- } 7 \end{cases}. \quad (2.115)$$

To construct an MPO for the Hamiltonian \hat{H} with this tree topology the site tensors may be populated ‘bond by bond’ by specifying slices. For example, the MPO site tensor H^3 for the site $i = 3$ can be constructed as follows:

$$H^3[\uparrow, -1, 1, :, :, :] = \left(\hat{H}_S^3 \quad \hat{h}_1^{3 \rightarrow 2} \quad \hat{h}_2^{3 \rightarrow 2} \quad \dots \quad \hat{h}_n^{3 \rightarrow 2} \quad \hat{\mathbb{1}}^3 \right) \quad (2.116)$$

$$H^3[1, \downarrow, 1, :, :, :] = \left(\hat{H}_S^3 \quad \hat{h}_n^{3 \rightarrow 4} \quad \dots \quad \hat{h}_2^{3 \rightarrow 4} \quad \hat{h}_1^{3 \rightarrow 4} \quad \hat{\mathbb{1}}^3 \right) \quad (2.117)$$

$$H^3[1, -1, \uparrow, :, :, :] = \left(\hat{H}_S^3 \quad \hat{h}_1^{3 \rightarrow 6} \quad \hat{h}_2^{3 \rightarrow 6} \quad \dots \quad \hat{h}_n^{3 \rightarrow 6} \quad \hat{\mathbb{1}}^3 \right), \quad (2.118)$$

where we follow the index ordering conventions defined by Eq. (2.78) and where $\hat{\mathbb{1}}^j$ is the identity in the local Hilbert space of site j . When constructing tensors in this way, we assume that any tensor elements that are not explicitly specified are 0.

Each slice corresponds to a bond and contains half of the operators which make up the associated interaction Hamiltonian $\hat{J}_{i,j}$. For example, the parent leg of site 3 connects to site 2; the slice specified by Eq. (2.116), which expands along the parent bond index, therefore corresponds to the bond between the sites 3 and 2. Equation (2.117) meanwhile corresponds to the bond between 3 and 4, and Eq. (2.118) to the bond between 3 and 6.

The site tensors which connect to site 3 will need to contain complementary slices in order to complete the interaction terms. For example, H^2 is given by:

$$H^2[\uparrow, -1, :, :] = \left(\hat{H}_S^2 \hat{h}_1^{2 \rightarrow 1} \hat{h}_2^{2 \rightarrow 1} \dots \hat{h}_n^{2 \rightarrow 1} \hat{\mathbf{1}}^2 \right) \quad (2.119)$$

$$H^2[1, \downarrow, :, :] = \left(\hat{H}_S^2 \hat{h}_n^{2 \rightarrow 3} \dots \hat{h}_2^{2 \rightarrow 3} \hat{h}_1^{2 \rightarrow 3} \hat{\mathbf{1}}^2 \right). \quad (2.120)$$

Site 3 is the first (and only) child of site 2, thus the slice which connects to this site expands along the second index of H^2 .

Note that the ordering of the coupling operators \hat{h}_α depends on the direction of the arrow.

For any given slice, the direction of the arrow may be chosen arbitrarily, however, two rules must always be followed:

1. For a given MPO tensor, if an arrow is chosen to point upward for a slice along a particular index, that index must take the value 1 for all other slices; conversely, if the arrow is chosen to point downward, the index must take the value -1 for the other slices
2. Slices on neighbouring MPO tensors which correspond to the same bond must have oppositely orientated arrows.

Thus, in accordance with rule 2, the slice of site 2 which links to site 3 (Eq. (2.120)) has a downward arrow and the slice of site 3 which links to site 2 (Eq. (2.116)) has an upward arrow.

In the expressions above, the operators fill in the physical indices of the site tensors. We use the colon notation to expand these indices as they will always be expanded in the normal, increasing index value, order.

Using these rules, it is easy to construct nearest-neighbour MPOs for arbitrary tree geometries. The MPO bond-dimension will be $w = n + 2$, which is optimal. Adding simple long range interaction terms into this approach is also relatively straight forward (See for example Ref. [19]), although we will not explicitly demonstrate that here.

2.6 Code - MPSDynamics.jl

The code used to carry out the tensor network simulations presented in this thesis was written in Julia and is available, along with usage instructions and documentation, on GitHub [92]. The exponentiations of the effective local Hamiltonians were implemented using the KrylovKit.jl package, and tensor contractions were implemented with the TensorOperations.jl package [93].

2.A Appendix - Chain mapping

The chain mapping used in Sec. 2.4 is based on the theory of orthogonal polynomials. A polynomial of degree n is defined by

$$p_n(x) = \sum_{m=0}^n a_m x^m. \quad (2.121)$$

The space of polynomials of degree n is denoted \mathbb{P}_n and is a subset of the space of all polynomials $\mathbb{P}_n \subset \mathbb{P}$. Given a measure $d\mu(x)$ which has finite moments of all orders on some interval $[a, b]$, we may define the inner product of two polynomials

$$\langle p, q \rangle_\mu = \int_a^b d\mu(x) p(x) q(x). \quad (2.122)$$

This inner product gives rise to a unique set of orthonormal polynomials $\{\tilde{p}_n \in \mathbb{P}_n, n = 0, 1, 2, \dots\}$ which all satisfy

$$\langle \tilde{p}_n, \tilde{p}_m \rangle = \delta_{n,m}. \quad (2.123)$$

This set forms a complete basis for \mathbb{P} , and more specifically the set $\{\tilde{p}_n \in \mathbb{P}_n, n = 0, 1, 2, \dots, m\}$ is a complete basis for $\bigcup_{r=1}^m \mathbb{P}_r$.

It is often useful to express the orthonormal polynomials in terms of the orthogonal *monic* polynomials $\pi_n(x)$ which are the unnormalized scalar multiples of $\tilde{p}_n(x)$ whose leading coefficient is 1 ($a_n = 1$)

$$\tilde{p}_n(x) = \frac{\pi_n(x)}{\|\pi_n\|}. \quad (2.124)$$

The key property of orthogonal polynomials for the construction of the chain mapping is that they satisfy a three term recurrence relation

$$\pi_{k+1}(x) = (x - \alpha_k)\pi_k(x) - \beta_k\pi_{k-1}(x), \quad (2.125)$$

where it can be easily shown that

$$\alpha_k = \frac{\langle x\pi_k, \pi_k \rangle}{\langle \pi_k, \pi_k \rangle}, \beta_k = \frac{\langle \pi_k, \pi_k \rangle}{\langle \pi_{k-1}, \pi_{k-1} \rangle}. \quad (2.126)$$

Now that we have defined the orthogonal polynomials we may use them to construct the unitary transformation that will convert the star Hamiltonian $H^{\text{star}} = \hat{H}_S + \hat{H}_1^{\text{star}} + \hat{H}_B^{\text{star}}$ with

$$H_1^{\text{star}} = \hat{A} \otimes \int_{-\infty}^{\infty} d\omega \sqrt{J(\omega)} (b_\omega + b_\omega^\dagger), H_B^{\text{star}} = \int_{-\infty}^{\infty} d\omega \omega b_\omega^\dagger b_\omega, \quad (2.127)$$

into the chain Hamiltonian H^{chain} . We have dropped the bath index α as the chain mapping can be applied to each bath independently. The transformation is given by

$$c_n^{(\dagger)} = \int_{-\infty}^{\infty} U_n(\omega) b_\omega^{(\dagger)}, \quad (2.128)$$

where

$$U_n(\omega) = \sqrt{J(\omega)} \tilde{p}_n(\omega) = \sqrt{J(\omega)} \frac{\pi_n(\omega)}{\|\pi_n\|}, \quad (2.129)$$

and the polynomials $\tilde{p}_n(\omega)$ are orthonormal with respect to the measure $d\omega J(\omega)$. The unitarity of $U_n(\omega)$ follows immediately from the orthonormality of the polynomials.

Applying the above transformation to the interaction Hamiltonian we have

$$H_I^{\text{chain}} = \hat{A} \otimes \sum_{n=0}^{\infty} \int_{-\infty}^{\infty} d\omega J(\omega) \frac{\pi_n(\omega)}{\|\pi_n\|} (c_n^\dagger + c_n) \quad (2.130)$$

For the zeroth order monic polynomial we have $\pi_0 = 1$ and so we may insert this into the above expression

$$H_I^{\text{chain}} = \hat{A} \otimes \sum_{n=0}^{\infty} \int_{-\infty}^{\infty} d\omega J(\omega) \frac{\pi_n(\omega) \pi_0}{\|\pi_n\|} (c_n^\dagger + c_n). \quad (2.131)$$

Recognising the inner product in the above expression and making use of the orthogonality of the polynomials we have

$$H_I^{\text{chain}} = \hat{A} \otimes \sum_{n=0}^{\infty} \|\pi_n\| \delta_{n,0} (c_n^\dagger + c_n) = \hat{A} \otimes \|\pi_0\| (c_0^\dagger + c_0), \quad (2.132)$$

and thus, in the new basis, only one mode couples to the system.

Now, for the environment part of the Hamiltonian we have

$$H_B^{\text{chain}} = \sum_{n,m=0}^{\infty} \int_{-\infty}^{\infty} d\omega J(\omega) \omega \frac{\pi_n(\omega) \pi_m(\omega)}{\|\pi_n\| \|\pi_m\|} c_n^\dagger c_m. \quad (2.133)$$

Substituting for $\omega \pi_n(\omega)$ from the three term recurrence relation of Eq. (2.125) yields

$$H_B^{\text{chain}} = \sum_{n,m=0}^{\infty} \int_{-\infty}^{\infty} d\omega \frac{J(\omega)}{\|\pi_n\| \|\pi_m\|} \left[\pi_{n+1}(\omega) + \alpha_n \pi_n(\omega) + \beta_n \pi_{n-1}(\omega) \right] \pi_m(\omega) c_n^\dagger c_m. \quad (2.134)$$

Again, evaluating the inner products and making use of orthogonality we have

$$\begin{aligned} H_B^{\text{chain}} &= \sum_{n,m=0}^{\infty} \frac{1}{\|\pi_n\|} \left[\|\pi_m\| \delta_{n+1,m} + \alpha_n \|\pi_m\| \delta_{n,m} + \beta_n \|\pi_m\| \delta_{n-1,m} \right] c_n^\dagger c_m \\ &= \sum_{n=0}^{\infty} \sqrt{\beta_{n+1}} c_n^\dagger c_{n+1} + \alpha_n c_n^\dagger c_n + \sqrt{\beta_{n+1}} c_n^\dagger c_{n-1}, \end{aligned} \quad (2.135)$$

where in the second line we have used the fact that

$$\frac{\|\pi_{n+1}\|}{\|\pi_n\|} = \sqrt{\beta_{n+1}}. \quad (2.136)$$

We thus arrive at the nearest-neighbour coupling Hamiltonian of Eq. (2.88) and (2.87), and are able to identify the chain coefficients as

$$\begin{aligned}\kappa &= \|\pi_0\|, \\ \epsilon_{n+1} &= \alpha_n, \\ t_n &= \sqrt{\beta_n}.\end{aligned}\tag{2.137}$$

All that remains now, to calculate the chain coefficients for a particular spectral density $J(\omega)$, is to compute the recurrence coefficients α_n and β_n . This may be done iteratively using Eq. (2.125) and (2.126) and numerically evaluating the inner product integrals using a quadrature rule. All chain parameters used in this thesis were generated using the ORTHPOL package [94].

Chapter 3

Models

In this chapter we will apply our tensor network methodology to a number of generic OQS models.

3.1 Independent Boson Model

In this section we verify the accuracy of the methods described in the previous chapter by comparing against an exactly solvable OQS problem. The following derivation follows Ref. [12].

The OQS Hamiltonian is exactly solvable when the system Hamiltonian commutes with the system interaction operator, i.e. when $[\hat{H}_S, \hat{A}_S] = 0$. The problem is then most naturally solved in the interaction picture as the interaction operator is constant in time: $\hat{A}_S(t) = \hat{A}_S$. For simplicity we consider Eq. (2.79) in the case of a single bosonic bath

$$\hat{H} = \hat{H}_S + \overbrace{\hat{A}_S \otimes \sum_k g_k (b_k^\dagger + b_k)}^{\hat{H}_I} + \overbrace{\sum_k \omega_k b_k^\dagger b_k}^{\hat{H}_B}. \quad (3.1)$$

The interaction picture propagator is

$$U(t) = T_{\leftarrow} \exp \left(-i \int_0^t ds \hat{H}_I(s) \right), \quad (3.2)$$

where the time evolved interaction Hamiltonian is given by

$$\hat{H}_I(s) = \hat{A}_S \otimes \sum_k g_k (b_k^\dagger e^{i\omega_k s} + b_k e^{-i\omega_k s}). \quad (3.3)$$

The time-ordered exponential of Eq. (3.2) may be expanded using a Magnus series:

$$U(t) = \exp \left(-i \int_0^t ds \hat{H}_I(s) \right) \exp \left(-\frac{1}{2} \int_0^t ds \int_0^s ds' [\hat{H}_I(s), \hat{H}_I(s')] \right). \quad (3.4)$$

The series terminates at the second order term since the commutator $[\hat{H}_I(s), \hat{H}_I(s')]$ is simply \hat{A}_S^2 times a c-number:

$$[\hat{H}_I(s), \hat{H}_I(s')] = -2i\hat{A}_S^2 \sum_k g_k^2 \sin(\omega_k(s - s')). \quad (3.5)$$

Then, evaluating the integrals in Eq. (3.4) we have

$$U(t) = \exp\left(\hat{A}_S \sum_k \left(\alpha_k(t)b_k^\dagger - \alpha_k^*(t)b_k\right)\right) \exp\left(-i\hat{A}_S^2\theta(t)\right), \quad (3.6)$$

where

$$\alpha_k(t) = \frac{g_k(1 - e^{i\omega_k t})}{\omega_k}, \quad (3.7)$$

and

$$\theta(t) = \sum_k \frac{2g_k^2}{\omega_k^2} (\omega_k t - \sin(\omega_k t)). \quad (3.8)$$

The second integral in Eq. (3.6) is simply a time-dependent phase factor while the first can be recognised as a displacement operator which acts on all bath modes with the time-dependent parameter $\alpha_k(t)$. Both factors contain the time-independent system operator \hat{A}_S which introduces a dependence on the system's initial state.

Specialising to the case where the system is a two-level system (TLS) with

$$\hat{H}_S = \frac{\omega_0}{2}\sigma_z \text{ and } \hat{A}_S = \frac{\sigma_z}{2}, \quad (3.9)$$

we obtain the independent boson model (IBM). For a factorising initial condition $\rho(0) = \rho_S \otimes \rho_B$ where ρ_B is the initial density matrix of the bath and ρ_S is the initial density matrix for the system, the dynamics are given by

$$U(t) |\uparrow_z\rangle \otimes |\phi\rangle = e^{-i\theta(t)} |\uparrow_z\rangle \otimes \prod_k \hat{D}(+\alpha_k(t)/2) |\phi\rangle, \quad (3.10)$$

$$U(t) |\downarrow_z\rangle \otimes |\phi\rangle = e^{-i\theta(t)} |\downarrow_z\rangle \otimes \prod_k \hat{D}(-\alpha_k(t)/2) |\phi\rangle, \quad (3.11)$$

where $|\phi\rangle$ is an arbitrary bath state and where the operator $\hat{D}(\alpha_k)$ is the displacement operator of bath mode k :

$$\hat{D}(\alpha_k) = \exp\left(\alpha_k b_k^\dagger - \alpha_k^* b_k\right). \quad (3.12)$$

From Eq. (3.10) and (3.11) it is clear that the populations of the system's reduced density matrix will be constant:

$$\rho_{\uparrow\uparrow}(t) \equiv \langle \uparrow_z | \text{Tr}_B \{\rho(t)\} | \uparrow_z \rangle = \langle \uparrow_z | \rho_S | \uparrow_z \rangle \equiv \rho_{\uparrow\uparrow}(0) \quad (3.13)$$

$$\rho_{\downarrow\downarrow}(t) \equiv \langle \downarrow_z | \text{Tr}_B \{\rho(t)\} | \downarrow_z \rangle = \langle \downarrow_z | \rho_S | \downarrow_z \rangle \equiv \rho_{\downarrow\downarrow}(0). \quad (3.14)$$

For the coherence terms on the other hand we have:

$$\rho_{\uparrow\downarrow}(t) \equiv \langle \uparrow_z | \text{Tr}_B \{ \rho(t) \} | \downarrow_z \rangle \quad (3.15)$$

$$= \langle \uparrow_z | \rho_S | \downarrow_z \rangle \text{Tr}_B \left\{ \prod_k \hat{D}(\alpha_k(t)) \rho_B \right\} \quad (3.16)$$

$$= \rho_{\uparrow\downarrow} \prod_k \left\langle \hat{D}(\alpha_k(t)) \right\rangle_{\rho_B}. \quad (3.17)$$

and

$$\rho_{\downarrow\uparrow}(t) = \rho_{\uparrow\downarrow}^*(t). \quad (3.18)$$

We see that the time-dependent phase factors $e^{-i\theta(t)}$ cancel out in the expressions for the coherences.

If the bath is initially in a thermal state with inverse temperature β , i.e. if $\rho_B = \frac{1}{Z} \exp(-\beta \hat{H}_B)$, the expectation values in Eq. (3.17) become thermal expectation values: $\langle \cdot \rangle_{\rho_B} \rightarrow \langle \cdot \rangle_\beta$. We can therefore make use of the following result for the thermal expectation value of the displacement operator:

$$\langle \hat{D}(\alpha_k) \rangle_\beta = \exp \left(-\frac{1}{2} |\alpha_k|^2 \coth \left(\frac{\omega_k \beta}{2} \right) \right). \quad (3.19)$$

Substituting this result into Eq. (3.17) we have

$$\rho_{\uparrow\downarrow}(t) = \rho_{\uparrow\downarrow} \prod_k \exp \left(-\frac{g_k^2}{\omega_k^2} (1 - \cos(\omega_k t)) \coth \left(\frac{\omega_k \beta}{2} \right) \right) \quad (3.20)$$

$$= \rho_{\uparrow\downarrow} \exp \left(-\sum_k \frac{g_k^2}{\omega_k^2} (1 - \cos(\omega_k t)) \coth \left(\frac{\omega_k \beta}{2} \right) \right), \quad (3.21)$$

and switching to a description in terms of a continuous spectral density (cf. Sec. 2.4, Eq. (2.85)):

$$\rho_{\uparrow\downarrow}(t) = \rho_{\uparrow\downarrow} \exp \left(-\int_0^\infty d\omega \frac{J(\omega)}{\omega^2} (1 - \cos(\omega t)) \coth \left(\frac{\omega \beta}{2} \right) \right). \quad (3.22)$$

Finally, incorporating the bare system dynamics yields

$$\langle \sigma_x \rangle = \cos(\omega_0 t) \text{Re}\{\rho_{\uparrow\downarrow}(t)\}, \quad \langle \sigma_y \rangle = \sin(\omega_0 t) \text{Re}\{\rho_{\uparrow\downarrow}(t)\}. \quad (3.23)$$

In Fig. 3.1 we compare the analytical solution derived above for an Ohmic spectral density

$$J(\omega) = 2\alpha\omega\theta(\omega - \omega_c), \quad (3.24)$$

with T-TEDOPA for a range of coupling strengths and inverse temperatures. We used $\mathcal{N}_m = 50$ chain sites and found converged results for $\omega_c \beta = 10$ and $\omega_c \beta = 100$ with MPS bond dimension $D_{\max} = 6$ and $d = 6$ Fock states for each harmonic oscillator; while, for the hotter bath with $\omega_c \beta = 1$ we required $d = 10$. The time required to perform each run was very short (~ 5 mins). The agreement between T-TEDOPA and the exact solution is very good over the parameter range tested, which includes the transition from under-damped to over-damped oscillations induced by increasing either the temperature or the coupling strength.

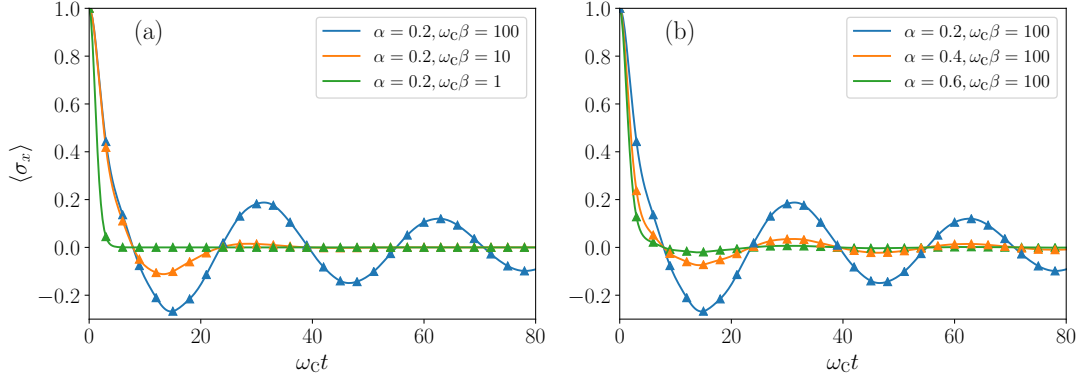


Figure 3.1: Comparison of T-TEDOPA with the exact solution for the Ohmic independent boson model (IBM). The exact solution is represented with solid lines, while the T-TEDOPA dynamics are depicted with triangles. Increasing the temperature (a) or the coupling strength (b) leads to damping of the oscillations.

3.2 Spin-Boson Model

In this section we will examine the Ohmic spin-boson model (SBM). This will serve as a further verification of T-TEDOPA, and demonstrate that it is effective in highly non-perturbative and non-markovian regimes.

The spin-boson model is defined by the following Hamiltonian [95]

$$\hat{H} = \underbrace{\frac{\epsilon\sigma_z}{2} - \frac{\Delta\sigma_x}{2}}_{\hat{H}_S} + \underbrace{\frac{\sigma_z}{2}}_{\hat{A}_S} \otimes \sum_k g_k (b_k^\dagger + b_k) + \sum_k \omega_k b_k^\dagger b_k. \quad (3.25)$$

We use the same form for the spectral density as in the previous section

$$J(\omega) = 2\alpha\omega\theta(\omega - \omega_c). \quad (3.26)$$

The SBM consists of a spin- $\frac{1}{2}$ linearly coupled to a bosonic bath; however, the applicability of this model extends far beyond spin systems: the spin states $|\uparrow_z\rangle$ and $|\downarrow_z\rangle$ can be considered as the values of any abstract, binary, quantum coordinate. Thus, for example, the two states could represent reactant and product states in chemical reactions, the physical location of an electron or proton tunnelling between donor and acceptor sites, or even the strangeness of a neutral K meson when modelling neutrino oscillations. In the SBM, the binary coordinate is coupled to a continuous quantum coordinate $\hat{q} = \sum_k b_k^\dagger + b_k$ leading to the double well structure shown in Fig. 3.2. In the figure we represent the coordinate \hat{q} heuristically as the scalar coordinate q , although one must bear in mind that \hat{q} is in fact multi-dimensional, and describes the displacements of a large number of harmonic oscillators. The parameter Δ represents the probability

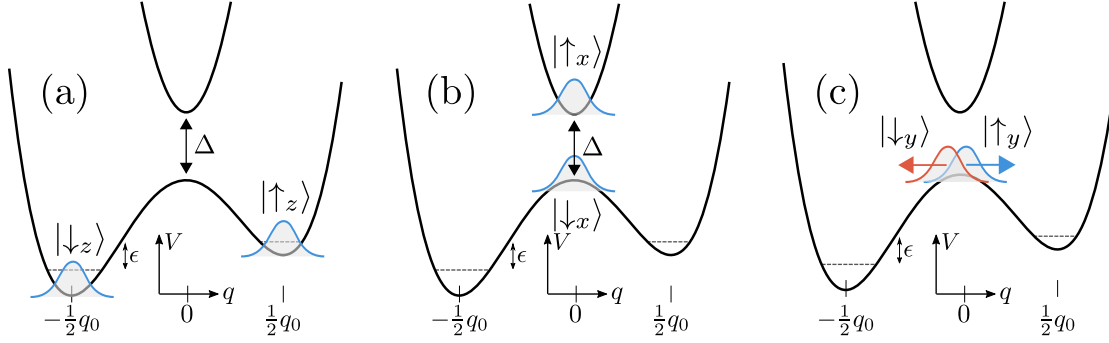


Figure 3.2: Potential energy surfaces of the SBM and the different initial spin states which are possible. The parameter ϵ gives the ground state energy level offset between the wells, and Δ gives the probability of tunnelling. The spin states along the z axis (a) correspond to states localised in one of the two wells. The spin states along x (b) represent delocalised states which have no momentum towards either well. The spin states along y (c) are also delocalised but have a momentum in the z direction which will cause them to move towards one of the two wells.

for tunnelling, while ϵ is the difference in energy between the ground states of the two wells.

In the zero tunnelling limit ($\Delta = 0$), the model reduces to the IBM considered in the previous section and thus admits an exact solution. In this section we will consider the opposite limit: that of zero detuning $\epsilon = 0$ (Fig. 3.3), in which there is a finite tunnelling matrix element but no offset between the ground state energies of the two wells. In this limit the system Hamiltonian and interaction operator clearly do not commute and thus an exact solution is not possible.

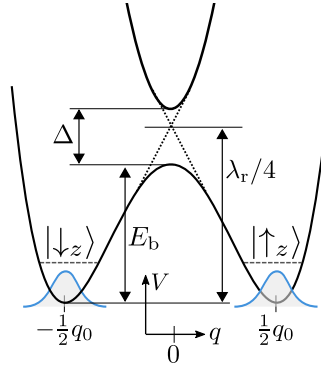


Figure 3.3: Potential energy surfaces in the case of zero detuning ($\epsilon = 0$).

Figures 3.2(a)-(c) depict the different initial conditions that are possible for the SBM. In the zero detuning limit we have $[\sigma_z, \hat{H}_S] \propto \sigma_y$; thus, the bare system evolution in the interaction picture is given by $\dot{\sigma}_z \propto \sigma_y$. The y coordinate can thus be viewed as a kind

of velocity, or momentum, in the z direction. Thus, the initial condition $|\uparrow_y\rangle$ has a momentum towards the right well ($|\uparrow_z\rangle$), while the state $|\downarrow_y\rangle$ has a momentum towards the left well ($|\downarrow_z\rangle$).

The two wells are separated by an energy barrier of height E_b as shown in Fig. 3.3, whose height is given by

$$E_b = \frac{\lambda_R}{4} - \frac{\Delta}{2}, \quad (3.27)$$

where λ_R is the reorganisation energy. The reorganisation energy is the energy required to displace each bath oscillator k by $\frac{g_k}{\omega_k}$ and is given by

$$\lambda_R = \int_0^\infty d\omega \frac{J(\omega)}{\omega}. \quad (3.28)$$

Of course, the existence of the barrier, and hence the two-well structure, requires that the tunnelling parameter Δ is not too large in comparison with the reorganisation energy. The reorganisation energy for an Ohmic bath is

$$\lambda_R = 2\alpha\omega_c, \quad (3.29)$$

which leads to the condition $\alpha > \Delta$ for a positive barrier height.

3.2.1 Thermalisation

We will first consider the initial condition $|\uparrow_x\rangle$ (Fig. 3.2(b)). This state is completely delocalised across the two wells and has no projection onto the z axis. Furthermore, since the projection onto the y axis is also zero, there is no momentum in the z direction; hence, the system will have no tendency to move towards one well or the other and will instead remain balanced on the cusp between the two. As a result, the dynamics will be entirely confined to the x direction.

The states $|\uparrow_x\rangle$ and $|\downarrow_x\rangle$ are separated by an energy gap Δ ; the coupling operator σ_z induces transitions between these two states causing population transfer and eventually a relaxation to thermal equilibrium. In the perturbative, weak-coupling limit, where ($\alpha \ll 1$), the steady state populations would be determined by the temperature T and the energy gap Δ according to the Gibbs-Boltzmann distribution

$$\langle \sigma_x(t \rightarrow \infty) \rangle = \frac{(e^{-\Delta/T} - 1)}{(e^{-\Delta/T} + 1)}. \quad (3.30)$$

The coupling strength α would only control the rate at which this steady state is obtained. However, in the strong coupling regime, a non-perturbative effect gives rise to a dependence of the steady state populations on the coupling strength, as can be seen in Fig. 3.4(a). This non-perturbative effect is the formation of polarons, i.e. states that mix electronic and bosonic degrees of freedom. Polaron formation leads to a renormalisation of the energy gap $\Delta \rightarrow \Delta_r$, which, according to the strong coupling theory of Silbey and Harris, [96] is given approximately by

$$\Delta_r = \Delta \left(\frac{\Delta}{\omega_c} \right)^{\frac{\alpha}{1-\alpha}}. \quad (3.31)$$

At critical coupling $\alpha_c = 1$ this renormalisation is capable of completely closing the energy gap, leading to the localisation transition which will be discussed below. The above result is derived in the scaling limit, i.e. when the cut-off frequency ω_c is much larger than all other frequencies ($\Delta \ll \omega_c$). In numerical simulations, it is difficult to obtain results deep in the scaling limit as one would have to propagate to very long times in order to capture the full dynamics. For the same reason, it is also difficult to obtain results deep in the weak-coupling limit. When performing comparisons it is therefore necessary to account for this, and it is common in the literature to do so by using a re-scaled coupling strength $\bar{\alpha} = c\alpha$ when evaluating Eq. (3.31), where c is a fitting parameter [97, 98, 99]. For the results presented in this section we took $\Delta = 0.2\omega_c$.

Taking the renormalised energy gap into account, the steady state values become

$$\langle \sigma_x(t \rightarrow \infty) \rangle = \left(\frac{\Delta_r}{\Delta} \right) \frac{(e^{-\Delta_r/T} - 1)}{(e^{-\Delta_r/T} + 1)}, \quad (3.32)$$

where the prefactor in Eq. (3.32) takes account of the suppressed expectation values of σ_x in the polaronic eigenbasis. In Fig. 3.5 we compare this analytic result with the steady state values extracted from the simulations and find good agreement across the parameter space sampled.

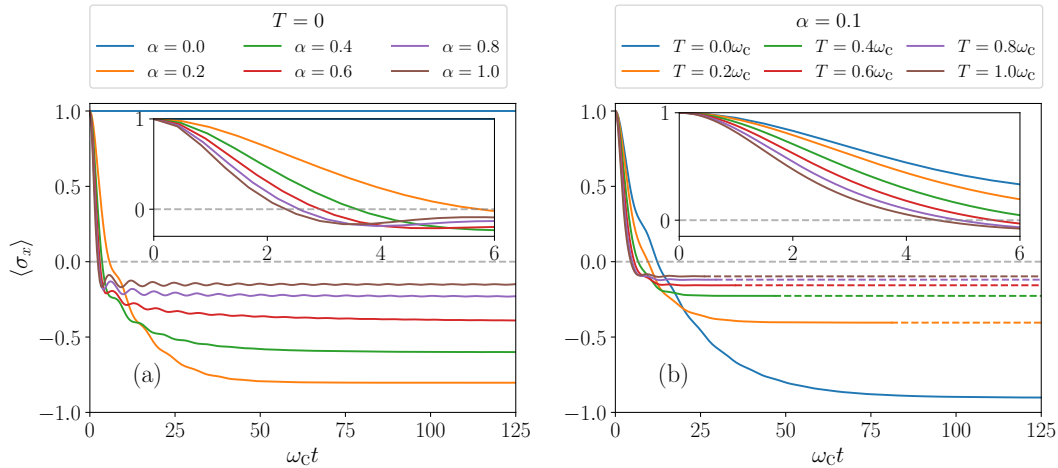


Figure 3.4: Dynamics of $\langle \sigma_x \rangle$ in the SBM for the initial TLS state $|\uparrow_x\rangle$. The dynamics were simulated until the attainment of a steady state; the dotted lines in panel (b) indicate where the results have been extrapolated.

3.2.2 Rabi Oscillations

A further non-perturbative effect that can be seen in the dynamics of σ_x are the oscillations which the system undergoes in reaching its steady state. Such oscillations are not predicted by weak-coupling theories, which instead suggest a simple exponential decay

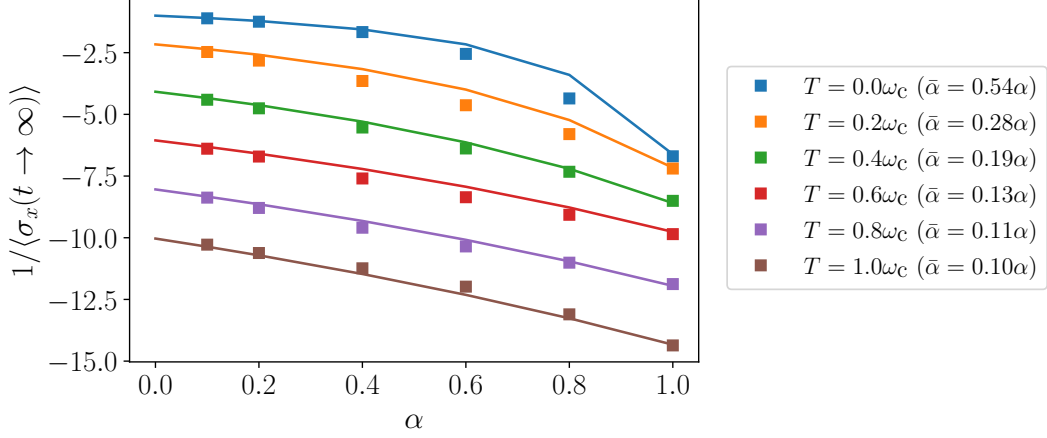


Figure 3.5: Comparison of the Silbey and Harris strong coupling theory against T-TEDOPA. We plot the inverse of the steady state values in order to better distinguish the curves. The values of the scaling parameter c are shown in the legend for the different temperatures.

defined by a single rate. The frequency of these oscillations seems to have a dependence on both temperature and coupling strength, which motivates an explanation in terms of Rabi oscillations. Rabi oscillations occur when a two-level system interacts with a harmonic mode whose frequency ω_a is close to the TLS gap. When a TLS interacts with a continuum of bath modes, the dominate contribution will come from the bath mode that resonates with the TLS.

A simple model that is often used for understanding Rabi oscillations is the Jaynes-Cummings model [100], defined by the following Hamiltonian

$$\hat{H} = \frac{\omega_a - \delta}{2} \sigma_z - \lambda(\sigma_+ a + \sigma_- a^\dagger) + \omega_a a^\dagger a, \quad (3.33)$$

where δ is known as the *detuning* and represents the difference between the TLS gap (here Δ) and the oscillator frequency ($\delta = \omega_a - \Delta$). The above Hamiltonian can be obtained from the SBM Hamiltonian (Eq. (3.25)) by replacing the continuum of bath modes with a single mode and making the rotating-wave approximation. Note that in going from the SBM Hamiltonian to the one above, we have also performed the rotation: $x \mapsto z$, $z \mapsto -x$ so that the system part is diagonal. The Jaynes-Cummings Hamiltonian is number-conserving, meaning that the total number of excitations in the TLS and the mode, which we will denote by n , is constant. Considering the zero temperature limit, where the mode is initially unoccupied, and the TLS is initially in its excited state, i.e.,

$$|\psi(0)\rangle = |\uparrow_z\rangle \otimes |0\rangle, \quad (3.34)$$

the dynamics will be confined to the one-excitation sub-space:

$$|\psi(t)\rangle = a_0(t) |\uparrow_z\rangle |0\rangle + a_1(t) |\downarrow_z\rangle |1\rangle. \quad (3.35)$$

One finds that the TLS populations oscillate with a frequency Ω_R known as the Rabi frequency:

$$|a_0(t)|^2 = \frac{1}{2}(1 + \cos(\Omega_R(n=1)t)), \quad (3.36)$$

where the Rabi frequency is given by

$$\Omega_R = \sqrt{\delta^2 + 4\lambda^2 n}. \quad (3.37)$$

As mentioned above, in the case of a continuum of modes, the resonant mode will be dominant. We can thus take $\delta = 0$ in Eq. (3.37) to obtain the following approximation for the oscillation frequency:

$$\Omega \approx 2\lambda. \quad (3.38)$$

Since our original model was one of a continuum of modes, it is difficult to determine a precise value for λ . However, we can see that, for the Ohmic spectral density Eq. (3.26), its dependence on the coupling strength α will be the following:

$$\lambda \propto \sqrt{\alpha}, \quad (3.39)$$

which leads to the prediction that the oscillation frequency, at $T = 0$, will increase with the square root of the coupling strength.

In Fig. 3.6 we confirm this prediction by plotting the oscillation frequencies extracted from the dynamics shown in Fig. 3.4(a) against the coupling strengths.

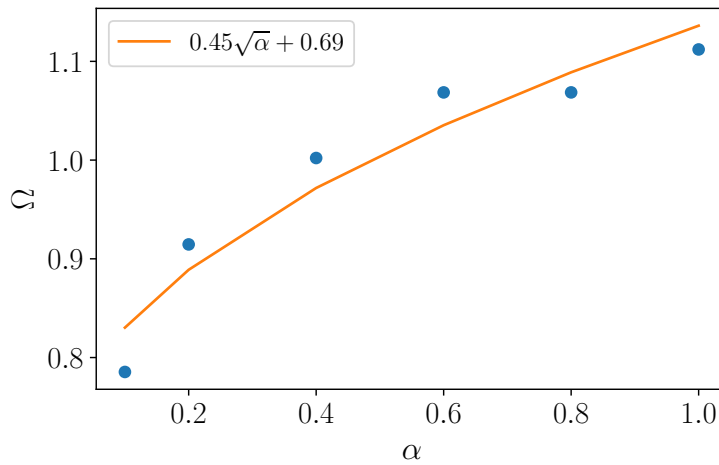


Figure 3.6: The frequency Ω of the oscillations in $\langle \sigma_x \rangle$ is plotted against the coupling strength α (blue dots). A good fit to a square-root curve is obtained (orange line), supporting the explanation in terms of Rabi oscillations.

At non-zero temperature the situation will be more complicated: as the oscillator modes will be thermally occupied, many Rabi frequencies, corresponding to the different excitation numbers involved, will be present [100]. We can expect these different

frequencies to interfere destructively, leading to a reduction in the amplitude of the oscillations. This finite temperature effect can be best seen in Fig. 3.7, which plots the decay of $\langle\sigma_x\rangle$ for different temperatures with $\alpha = 1.0$ - the coupling strength which gives the strongest oscillations at zero temperature.

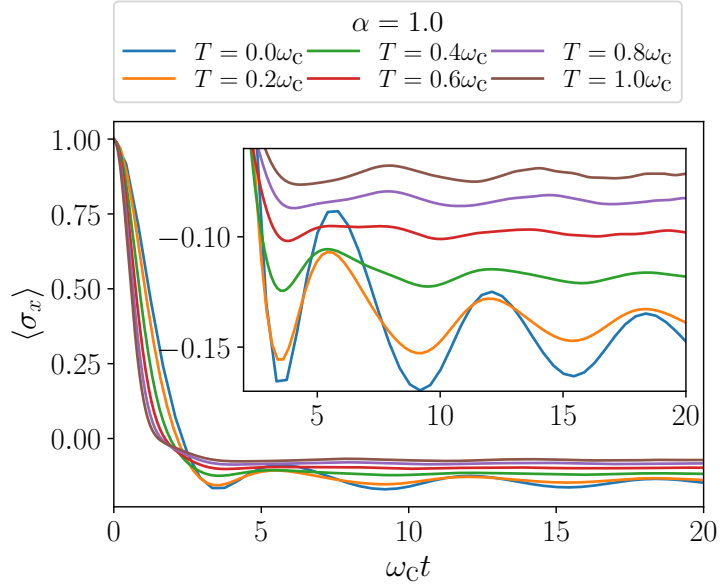


Figure 3.7: The dynamics of $\langle\sigma_x\rangle$ with the initial condition $|\uparrow_x\rangle$ for $\alpha = 1$ at a range of temperatures. The amplitude of the Rabi oscillations diminishes as temperature increases, as explained in the text.

3.2.3 Localisation Transition

To fully understand the dynamics of the SBM it is necessary to consider two other initial conditions: $|\uparrow_z\rangle$ and $|\uparrow_y\rangle$ (Fig. 3.2(a) and (c)). These correspond, respectively, to the system localised in the right-hand well, and the system delocalised across the two wells but with a velocity towards the right-hand well. From the evolutions of these three initial conditions it is possible to recreate the complete dynamical map, allowing the system to be evolved from any arbitrary initial density matrix, which may also be mixed.

The zero temperature results for both these initial conditions are collected in Fig. 3.8. The dynamics of $\langle\sigma_x\rangle$, are very similar to those presented in the previous sub-section for the initial condition $|\uparrow_x\rangle$; specifically, we see a decay with Rabi oscillations to the same steady states. The fact that the steady states are the same for $\langle\sigma_x\rangle$ is expected, since the main characteristic of thermalisation is that any information regarding the initial state is lost.

Turning our attention to $\langle\sigma_z\rangle$ and $\langle\sigma_y\rangle$ we come across what is perhaps the most

striking feature of the Ohmic SBM at zero temperature: the localisation transition [95]. As explained in Sec. 3.2.1, at critical coupling $\alpha_c = 1$ the renormalised tunnelling matrix element goes to zero ($\Delta_r \rightarrow 0$) causing the system to become stuck in one of the wells. In Fig. 3.8(a) we see that, with the system starting in the right-hand well, with sub-critical coupling $\alpha < \alpha_c$, the system tends towards a delocalised steady state: $\langle \sigma_z(t \rightarrow \infty) \rangle = 0$. For low values of α there exists oscillations in $\langle \sigma_z \rangle$ which become increasingly damped as we increase α . The dynamics are expected to become incoherent for $\alpha > 0.5$ [16]. At critical coupling $\alpha = \alpha_c$, the decay ceases entirely and $\langle \sigma_z \rangle$ has a finite steady state value, i.e., is localised in the right-hand well. The dynamics of $\langle \sigma_y \rangle$ shown in Fig. 3.8(b) give a complementary picture of the system's tunnelling. As discussed above, $\langle \sigma_y \rangle$ can be seen as the tunnelling velocity; thus, as the system begins in the right-hand well, the velocity, which is initially zero, becomes negative (towards the left-hand well), and later settles to zero when the steady state is reached.

The localisation transition is also apparent when starting from the state $|\uparrow_y\rangle$. Here, the system's initial state is delocalised but there is a velocity towards the right-hand well causing the system to move in that direction. Again, below critical coupling, the system will tunnel back and become delocalised but at critical coupling the system becomes stuck in the right-hand well.

It is important to note that, at critical coupling, in contrast to the thermalisation dynamics of $\langle \sigma_x \rangle$, the system is non-ergodic; that is, the steady state of $\langle \sigma_z \rangle$ and $\langle \sigma_y \rangle$ is initial state dependent. For example, if the system began in the left-hand well ($|\downarrow_z\rangle$), or had a velocity towards the left-hand well ($|\downarrow_y\rangle$), then the steady state would be localised in the left-hand well.

As can be seen from Fig. 3.9, the localisation transition is no longer present at finite temperature as predicted in Ref.[95, 16].

Data Availability

A full data set for the Ohmic SBM, from the which the results presented in this section have been selected, has been published online and can be found at Ref. [101]. These data sample a large part of the $\alpha - \beta$ parameter space and contain sufficient information to construct the complete dynamical map - allowing a TLS to be propagated from any arbitrary initial condition, including mixed states. Some of these data have also been presented in Dunnett and Chin [102].

3.3 Electron transfer

In the previous section we introduced the spin-boson model as a generic model for a dissipative two-state system and explored its non-perturbative dynamics, including Rabi oscillations and the localisation transition. In the present section we will continue to study the SBM but now specifically from the point of view of electron transfer (ET). Electron transfer is a fundamental problem in chemical dynamics and plays an essential role in a vast variety of crucial processes including the ultra-fast primary electron transfer

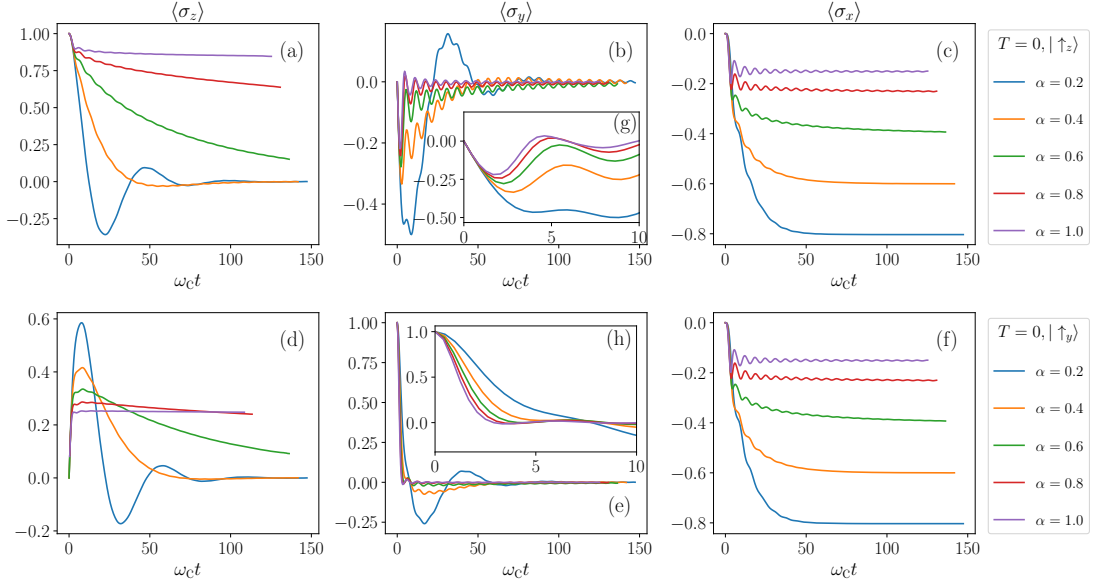


Figure 3.8: Zero temperature tunnelling dynamics of the Ohmic SBM for a range of coupling strengths. Panels (a), (b) and (c) refer to the initial condition $|\uparrow_z\rangle$, and panels (d), (e) and (f) refer to the initial condition $|\uparrow_y\rangle$. Panels (a) and (d) show $\langle\sigma_z\rangle$, (b) and (e) show $\langle\sigma_y\rangle$, and (c) and (f) show $\langle\sigma_x\rangle$. The insets (g) and (h) are close-ups of the fast initial decay of $\langle\sigma_y\rangle$.

step in photosynthetic reaction centers and the electron transport that powers biological respiration [103, 104, 105].

In the previous section the spin states $|\downarrow_z\rangle$ and $|\uparrow_z\rangle$ had no concrete meaning; here we take them to be, respectively, the donor $|D\rangle$ and acceptor $|A\rangle$ states of the ET reaction. Usually in the ET reaction the transfer of the electron from the donor to the acceptor state is impeded by a barrier whose energy must be overcome for the reaction to progress. The presence of the barrier is due to the fact that the ET states are *solvated*, i.e. are coupled to their solvent environment. Overcoming the barrier requires a *reorganisation* of the solvent environment; the energy required to perform this reorganisation is the reorganisation energy λ_R . Within the SBM, the solvent environment is modelled as a linearly responding heat bath.

We modify the SBM Hamiltonian slightly by introducing a shift to the solvent coordinate, such that the donor state corresponds to the global ground state of the electron+solvent system in the absence of electronic coupling ($\Delta = 0$):

$$H = (\lambda_R - \epsilon) \left(\frac{\hat{\mathbf{1}} + \sigma_z}{2} \right) - \frac{\Delta}{2} \sigma_x + \left(\frac{\hat{\mathbf{1}} + \sigma_z}{2} \right) \otimes \sum_k g_k (b_k^\dagger + b_k) + \sum_k \omega_k b_k^\dagger b_k. \quad (3.40)$$

As above, the parameter ϵ is the difference in energy between the donor and acceptor states and is often referred to as the *bias*. The potential energy surfaces for this model

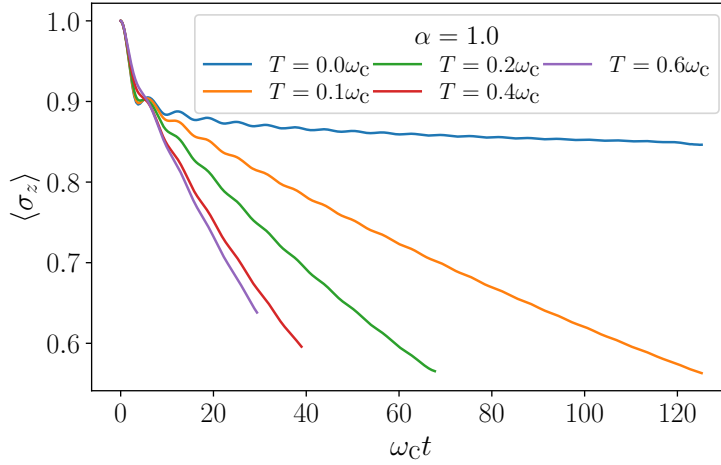


Figure 3.9: Dynamics of $\langle \sigma_z \rangle$ at critical coupling $\alpha = 1$ with an initial condition $|\uparrow_z\rangle$ at a range of temperatures. The localisation transition is destroyed by finite temperatures.

are identical to those in Fig. 3.2 and Fig. 3.3 but with a shifted q -axis: $q \mapsto q + \frac{1}{2}q_0$.

In the absence of solvent tunnelling, the electron transfer reaction is well described by Marcus' theory when a separation of time scales exists between the electron and solvent environment. This separation of time scales occurs in two distinct limits known as adiabatic and non-adiabatic (See Fig. 3.10). In the adiabatic limit the solvent degrees of freedom are assumed to be slow compared to the electronic system ($\omega_c \ll \Delta$) and the Born-Oppenheimer approximation for the electron can be used. If the reorganisation energy is greater than twice the electronic coupling ($\lambda_R > 2\Delta$) (cf. Eq. (3.27)), the lower electronic Born-Oppenheimer surface has two minima, separated by a barrier, which are degenerate in the case of zero bias (cf. Fig. 3.3 and Fig. 3.10(a)). The ET reaction then consists of the motion of the solvent across this lower electronic surface. The reaction rate in this limit is given by

$$k \propto \exp(-E_b\beta), \quad (3.41)$$

where E_b is the height of the energy barrier.

In the opposite, non-adiabatic limit (cf. Fig. 3.10(b)), the electronic coupling is assumed to be small and the solvent fluctuations to be fast ($\Delta \ll \omega_c$). In this limit, the reaction can be understood in terms of transitions between adiabatic potential energy surfaces, known as Marcus parabola. The Marcus parabola are simply the potential energy surfaces of the donor and acceptor states. The assumption that the bath is fast allows the electronic transitions to be treated via the Frank-Condon principle, which states that transitions between donor and acceptor states happen vertically, with no change in the solvent polarisation. The transition rate in this regime can be calculated with the Golden Rule. In order for these transitions to be energetically favourable, however, the donor and acceptor states must be brought close in energy through a

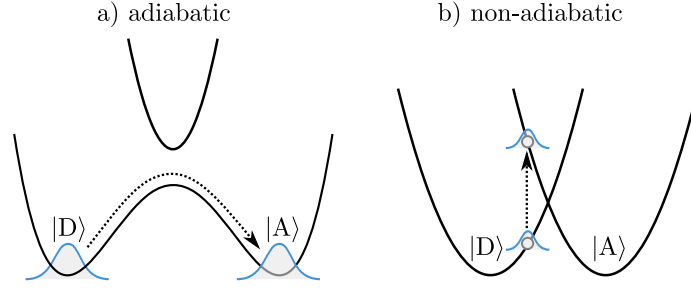


Figure 3.10: The two limits of electron transfer. In the adiabatic limit (a) the coupling between donor and acceptor states is large and the reaction can be assumed to take place on the lower potential energy surface with *no transitions*. In the opposite, non-adiabatic limit (b) the coupling is small and the electron transfer may be described in terms of *transitions* between the donor and acceptor states. These transitions are often treated perturbatively via the Golden Rule; the Frank-Condon principle states that transition happen *vertically*.

reorganisation of the solvent modes. The fact that Frank-Condon transitions only occur in the vicinity of the intersection of the Marcus parabola leads to the prediction of a non-monotonic dependence of the rate on the bias ϵ .

However, at low temperatures, when there is not sufficient thermal energy available to support electronic tunnelling, solvent tunnelling is expected to be the dominant reaction mechanism. In the non-adiabatic limit, rate expressions can be derived using a Golden Rule approach that is second-order perturbative in the electronic coupling Δ but which treats the electron-solvent coupling to all orders. For an Ohmic spectral density this approach yields the following expression for the ET reaction rate in the zero bias limit [16]

$$k = \frac{\beta\Delta^2}{4} \sqrt{\frac{\pi}{2\alpha\psi^{(1)}(\frac{1}{2} + \frac{1}{\omega_c\beta})}} \left(\frac{\Gamma^2(\frac{1}{2} + \frac{1}{\omega_c\beta})}{\beta\omega_c\Gamma^2(1 + \frac{1}{\omega_c\beta})} \right)^{2\alpha}, \quad (3.42)$$

where Γ and $\psi^{(1)}$ denote the gamma function and first order polygamma function respectively. The above rate expression predicts a non-monotonic relationship between the rate and the temperature with a quantum to classical transition in the region $\omega_c\beta \sim 1$. In the low temperature, quantum region ($\omega_c\beta \gg 1$) the rate grows as a power law of the temperature ($k \propto T^{2\alpha-1}$), whereas in the high temperature, classical region ($\omega_c\beta \ll 1$) we have power law decay ($k \propto \frac{1}{\sqrt{T}}$).

The above expression is only valid in the incoherent tunnelling regime, where $\alpha > 0.5$; as seen in the previous section, the Ohmic SBM exhibits coherent tunnelling for $0 < \alpha \leq 0.5$ and so the dynamics is not characterised by a single rate in this regime.

In Fig. 3.11 we present tunnelling dynamics in the incoherent, non-adiabatic regime for a range of temperatures. Figure 3.11(a) gives the expectation value of σ_z which is a measure of the progress of the reaction from the donor state ($\sigma_z = -1$) to the acceptor state ($\sigma_z = 1$). In Fig. 3.11(b), we show the expectation of σ_y , which, as

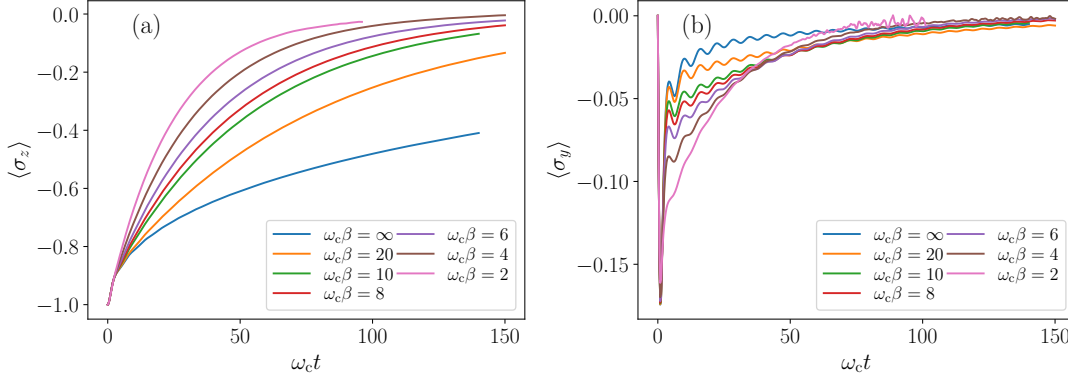


Figure 3.11: Tunnelling dynamics in the incoherent, non-adiabatic regime, with $\alpha = 0.8$ and $\Delta = 0.3\omega_c$. The reaction coordinate is represented by $\langle\sigma_x\rangle$ (panel a), while $\langle\sigma_y\rangle$ (panel b) represents the tunnelling momentum.

discussed in the previous section can be interpreted as a kind of momentum associated with the tunnelling. We find that there is a sharp initial spike in $\langle\sigma_y\rangle$ which decays with oscillations which are increasingly damped at higher temperatures. As we might have predicted, these transient dynamics occur on a timescale of $\tau \approx \omega_c^{-1}$, which is the fastest response time of an environment with an upper cut-off frequency of ω_c . This is approximately the timescale over which the environment will adjust to the sudden presence of the electron, and essentially sets the timescale for the formation of the adiabatic landscape (or, alternatively, for the formation of the dressed polaron states), after which the tunneling dynamics proceed.

By fitting each $\langle\sigma_z(t)\rangle$ to an exponential decay $-e^{-kt}$ on time scales $t > \tau$, we obtain approximate rates that may be compared with the perturbative formula Eq. (3.42). The extracted rates, which were also calculated for three different Δ s, are plotted against the inverse temperature, along with the analytic result, in Fig. 3.12. The agreement is best when one is deep in either the quantum or the classical regime, while the rate in the transition region is underestimated by the perturbative theory. One may also observe a growing deviation (most remarkably in the transition region) between the numerically calculated rate and the analytical result as the electronic coupling Δ is increased and one moves towards the adiabatic regime. We interpret the departure from the Golden Rule formula in the transition region as being due to thermally activated tunnelling on the lower adiabatic surface whereby $k \propto \exp(-E_b\beta)$. The inset of Fig. 3.12 plots the reaction rate for $\Delta = 0.4\omega_c$ in the transition region on a log scale; the rate increases exponentially with temperature in accordance with thermally activated tunnelling. At very high temperatures, one is no longer really in the adiabatic limit as the upper potential energy surface will begin to become populated, hence the departure from thermally activated tunnelling in this region.

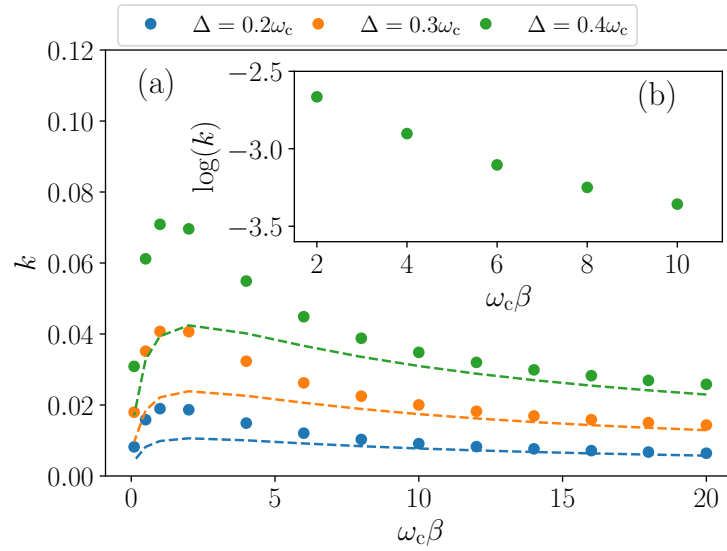


Figure 3.12: (a) ET reaction rates for the Ohmic SBM with $\alpha = 0.8$ and three different electronic coupling strengths Δ . Dots represent rates extracted from T-TEDOPA simulations, while dotted lines represent the analytical rate expression of Eq. (3.42), which is perturbative in Δ . A quantum to classical transition can be observed around $\omega_c \beta \sim 1$. The inset (b) shows the reaction rate for $\Delta = 0.4\omega_c$ on a log scale; the exponential trend in this region suggests thermally activated tunnelling whereby $k \propto \exp(-E_b \beta)$.

Data Availability

A repository containing the data presented in this section is available online (See Ref. [106]). The results of Fig. 3.11 and 3.12 are also published in Dunnett and Chin [107].

3.4 Two-bath Spin-Boson Model

Having studied, in the previous two sections, the dynamics of a TLS coupled to a single bosonic bath, we now move beyond this simple model to simulate the non-equilibrium dynamics of a TLS connected to *two* baths at different temperatures. The temperature gradient thus set-up will induce heat flow through the TLS and lead to the establishment of a non-equilibrium steady state. This model, known as the two-bath SBM, has both wide-ranging practical applications, such as studying heat and charge transfer in nano-devices and molecules [108, 109, 110], as well as being of fundamental relevance for quantum thermodynamics, decoherence, and non-equilibrium steady states [99, 111, 112, 113, 114]. Some of the results presented in this section have also been published in Dunnett and Chin [102].

We set up the Hamiltonian as follows

$$\hat{H} = \underbrace{-\frac{\Delta}{2}\sigma_x}_{\hat{H}_S} + \underbrace{\frac{\sigma_z}{2}}_{A_S} \otimes \sum_{\alpha,k} g_{\alpha,k}(b_{\alpha,k}^\dagger + b_{\alpha,k}) + \sum_{\alpha,k} \omega_{\alpha,k} b_{\alpha,k}^\dagger b_{\alpha,k}. \quad (3.43)$$

We label the baths with the symbols ‘h’ for ‘hot’ and ‘c’ for ‘cold’, thus $\alpha \in [h, c]$. Since we are particularly interested in the effects of a temperature gradient, we specialise to the case where the spectral densities of the two baths are identical: $J_h(\omega) = J_c(\omega)$, and the only their temperatures T_h and T_c differ. As usual, we use the Ohmic spectral density defined in Eq. (3.26). For the results presented here we take the coupling strength to be $\alpha = 0.1$.

As there are only two baths, this OQS problem may be solved with an ordinary chain-MPS with the system lying somewhere near the middle and two bosonic chains extending on either side, as shown in Fig. 3.13.

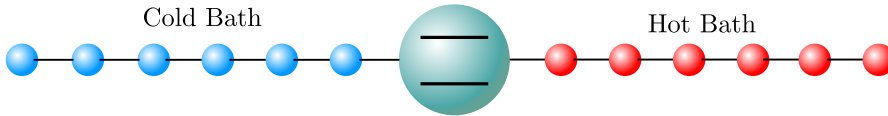


Figure 3.13: The structure of the MPS used to simulate the two-bath SBM.

The TLS is prepared in its ground state ($|\downarrow_x\rangle$) and connected at $t = 0$ to the two baths. Figure 3.14(a) shows the real-time evolution of $\langle\sigma_x\rangle$ for fixed cold bath temperature $\omega_c\beta = 100$ and varying hot bath temperature. We choose the TLS gap to be $\Delta = 0.2\omega_c$. In Fig. 3.14(b) the steady-state spin polarization is plotted as a function of the temperature difference between the two baths. To understand the basic features of

the steady state, let us consider a perturbative set of rate equations for the population of the spin-up level P_\uparrow . Assuming that the rates of absorption and emission from each bath of TLS obey detailed balance, the dynamics of P_\uparrow can be obtained from the equation

$$\frac{dP_\uparrow(t)}{dt} = -\Gamma P_\uparrow(t)(n_c + n_h + 2) + \Gamma(1 - P_\uparrow(t))(n_c + n_h), \quad (3.44)$$

where Γ is the rate of emission and absorption and the n_α are the mode populations given by

$$n_\alpha = \frac{1}{e^{\Delta\beta_\alpha} - 1}. \quad (3.45)$$

From this equation it is straightforward to extract the steady state population $P_\uparrow(t \rightarrow \infty)$ and thus the steady state polarisations ($\langle \sigma_x \rangle = 2P_\uparrow - 1$):

$$\langle \sigma_x(t \rightarrow \infty) \rangle = -\frac{1}{n_c + n_h + 1}. \quad (3.46)$$

Once again, one must account for renormalisation effects by replacing Δ with the renormalised gap Δ_r and suppressing the expectation value by a factor Δ_r/Δ . Indeed, for the lowest temperatures, the spin dynamics are almost entirely due to renormalization effects, as thermal occupation of the excited level is negligible. As shown in Fig. 3.14(b), the agreement between the numerical and analytical results is very good. Note that since we are far from critical coupling α_c we do not need to re-scale the coupling strength as in Sec. 3.2.1.

3.4.1 Heat flow

We now wish to define operators that will enable us to measure the heat flowing in and out of the TLS. The energy of the TLS satisfies the continuity equation

$$\frac{d\hat{H}_S}{dt} = \hat{J}_h - \hat{J}_c, \quad (3.47)$$

where we have defined \hat{J}_h as the heat flux *into* the TLS *from* the hot bath, and \hat{J}_c as the heat flux *out of* the TLS *into* the cold bath. The left-hand side of Eq. (3.47) may be evaluated by means of the Heisenberg equation of motion

$$\frac{d\hat{H}_S}{dt} = i[\hat{H}, \hat{H}_S]. \quad (3.48)$$

Evaluating the commutator in the chain picture yields:

$$[\hat{H}^{\text{chain}}, \hat{H}_S] = [\kappa_h \frac{\sigma_z}{2}(c_{h,0} + c_{h,0}^\dagger), -\frac{\Delta}{2}\sigma_x] + [\kappa_c \frac{\sigma_z}{2}(c_{c,0} + c_{c,0}^\dagger), -\frac{\Delta}{2}\sigma_x] \quad (3.49)$$

$$= -i\frac{\kappa_h\Delta}{2}\sigma_y(c_{h,0} + c_{h,0}^\dagger) - i\frac{\kappa_c\Delta}{2}\sigma_y(c_{c,0} + c_{c,0}^\dagger), \quad (3.50)$$

from which the two heat flux operators may be identified as

$$\hat{J}_h = +\frac{\kappa_h \Delta}{2} \sigma_y (c_{h,0} + c_{h,0}^\dagger) \quad (3.51)$$

$$\hat{J}_c = -\frac{\kappa_c \Delta}{2} \sigma_y (c_{c,0} + c_{c,0}^\dagger). \quad (3.52)$$

The operators $c_{\alpha,0}^{(\dagger)}$ refer to the creation and annihilation operators of the first site of chain α , i.e. the site coupled to the TLS. Measuring these heat flow operators requires access to the observables of the bath. A virtually unique advantage of the T-TEDOPA method is that such access is provided naturally as we simulate an MPS for the full system+environment state.

Representative heat flows are shown in Fig. 3.15(a) for large and zero differences in the bath temperatures. In both cases, the initial dynamics involve heating from both hot and cold environments, as the spin is initially in a pure ($T = 0\text{K}$) ground state. As the dynamical steady state of the spin is obtained, a net heat current appears from the hot to cold environment. This heat current vanishes as the temperature difference of the baths is reduced, as we would expect. From the long-time solution of the Pauli master equation given in Eq. (3.44), the steady-state heat flux from the hot to cold environment can be shown to be

$$J_{\text{ss}} = \langle \hat{J}_h(t \rightarrow \infty) \rangle = \langle \hat{J}_c(t \rightarrow \infty) \rangle = \Gamma \frac{n_h - n_c}{1 + n_h + n_c}, \quad (3.53)$$

and this is plotted alongside our numerical data in Fig. 3.15(b). The simulations correctly capture the essentially non-linear behaviour of heat flow through the quantum heat leak TLS, although a linear regime where Fourier's law of heat flow appears to hold can be clearly observed before the flows saturate for large temperature differences.

3.5 Chain Dynamics

As mentioned in the previous section, one of the key advantages of the T-TEDOPA method is that one has direct access to the observables of the bath. Direct measurements can be made on the MPS to obtain expectation values of chain-basis observables, following which, the chain mapping can be reversed to obtain information on the modes of the original OQS Hamiltonian. Furthermore, one can also reverse the Tamascelli temperature mapping to obtain thermal expectation values of bath observables.

In this section we exploit this property to explore the bath dynamics in the simple case of the one-bath SBM. This will lead to insights into the workings of the T-TEDOPA method and also reveal some potential limitations, particularly regarding its ability to simulate long-time dynamics.

The operators that one can directly measure during a simulation are those which act on the chain sites, namely $c_{\alpha,n}^{(\dagger)}$ as defined in Eq. (2.86). If instead we wished to calculate, for example, the occupation of the bosonic modes in the original star picture, we would

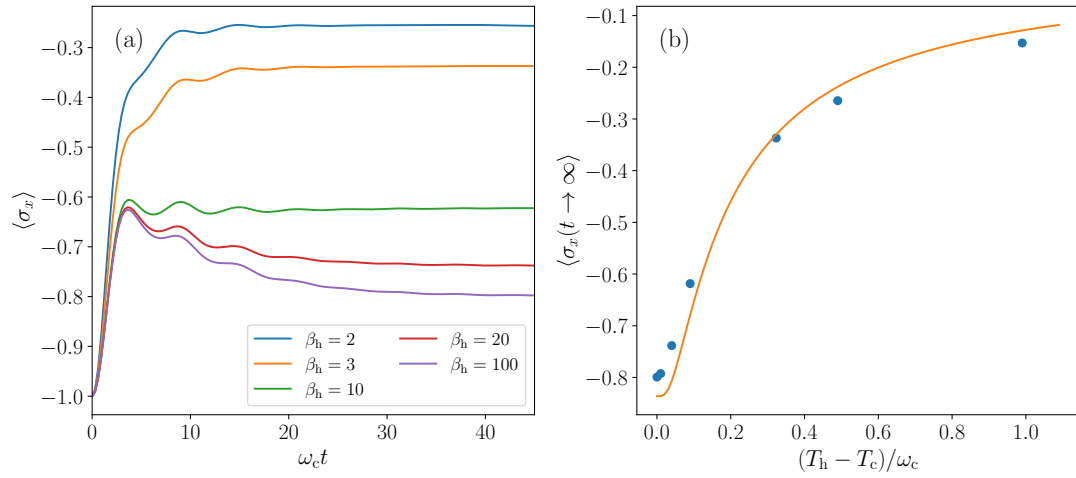


Figure 3.14: (a) Population dynamics of heat-leak TLS which connects a cold bath with inverse temperature $\beta_c = 100$ with a hot bath with inverse temperature β_h . The TLS has a gap $\Delta = 0.2\omega_c$ and both baths have Ohmic spectral densities with non-perturbative coupling strength $\alpha = 0.1$. (b) Steady state TLS polarisation vs temperature gradient; blue dots represent the steady states extracted from numerical simulations, while the orange line plots the analytical prediction of Eq. (3.46) where the renormalisation effects have been taken into account.

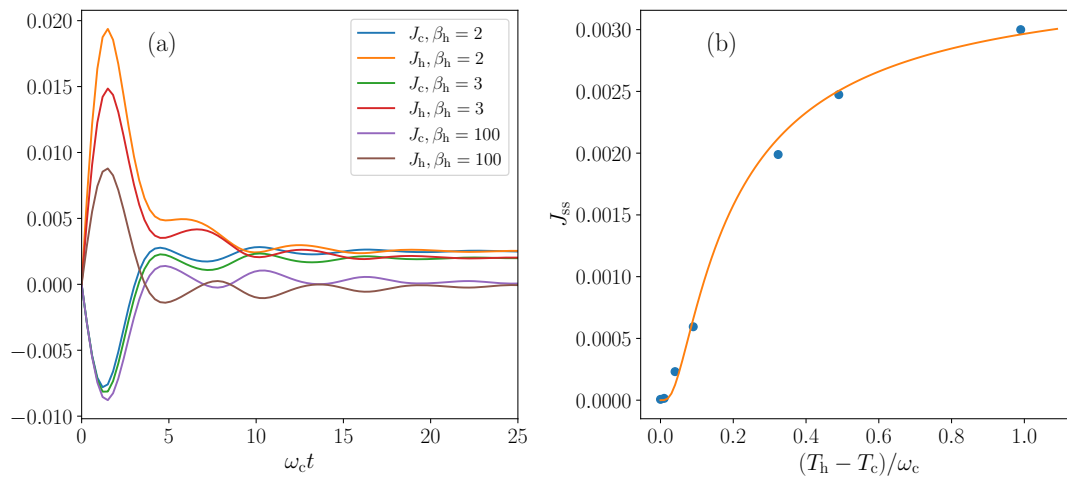


Figure 3.15: (a) Heat flows in (J_h) and out (J_c) of the heat-leak TLS for fixed cold bath inverse temperature $\beta_c = 100$ and varying hot bath temperature. At early times, heat flows in from both baths to the initially 0K TLS; later on, non-equilibrium heat currents are established for finite temperature gradients. (b) Steady state heat current as a function of temperature gradient. The blue dots represent numerical results, while the orange line plots the analytical result of Eq. (3.53) with renormalisation taken into account.

require to reverse Eq. (2.86) in order to obtain the original bosonic modes in terms of the chain modes

$$b_{\omega}^{(\dagger)} = \sum_{n=0}^{\infty} U_n(\omega) c_n^{(\dagger)}. \quad (3.54)$$

The mode occupation is thus given by

$$\langle \hat{n}_{\omega}^b \rangle := \langle b_{\omega}^{\dagger} b_{\omega} \rangle = \sum_{n,m=0}^{\mathcal{N}_m-1} U_n(\omega) U_m(\omega) \langle c_n^{\dagger} c_m \rangle, \quad (3.55)$$

where we have truncated the summation in accordance with the chain truncation (cf. Sec. 2.4.1). Evaluating Eq. (3.55) thus requires the calculation of \mathcal{N}_m^2 expectation values, which may be performed surprisingly fast on an MPS. While one may evaluate Eq. (3.55) at any ω , due to the truncation of the chain, only a discrete set of modes $k \in [0, \mathcal{N}_m - 1]$ is actually present in the simulation. Equation (3.55) thus provides an interpolation of the simulated mode frequencies, which should be accurate, provided the error introduced by the chain truncation is small. Here however, we will only calculate expectation values for the discrete modes, which are given by

$$\langle \hat{n}_k^b \rangle := \langle b_k^{\dagger} b_k \rangle = \sum_{n,m=0}^{\mathcal{N}_m-1} U_{n,k} U_{m,k} \langle c_n^{\dagger} c_m \rangle, \quad (3.56)$$

where $U_{n,k}$ is simply the $\mathcal{N}_m \times \mathcal{N}_m$ unitary matrix that diagonalises the chain Hamiltonian.

In Sec. 2.4.2 we introduced the Tamascelli temperature mapping by demonstrating that, given an OQS linearly coupled to a thermal bath, performing the transformation $J(\omega) \mapsto J_{\beta}(\omega)$ and replacing the mixed environment state with the vacuum, leaves the OQS dynamics unchanged. This observation is extremely useful since this pure state system is far more amenable to simulation. Thus, the modes $b_k^{(\dagger)}$ of the chain that is simulated are the modes of this *extended*, vacuum, environment, with spectral density $J_{\beta}(\omega)$, rather than the original *thermal* environment with spectral density $J(\omega)$. However, an alternative formulation is possible whereby the modes of the extended environment are obtained via Bogoluibov transformations on entangled squeezed state pairs. These entangled squeezed pairs represent the original bosonic environment in its thermal state; they each consist of a mode, coupled to the system, and an, uncoupled, ancillary mode. Due to the properties of the squeezed state, tracing out the ancillary mode leads to the thermal density matrix. Then, by reversing the Bogoluibov transformation on the simulated modes, we are able to return to the original, thermal, picture and thus obtain expectation values for the original, thermally occupied bath modes.

For example, denoting the number operator of the original thermal modes $\hat{n}_{\omega}^{\text{th}}$, we have

$$\langle \hat{n}_{\omega}^{\text{th}} \rangle_{\beta} = e^{-\omega\beta} + \langle \hat{n}_{\omega}^b \rangle - \langle \hat{n}_{-\omega}^b \rangle. \quad (3.57)$$

Clearly, in the zero temperature limit ($\beta = \infty$), where $\langle \hat{n}_{-\omega}^b \rangle = 0$, the temperature mapping has no effect on the modes and thus Eq. (3.57) reduces to

$$\langle \hat{n}_{\omega}^{\text{th}} \rangle_{\beta=\infty} = \langle \hat{n}_{\omega}^b \rangle. \quad (3.58)$$

In Fig. 3.16(a), we plot the bath mode occupations $\langle \hat{n}_k^b \rangle$ for several temperatures. The SBM parameters are $\alpha = 0.1$ and $\Delta = 0.2\omega_c$. Each observation was taken after the spin, which was initially prepared in the state $|\uparrow_x\rangle$, had decayed into its thermal steady state and thus provides a kind of absorption spectrum for the system. We emphasise that these data refer to the modes of the *extended* environment rather than the original bosonic bath and thus the mode energies run from $-\omega_c$ to ω_c .

We find that for zero temperature ($\beta = \infty$) the bath absorption spectrum contains a single peak at a frequency around $\omega_p = 0.17\omega_c$, suggesting that the spin emits into the bath at a re-normalized frequency that is lower than the bare gap of the TLS ($\Delta = 0.2\omega_c$). This agrees well with the non-perturbative polaron theory of Sibley and Harris [96] which predicts a renormalised gap $\Delta_r = 0.167\omega_c$ (See Eq. (3.31)).

Moving to non-zero temperature we see that a peak begins to form at a corresponding negative frequency ω_n , which we interpret as being due to the spin absorbing thermal energy from the bath by the emission (creation) of negative energy quanta. We can expect therefore that the rate of growth of the negative peak will be related to the rate at which the TLS absorbs quanta from the thermal bath; we denote this rate Γ_\uparrow . Similarly, the positive peak should grow at a rate related to Γ_\downarrow : the rate at which the TLS emits into the thermal bath. As a result, the positive and negative peak heights for the snapshot of Fig. 3.16(a) should also be related, respectively, to Γ_\uparrow and Γ_\downarrow .

In accordance with detailed balance, the ratio between the positive and negative frequency peaks approaches unity as temperature is increased and by $\omega_c\beta = 2$ the two peaks have merged to form a single, almost symmetric, distribution, reflecting the dominance of thermal absorption and emission over spontaneous emission at high temperature ($\Gamma_\uparrow = \Gamma_\downarrow$). Indeed, according to detailed balance we should have

$$\frac{\Gamma_\uparrow}{\Gamma_\downarrow} = e^{\beta\Delta_r}. \quad (3.59)$$

As shown in Fig. 3.16(b) the ratio of the peak heights obeys

$$\frac{\langle \hat{n}_{\omega_p}^b \rangle}{\langle \hat{n}_{\omega_n}^b \rangle} \propto e^{\beta\epsilon}, \quad (3.60)$$

with $\epsilon = 0.118$, which is approximately $\sqrt{2}\Delta_r$, suggesting that $\langle \hat{n}_{\omega_p}^b \rangle \propto \Gamma_\uparrow^{\sqrt{2}}$ and $\langle \hat{n}_{\omega_n}^b \rangle \propto \Gamma_\downarrow^{\sqrt{2}}$. This detailed balance relation in the peak heights stems from the ratio of the coupling strengths to the positive and negative modes encoded in the thermal spectral density

$$\frac{J_\beta(\omega)}{J_\beta(-\omega)} = e^{\beta\omega}. \quad (3.61)$$

From the above, it is clear how we are able to substitute a thermally occupied bath by an extended, unoccupied one: the extension to negative frequencies essentially allows the process whereby the system would be heated by the environment (absorbing pre-existing quanta in the thermal bath) to be mimicked by spontaneous emission into a negative energy vacuum of states.

3.5.1 Performance for long-time dynamics

On the face of it, under the T-TEDOPA method, the simulation of an OQS at finite temperature seems to have roughly the same computational cost as at zero temperature; in both cases we propagate an MPS representing our system coupled to one or more tight-binding chains, which are initially in trivial vacuum states. We may expect a finite temperature bath to require slightly more computational resources due to the fact that the hopping strengths (t_n) increase with temperature (cf. Fig. 2.5(a)). Increased hopping strengths lead to faster propagation of excitations on the chain (cf. Fig. 2.3) and thus we find that, for a given simulation time, more chain sites will be required to avoid errors due to the truncation of the chain. Nonetheless, this effect only leads to a modest increase in computational cost. This conclusion is somewhat surprising since there seems to be an inherent difficulty to the finite temperature problem. We may wonder therefore, whether there is not some hidden price to pay in going to finite temperature.

Figure 3.16(c) gives an indication of what this hidden cost may be. In the figure we plot the total number of excitations in the bath, given by

$$\langle \hat{N}_T^b \rangle := \sum_k \langle b_k^\dagger b_k \rangle, \quad (3.62)$$

as a function of time. It is easy to show that the total excitation number in the chain basis is identical to that in the original mode basis:

$$\langle \hat{N}_T^c \rangle := \sum_k \langle c_k^\dagger c_k \rangle = \langle \hat{N}_T^b \rangle, \quad (3.63)$$

allowing us to define the total excitation number independently of the mode basis

$$\langle \hat{N}_T \rangle := \langle \hat{N}_T^b \rangle = \langle \hat{N}_T^c \rangle. \quad (3.64)$$

We find that, at zero temperature, the total mode occupation initially grows according to what appears to be a power law, and then saturates. The saturation value may be understood as being the total number of excitations created in the bath by the TLS during its decay. At finite temperatures however, the total mode occupation shows unbounded, linear growth, whose rate increases with the temperature. This is despite the fact that, for the finite temperature baths, we should also expect to reach a steady state in the bath once thermal equilibrium has been established.

Explaining oscillator population growth

We believe this observation can be explained as follows. The thermal occupation of the physical bath mode with frequency ω is obtained, according to Eq. (3.57), by subtracting its negative, from its positive energy counterpart in the extended mode basis. While $\langle \hat{n}_\omega^{\text{th}} \rangle_\beta$ will reach a steady state, the components $\langle \hat{n}_\omega^b \rangle$ and $\langle \hat{n}_{-\omega}^b \rangle$ will be forever increasing, reflecting the fact that the TLS reaches a *dynamic* equilibrium with the bath, in which energy is continuously being absorbed from and emitted into the bath at equal

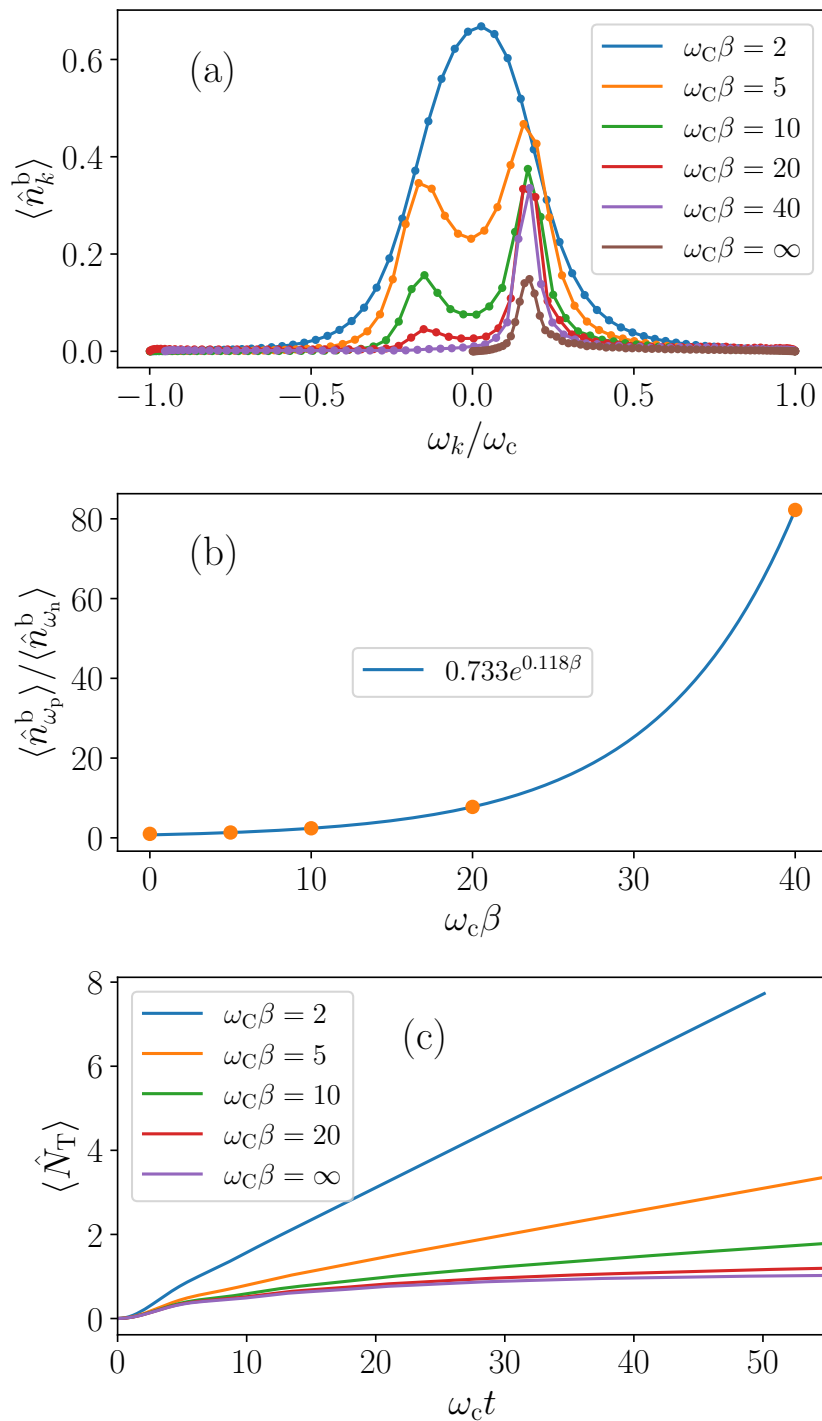


Figure 3.16: (a) Mode occupations of the extended environment following the decay of a TLS from the initial state $|\uparrow_x\rangle$. The model is the Ohmic SBM with parameters $\alpha = 0.1$ and $\Delta = 0.2\omega_c$. (b) Peak height ratios (orange dots) for the snap shots shown in panel a and exponential fit (blue line). (c) Total mode occupation as a function of time. These data have also been published in Dunnett and Chin [107].

rates, thus filling up the positive and negative reservoirs. Indeed, as is illustrated in Fig. 3.17, the interaction of a TLS with positive and negative energy reservoirs sets up a cycle in which the system is continuously being excited and de-excited, creating a continuous stream of excitations in both baths.

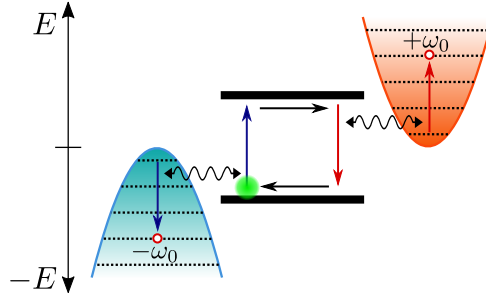


Figure 3.17: The presence of negative energy modes in the environment means that pairs of positive and negative energy excitations are continually being generated, leading to the growth of entanglement and the filling-up of the chain oscillator states.

While the above explanation seems plausible, one may observe from Fig. 3.16(a) that, in addition to the two peaks at ω_n and ω_p , there is also a growing population centred at $\omega = 0$, which, in the high-temperature limit, comes to dominate. One might argue therefore that the reason the mode occupations show unbounded growth at high- T is as a result of this central peak instead of the two side peaks. In fact, the presence of this central peak is incidental and is dependent on the behaviour of the spectral density as ω approaches zero. It is well known for example that, for sub-Ohmic baths, oscillator populations diverge in ground state DMRG calculations, necessitating the use of special methods [111]. In that case, the problem can be remedied by a simple transformation to a displaced oscillator basis.

Rather confusingly however, in the case of an Ohmic bath at high- T , the zero frequency population growth that results from the low frequency behaviour of the temperature mapped spectral density $J_\beta(\omega)$, leads to a linear growth of the total mode occupation - exactly what is observed in Fig. 3.16(c). If the population growth is really just a result of the low frequency behaviour, then we may expect that the same methods used in the case of the sub-Ohmic bath may be applied here, and that long-time dynamics will be accessible without exploding computational cost. If however the heating cycle of Fig. 3.17 plays a role, it is unlikely that a simple basis transformation will help. It is therefore important to be able to clearly distinguish these two effects.

Let us consider the simple case in which a bosonic bath, consisting of modes $a_k^{(\dagger)}$, with power law spectral density

$$J(\omega) = 2\alpha\omega \left(\frac{\omega}{\omega_c}\right)^{s-1} \theta(\omega - \omega_c), \quad (3.65)$$

is subject to a constant displacing force which is turned on at time $t = 0$. This could be the case, for example, in the IBM defined by Eq. (3.9), with the spin placed in the state

$|\uparrow_z\rangle$. Under this force, the oscillators, initially in their vacuum states $|0\rangle_k$, will become displaced and be described by the coherent states

$$|\alpha_k(t)/2\rangle = \hat{D}(\alpha_k(t)/2) |0\rangle, \quad (3.66)$$

where $\alpha_k(t)$ is given by Eq. (3.7), which we here repeat:

$$\alpha_k(t) = \frac{g_k(1 - e^{i\omega_k t})}{\omega_k}. \quad (3.67)$$

Recalling the fundamental property of the coherent states, namely that they are eigenstates of the annihilation operator:

$$a|\alpha\rangle = \alpha|\alpha\rangle, \quad (3.68)$$

we easily obtain the time-dependent expectation of the number operator

$$\langle \hat{n}_k(t) \rangle = |\alpha_k(t)/4|^2 = \frac{g_k^2}{2\omega_k^2} (1 - \cos(\omega_k t)). \quad (3.69)$$

We see therefore that, under a constant displacing force, the mode occupations undergo oscillations at the corresponding mode frequencies. However, as ω_k becomes very small, the period of the oscillations will increase, and in the limit $\omega_k \rightarrow 0$ the period will actually be infinite, reducing Eq. (3.69) to a monotonic function of time:

$$\langle \hat{n}_k(t) \rangle \approx g_k^2 t^2 / 2, \quad \omega_k t \ll 1. \quad (3.70)$$

Whether or not this translates to a real divergence of the populations of the relaxed system depends on how g_k behaves as $\omega_k \rightarrow 0$ and hence on the Ohmicity s of the bath. The total mode population is given by the integral

$$\langle \hat{N}_T(t) \rangle = \int_0^{\omega_c} d\omega \frac{J(\omega)}{2\omega^2} (1 - \cos(\omega t)). \quad (3.71)$$

The behaviour of this integral in the long-time limit, where by long-time we mean long with respect to the characteristic frequency of the bath ($\omega_c t \gg 1$), is given in the first column of Tab. 3.1 for sub-Ohmic, Ohmic and super-Ohmic baths. One sees that for an Ohmic bath, the total occupation only grows logarithmically which is more or less consistent with the zero temperature curve in Fig. 3.16(c).

In the T-TEDOPA simulations, however, the spectral density is not $J(\omega)$ but $J(\omega, \beta)$ given by

$$J(\omega, \beta) = \text{sign}(\omega) \frac{J(|\omega|)}{2} \left(1 + \coth\left(\frac{\omega\beta}{2}\right) \right). \quad (3.72)$$

In the limit of high temperature we have

$$1 + \coth\left(\frac{\omega\beta}{2}\right) \approx \frac{2}{\omega\beta}, \quad \omega\beta \ll 1, \quad (3.73)$$

	$T = 0 (\beta = \infty)$	$T = \infty (\beta = 0)$
$s = \frac{1}{2}$	$\langle \hat{N}_T \rangle \sim \omega_c t^{1/2}$	$\langle \hat{N}_T \rangle \sim \omega_c t^{3/2}$
$s = 1$	$\langle \hat{N}_T \rangle \sim \log(\omega_c t)$	$\langle \hat{N}_T \rangle \sim \omega_c t$
$s = 2$	$\langle \hat{N}_T \rangle \sim \omega_c t^{-1}$	$\langle \hat{N}_T \rangle \sim \log(\omega_c t)$

Table 3.1: Summarising the long-time ($\omega_c t \gg 1$) behaviour of the total occupation of a bath of bosonic modes with temperature mapped spectral density $J(\omega, \beta)$ under a constant displacement field.

which gives rise to the following expression for the total mode population as a function of time in a T-TEDOPA simulation:

$$\langle \hat{N}_T(t) \rangle = \int_{-\omega_c}^{\omega_c} d\omega \text{sign}(\omega) \frac{J(|\omega|)}{2\omega^3\beta} (1 - \cos(\omega t)), \quad \omega_c\beta \ll 1. \quad (3.74)$$

The second column of Tab. 3.1 gives the long time behaviour of this function for the different Ohmicities. Due to the additional factor of ω in the denominator, the behaviour for an Ohmicity s at zero temperature can be expected to be seen at high temperature for an Ohmicity of $s + 1$. We see that for an Ohmic bath at high temperature we expect $\langle \hat{N}_T \rangle$ to grow linearly.

In order to determine whether the heating cycle effect is really present, we repeat the mode measurements of Fig. 3.16 for a super-Ohmic spectral density with $s = 2$. The high temperature behaviour of $\langle \hat{N}_T \rangle$ for this model, according to Tab. 3.1, should be similar to the *zero* temperature behaviour of the Ohmic model. Hence, if we still observe growing populations, we can conclude that this is due to the heating cycle, and not simply down to diverging displacements. The results presented in Fig. 3.18 confirm this conclusion. In Fig. 3.18(a) we present three snapshots of the mode occupations in the extended bath picture for the super-Ohmic SBM at high temperature ($\omega_c\beta = 2$). In contrast to the Ohmic SBM, the mode occupation at $\omega = 0$ is zero and only the two peaks at ω_n and ω_p are present. These peaks grow with time and this growth continues even after the TLS and the bath have reached equilibrium (cf. Fig. 3.18(c)). In Fig. 3.18(b) we see that this leads to a linear growth of the total mode occupation.

We thus conclude that, at high temperature, the reservoir structure present in the T-TEDOPA method leads to a heating cycle which causes a linear growth in the total mode occupation of the chain, regardless of the details of the original spectral density. In the case of an Ohmic bath, this effect, while still present, was disguised, as the low frequency behaviour of the spectral density also lead to a linear growth in occupation.

A growing number of excitations in the chain will increase the computational cost for two reasons: (1) the number of Fock states d retained for each chain site will need to increase and (2) more excitations will lead to greater entanglement and thus a larger MPS bond dimension will be necessary.

Entanglement growth is a problem that is not limited to OQS and T-TEDOPA but is ubiquitous in exact quantum dynamics and forms the main barrier to obtaining accurate,

long-time dynamics in condensed phase systems. However, entanglement growth is not always a serious issue, particularly if one is only interested in the short-time, transient dynamics as is the case in the present section. In addition, for the particular case of T-TEDOPA, where the rate of entanglement growth is broadly proportional to the temperature, we can expect that the time-scale of the system dynamics will reduce roughly in proportion to the increase in the entanglement growth-rate, and thus we find that high-temperature simulations are not necessarily more expensive than low-temperature ones. Where entanglement growth may cause problems is in the extraction of converged properties of relaxed, i.e. locally thermalised, excited states, such as their (resonance) fluorescence spectra, or multidimensional optical spectra [115]. Recently, the Dissipation-Assisted Matrix-Product Factorisation [116] has been proposed which aims to overcome this issue in the OQS context by mapping the bosonic environment onto a set of Lindblad damped harmonic oscillators. The damping suppresses the growth of entanglement and thus improves performance for long times.

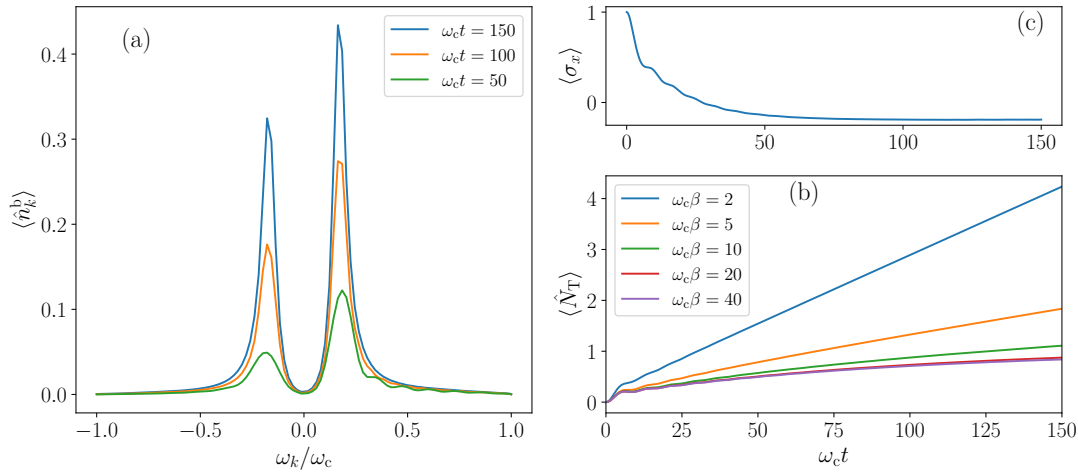


Figure 3.18: (a) Mode occupations of the extended environment at three snapshots. The model is the super-Ohmic SMB with parameters $s = 2$, $\alpha = 0.1$, $\omega_c \beta = 2$ and $\Delta = 0.2\omega_c$, and the spin is initially in the state $|\uparrow_x\rangle$. (b) Total mode occupation as a function of time. The linear growth is due to the continual production of positive and negative energy excitations (cf. Fig. 3.17). (c) The dynamics of $\langle \sigma_x \rangle$, showing the decay of the TLS towards thermal equilibrium. Thermal equilibrium is reached by $\omega_c t = 100$ and yet both mode occupations continue to increase.

Chapter 4

Linear Absorption Spectroscopy

In this chapter we will move beyond the toy models considered in chapter 3 to apply our established methodology to the problem of spectroscopy; specifically, the calculation of linear absorption spectra in the condensed phase.

Spectroscopy is a key step in the screening of materials and molecules for technological applications such as photovoltaics, in the understanding of photochemical reactions, and in the investigation of biological processes. Accurate theoretical modelling of spectra is essential to the interpretation of experimental results, and represents a persistent challenge due to the complexity of the interaction between electronic states and their environment. The exact calculation of experimental spectra in the condensed phase requires a unification of the accurate treatment of non-adiabatic quantum dynamics with the proper inclusion of the effects of the environment. In particular, a fully dynamical approach is required, which incorporates information captured in molecular dynamics simulations of the solute-solvent system.

We take, as a case study, the example of the cationic Methylene Blue (MB) chromophore in aqueous solution, for which previous studies have failed to fully account for the observed spectral features. The resulting investigation will provide a better understanding of the spectral signatures of optical dark states, and also lead us to consider the role of correlations in environment induced fluctuations. This latter will entail an interesting development to the chain-mapping technique.

The application of the T-TEDOPA method to spectroscopy is relatively novel. Nonetheless, in a recent paper, Gelin and Borrelli [117] have shown that it is possible to extend this methodology to the extraction of third-order response functions, opening the door to time and frequency resolved fluorescence spectroscopy.

4.1 Case Study: Methylene Blue

The optical properties of Methylene Blue have been the subject of many studies. Both the molecular structure and excitation landscape have been shown to be environmentally sensitive, and there are many open questions regarding the nature of the solvation and aggregation of this molecule and the influences on the spectral lineshape [118, 119]. Here

we will focus on the monomeric spectrum of Methylene blue in water; the molecule is known to form dimers in aqueous solution causing a dramatic alteration of the spectral lineshape which must be accounted for when comparing to experimentally obtained spectra. The monomeric absorption spectrum has a single peak at wavelength $\lambda = 664\text{nm}$ (1.86eV) with a broad, higher energy shoulder around $\lambda = 610\text{nm}$ (2.03eV) at half the maximum absorption intensity [120]. Despite this simple lineshape, previous approaches at modelling this spectrum appear incomplete - either significantly under or over estimating the shoulder intensity [121, 122].

We expand on previous studies of MB by 1) using an explicitly quantum mechanical treatment of solvent polarisation effects and 2) calculating the response function from an exact numerical treatment of the 3-level linear vibronic coupling (LVC) Hamiltonian which includes the dark S_2 state.

In the sub-sections that follow we will describe the three, ascending levels of theory that we applied to this problem. These are: the Brownian Oscillator Model, the linear vibronic coupling model, and the linear vibronic coupling model with correlated fluctuations. Having described the methodology, we will then move on to present and discuss the resulting spectra and excitation dynamics, and compare with experiment.

This work was the result of a collaboration with Tim Zuehlsdorffⁱ, Christine Isbornⁱⁱ and Duncan Gowlandⁱⁱⁱ. The parameterisations of the models, including all molecular dynamics and electronic structure calculations, were performed entirely by them. This work has been published in Ref. [123].

4.1.1 Brownian Oscillator Model

We begin with the simplest model of optical absorption, the Brownian Oscillator Model (BOM), which treats the ground and excited state potential energy surfaces (PESs) as harmonic surfaces with the same curvature that differ only in a displacement of their respective minima and an offset in their respective ground state energies. The BOM is represented schematically in Fig. 4.1(a). Generalisations of the BOM which relax these assumptions exist. The Generalised Brownian Oscillator Model (GBOM) allows for different curvatures of the ground and excited state PESs and rotations of the oscillator basis, known as Duschinsky rotation; and, the Morse Oscillator model, allows the surfaces to be anharmonic.

We emphasise however, that the BOM *does* include anharmonic effects when solvent modes are treated *dynamically*, as we do here. Indeed, the coordinate q in Fig. 4.1(a) is really just a proxy for the multi-coordinate $\hat{\mathbf{q}}$, describing the displacements of N solvent modes which will all undergo their separate motions. As a result, the true PES that the solute moves on will be anharmonic. This is in contrast to *static* approaches for linear absorption spectra calculations, by which we mean: approaches that require only static input of the ground and excited state optimised energies. These include the Frack-Condon and ensemble methods, whereby excited state PESs are obtained from static

ⁱDepartment of Chemistry, Oregon State University, Corvallis, Oregon 97331, USA

ⁱⁱChemistry and Chemical Biology, University of California Merced, Merced, CA 95343, USA

ⁱⁱⁱDepartment of Physics, Kings College London, London WC2R 2LS, United Kingdom

optimisations on the solute-solvent system. While anharmonic effects are naturally taken into account in the ensemble approach, in the Frank-Condon (FC) method, the PESs are usually required to be harmonic [124]. However, an advantage of the Frank-Condon method is that it can be applied to the GBOM in an approach known as Adiabatic Hessian Frank-Condon (AHFC), and can thus take account of non-linear effects.

We consider a 3-level BOM consisting of a ground state $|S_0\rangle$, a bright excited state $|S_1\rangle$ and a higher excited state $|S_2\rangle$ which is mostly dark. Optical transitions occur between the S_1 and S_0 states, and, to a much lesser extent, between S_0 and S_2 , as indicated in Fig. 4.1(a). We make the common assumption that the light field is fast such that optical transitions happen vertically above the ground state potential minimum. The BOM Hamiltonian is given as follows

$$\hat{H}_{\text{BOM}} = \sum_{\alpha=1}^2 \omega_{0\alpha}^{\text{av}} |S_\alpha\rangle \langle S_\alpha| + \overbrace{\sum_{k,\alpha=1}^2 g_{\alpha,k} |S_\alpha\rangle \langle S_\alpha| (a_{\alpha,k}^\dagger + a_{\alpha,k})}^{\hat{H}_I^{\text{EL}}} + \sum_{k,\alpha=1}^2 \omega_{\alpha,k} a_{\alpha,k}^\dagger a_{\alpha,k}. \quad (4.1)$$

The 3-level electronic system is coupled to two bosonic baths, labelled $\alpha = 1, 2$, which modify respectively the S_0 - S_1 and S_0 - S_2 gaps. By using a model in which the two excited states couple to separate bosonic baths, we are making the assumption that the fluctuations of the excited state energies are completely uncorrelated, and behave as independent sources of Gaussian noise. We will go on to refine this assumption later on.

As usual, the baths are characterised by spectral densities:

$$J_{0\alpha}(\omega) := \sum_k |g_{\alpha,k}|^2 \delta(\omega - \omega_k). \quad (4.2)$$

These bosonic baths model the nuclear environment of the electronic system, which consists, not only of the inter-molecular forces between MB and the surrounding water molecules, but also of the *intra-molecular* vibrations of MB itself (cf. Fig. 4.1(b) and (c)). The solvent is thus able to influence the lineshape both by direct effects on the electronic gap and indirectly via deformations of the molecular structure of MB.

As shown in Fig. 4.1(a), the excitation energies ω_{01}^{av} and ω_{02}^{av} are composed of the sums of the respective reorganisation energies for the baths and the energies of the PES minima:

$$\omega_{0\alpha}^{\text{av}} = \lambda_{0\alpha}^{\text{R}} + \Delta_{0\alpha} \quad (4.3)$$

(See Eq. (3.28) for reorganisation energy definition).

Parameterising the BOM Hamiltonian requires the determination of the two spectral densities and the excitation energies. The spectral densities can be written in terms of the autocorrelation functions of the energy gap fluctuation operators:

$$J_{0\alpha}(\omega) = i\theta(\omega) \int dt e^{i\omega t} \text{Im}\{C_{0\alpha}(t)\}, \quad (4.4)$$

where the autocorrelation functions are given by

$$C_{0\alpha}(t) = \langle \delta U_{0\alpha}(\hat{\mathbf{q}}, t) \delta U_{0\alpha}(\hat{\mathbf{q}}, 0) \rangle, \quad (4.5)$$

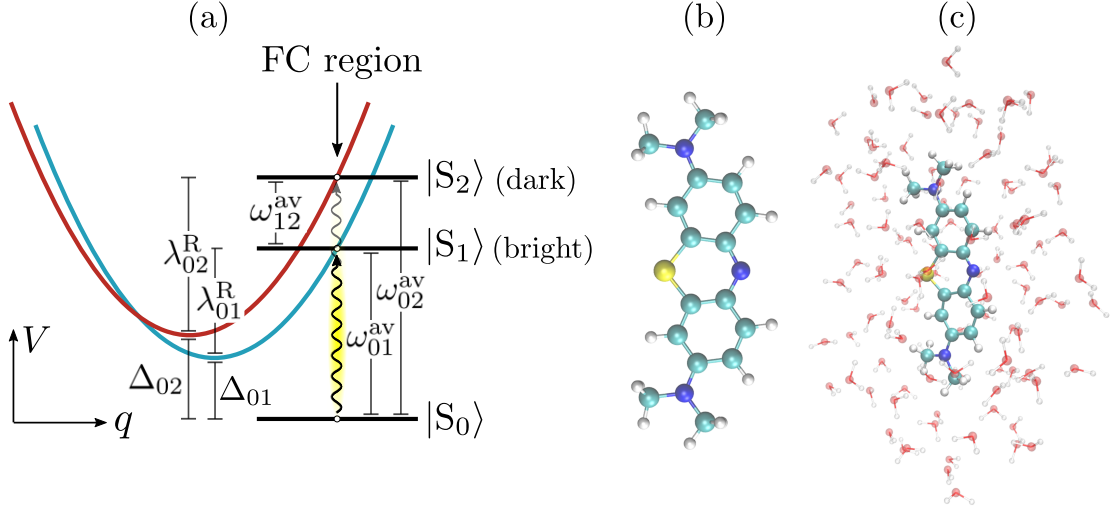


Figure 4.1: (a) Schematic of the Brownian Oscillator Model for Methylene Blue. Optical transitions happen vertically above the ground state minimum, in what is known as the Frank-Condon (FC) region. (b) Structure of Methylene Blue. (c) Methylene Blue in water up to a 6 Å radius. Panels (b) and (c) represent, respectively, the regions which are treated quantum mechanically in the MM and QM TDDFT calculations.

and the energy gap fluctuation operators $\delta U_{0\alpha}(\hat{\mathbf{q}})$ measure the deviation of the energy gaps from their average values ($\delta U_{0\alpha} = U_{0\alpha} - \omega_{0\alpha}^{\text{av}}$). The average values of the energy gaps $\omega_{0\alpha}^{\text{av}}$ provide the excitation energies for the BOM. The operator $\hat{\mathbf{q}}$ is the solvent coordinate and describes the full configuration of the solvent modes.

While it is impossible for all but the simplest systems to calculate the exact quantum autocorrelation function, it is possible to approximately reconstruct $C_{0\alpha}(t)$ from its classical counterpart $C_{0\alpha}^{\text{cl}}(t)$ using quantum correction factors [125, 126, 127]. This allows $C_{0\alpha}(t)$, and thus $J_{0\alpha}(\omega)$, to be obtained from classical correlation functions computed along the ground state of a molecular dynamics (MD) trajectory. If the statistics of the energy gap fluctuation operator are Gaussian, then the mapping of the solute-solvent system to the BOM is exact (cf. Eq. (3.4)).

The BOM Hamiltonian has commuting system and environment parts and thus admits an exact solution of the form Eq. (3.6). The linear absorption spectrum may be calculated from the expression

$$\sigma(\omega) \propto \omega \int_{-\infty}^{\infty} dt e^{i\omega t} \chi(t), \quad (4.6)$$

where $\chi(t)$ is the response function

$$\chi(t) := \langle \hat{V}(t) \hat{V}(0) \rangle, \quad (4.7)$$

and \hat{V} is the optical dipole operator:

$$\hat{V}(\hat{\mathbf{q}}) := V_{01}(\hat{\mathbf{q}}) |S_0\rangle \langle S_1| + V_{02}(\hat{\mathbf{q}}) |S_0\rangle \langle S_2| + \text{h.c.} \quad (4.8)$$

In the above we have written the dipole operator for the general case in which it is a function of the environment configuration $\hat{\mathbf{q}}$. The Condon approximation consists in assuming that the dipole operator is independent of $\hat{\mathbf{q}}$, such that

$$\hat{V} = V_{01} |S_0\rangle \langle S_1| + V_{02} |S_0\rangle \langle S_2| + \text{h.c.} \quad (4.9)$$

This is a reasonable approximation to make when excited states are energetically well separated in the Frank-Condon (FC) region, which is the region in which optical transitions take place (cf. Fig. 4.1(a)).

The optical dipole operator includes the possibility of transitions to the S_2 state, although for MB these are very weak ($V_{01} \gg V_{02}$).

In the BOM, there is no mixing between the S_1 and S_2 states and thus the two contributions to the response function evolve independently, allowing the decomposition

$$\chi(t) = \chi_{01}(t) + \chi_{02}(t), \quad (4.10)$$

where $\chi_{0\alpha}(t) := \langle \hat{V}_{0\alpha}(t) \hat{V}_{0\alpha}(0) \rangle$, and $\hat{V}_{0\alpha} := V_{0\alpha} (|S_0\rangle \langle S_\alpha| + |S_\alpha\rangle \langle S_0|)$. Following Eq. (3.6) and (3.19) we obtain the exact solutions

$$\chi_{0\alpha}(t) = |V_{0\alpha}|^2 e^{i\omega_{0\alpha}^{\text{av}} t} \exp(-g[J_{0\alpha}](t)), \quad (4.11)$$

where $g[J](t)$ is the lineshape function, which, for the BOM is determined entirely by the spectral density:

$$g[J](t) = \int_0^\infty d\omega \frac{J(\omega)}{\omega^2} \left[\coth\left(\frac{\beta\omega}{2}\right) [1 - \cos(\omega t)] - i[\sin(\omega t) - \omega t] \right]. \quad (4.12)$$

One may view this solution in two ways: on the one hand it is the exact solution to the BOM which is, in turn, an exact model for the solute-solvent system *if* the statistics of the energy gap fluctuations are Gaussian. On the hand, if the statistics of the energy gap fluctuations are not Gaussian (which is generally the case), the above solution represents the second-order term in the cumulant expansion of the GBOM, and thus constitutes an approximation in which higher order autocorrelation functions are neglected.

Due to the separable nature of the S_1 and S_2 contributions in the BOM, and the weakness of the S_2 dipole strength, the S_2 state has a negligible effect on the absorption lineshape. However, if a reorganisation of the environment is capable of reducing, or completely closing, the gap between the excited state PESs in the FC region, this will lead to strong coupling between excited states that is dependent on nuclear coordinates, resulting in a breakdown of the Condon approximation. In fact, for polyatomic systems, such crossings, known as conical intersections, are ubiquitous, however the Condon approximation can still be applied provided these crossings are far from the initial state equilibrium, representing rare events. When this is not the case, the strong coupling will lead to the optical character of the S_1 state becoming shared with S_2 , in an effect known as intensity borrowing. In this way it is possible for a dark state to become ‘visible’.

A simple model, capable of describing these dynamics is the linear vibronic coupling (LVC) model, which is introduced in the following subsection.

4.1.2 Linear Vibronic Coupling Model

We consider an LVC Hamiltonian with $\hat{\mathbf{q}}$ dependent coupling between the S_1 and S_2 states:

$$\hat{H}_{\text{LVC}} = \hat{H}_{\text{BOM}} + \delta(|S_1\rangle\langle S_2| + \text{h.c.}) + \overbrace{\sum_k \Lambda_k (|S_1\rangle\langle S_2| + \text{h.c.}) (a_{3,k}^\dagger + a_{3,k})}^{\hat{H}_1^\delta} + \sum_k \omega_{3,k} a_{3,k}^\dagger a_{3,k} \quad (4.13)$$

$$= \sum_{k,\alpha=1}^2 \omega_{0\alpha}^{\text{av}} |S_\alpha\rangle\langle S_\alpha| + \hat{H}_1^{\text{EL}} + \hat{H}_1^\delta + \sum_{k,\alpha=1}^3 \omega_{\alpha,k} a_{\alpha,k}^\dagger a_{\alpha,k}. \quad (4.14)$$

In the second line we have written the interaction Hamiltonian as the sum of two parts: the energy-level interaction Hamiltonian \hat{H}_1^{EL} (defined in Eq. (4.1)), and the coupling interaction Hamiltonian \hat{H}_1^δ . By moving to the LVC Hamiltonian we thus introduce a third bosonic bath, labelled $\alpha = 3$, which has off-diagonal coupling to the system. This bath is specified by the spectral density

$$J_{12}(\omega) = \sum_k |\Lambda_k|^2 \delta(\omega - \omega_k). \quad (4.15)$$

The average value of the electronic coupling is given by δ and is very small for MB ($\delta \sim 10^{-3}$ eV).

The spectral density of the coupling bath $J_{12}(\omega)$, can be obtained from MD simulations via the measurement of the autocorrelation $C_{12}^{\text{cl}}(t)$, following the same procedure as described above for the BOM. However, for the LVC Hamiltonian an addition step is required. Computing excitation energies from electronic structure methods such as time-dependent density functional theory (TDDFT) yields adiabatic electronic states, i.e. states that are electronically decoupled but can change their electronic character along the MD trajectory. Instead, to parameterise the LVC Hamiltonian, it is necessary to construct coupled, diabatic states that do not change character along the trajectory, and thus have constant ground to excited state transition dipole moments. The choice of diabatisation procedure is not unique. In this work we followed the diabatisation strategy previously outlined by Subotnik et al. [128]. This strategy consists of performing a basis transformation on the adiabatic states at each point along the MD trajectory. The transformation is chosen such that the difference between the ground to excited state transition dipole moments of the two states is maximised, thus yielding a bright and a dark state which are ‘quasi-diabatic’. The extent to which this diabatisation procedure changes the states provides a measure of how significant excited state crossings are; indeed, if the diabatisation had no effect, and the original states were already quasi-diabatic, the BOM could be applied directly. A quantitative measure for this is the reorganisation energy λ_{12}^{R} of the coupling bath.

Following this procedure, it is straightforward to construct the classical correlation functions $C_{01}^{\text{cl}}(t)$, $C_{02}^{\text{cl}}(t)$ and $C_{12}^{\text{cl}}(t)$ with respect to the diabatic states. The parameters ω_{01}^{av} , ω_{02}^{av} , δ , along with the dipole strengths V_{01} and V_{02} are obtained by averaging these quantities over the trajectories.

4.1.3 Molecular Dynamics and Electronic Structure Calculations

In this section we will provide some details of the molecular dynamics and electronic structure calculations carried out by our collaborators.

To sample the energy gap fluctuations needed to generate the necessary correlation functions and spectral densities of MB in water, four independent, 8 ps long, trajectories were generated. The trajectories were generated using mixed quantum mechanical/molecular mechanical (QM/MM) simulations using the TeraChem package [129]. The independent starting points for the trajectories were obtained from force field based molecular dynamics simulations performed using the OpenMM [130] package, where water was represented by the TIP3P [131] water model and the MB force field parameters were generated using the QUBEKit package [132].

In the QM/MM simulations the chromophore and its counter-ion were treated quantum mechanically with the CAM-B3LYP exchange-correlation functional [133] and 6-31+G* basis set, and all water molecules were described by the TIP3P force field. From these trajectories, snapshots were extracted every 2 fs for calculating vertical excitation energies, yielding a total of 16,000 snapshots from which the classical correlation functions were constructed.

Adiabatic excitation energies on each snapshot were computed using the TDDFT implemented in the TeraChem code [134]. To evaluate the influence of different choices of TDDFT functional on the S_1 - S_2 coupling, vertical excitation energies were computed both at the CAM-B3LYP/6-31+G* level of theory in the Tamm-Dancoff approximation (TDA), and at the B3LYP/6-31+G* level of theory using full TDDFT [133, 135]. This choice is motivated by the fact that the relative S_1/S_2 energy is very sensitive to the treatment of long range Hartree-Fock exchange in the density functional, mostly likely due to the strong charge-transfer character of the S_2 state, with the CAM-B3LYP functional predicting a larger energy difference between S_1 and S_2 .

To fully capture the influence of dynamic polarization of the environment on the energy gap fluctuations, excitation energies are computed by treating every solvent molecule with a center of mass within 6 Å from any chromophore atom fully quantum mechanically in the TDDFT calculation, with the remaining solvent atoms represented by classical point charges. This leads to a quantum mechanical region containing ≈ 400 atoms for the TDDFT calculations. Previously studies have shown that, for certain systems, couplings between solvent vibrations and electronic states can be highly sensitive to the treatment of polarisation effects in the environment [136]. In order to determine whether MB exhibits a similarly sensitivity, this quantum treatment is contrasted against a classical approach, wherein the entire solvent environment is represented by classical point charges and only the chromophore itself was treated quantum mechanically. Both the quantum solvent and classical solvent approaches, termed QM and MM respectively (cf. Fig. 4.1(b) and (c)), were repeated for the two functional choices, yielding four parameter data sets: CAM-B3LYP/QM, CAM-B3LYP/MM, B3LYP/QM and B3LYP/MM.

Figure 4.2(a) plots the three spectral densities, J_{01} , J_{02} and J_{12} obtained via the CAM-B3LYP/QM approach. The spectral densities show little variation across the

different treatments. The LVC parameters for all of the four treatments are collected in Tab. 4.1. We see that, across all treatments, the oscillator strength of the $S_0 \rightarrow S_2$ transition is about 5% that of the $S_0 \rightarrow S_1$ transition. Thus, in any approach based on the Condon approximation, we should expect the intensity due to S_2 to be a negligible 0.25% of that of S_1 . Where there exists significant variation is the S_1/S_2 ground state gaps Δ_{12} . In particular, adiabatic excitation energies calculated using the B3LYP functional lead to much smaller Δ_{12} than for CAM-B3LYP, and Δ_{12} even becomes negative when the solvent is treated classically. This is most likely due to the differing treatments of long-range exchange between the two functionals. As we shall see, the lineshape, is highly sensitive to the S_1/S_2 gap.

For full details on the computation of the model parameters, along with a detailed analysis of the computed spectral densities and model parameters, we refer to Ref. [123].

4.1.4 Calculating the Response Function

With the non-adiabatic excited state dynamics captured by the couplings in the LVC Hamiltonian, the response function may again be obtained assuming a nuclear coordinate independent dipole operator, following Eq. (4.6), (4.7) and (4.9).

However, in contrast to the BOM Hamiltonian, in the LVC model, the system and environment Hamiltonians no longer commute, rendering an analytical description of time-evolution unobtainable. To calculate $\chi(t)$, we therefore have need of the numerical methodology introduced in chapter 2 and utilised in chapter 3, namely T-TEDOPA. The key to comparison with experiment is the ability of T-TEDOPA to handle finite temperatures, since absorption spectra in water are naturally obtained at room temperature.

There are two main points in which the current application of the T-TEDOPA method differs from those in chapter 3. Firstly, the Hamiltonian (4.13) consists of a system coupled to three bosonic baths. As a result, the natural TN representation is in terms of tree-MPS/MPO (cf. Sec. 2.4.1). Secondly, the observable of interest is not the expectation of a simple operator, but a two-time correlation function. This latter poses a potential problem since, although the T-TEDOPA mapping preserves the dynamics of the system's reduced density matrix, it is not clear that the same can be said for arbitrary multi-time correlation functions. However, in the present case the response function can be shown to depend on a reduced density matrix for the system which has been time-evolved from a particular initial state, allowing the mapping to be correctly applied. Below, we set out the steps taken to arrive at this conclusion.

Firstly, we expand the thermal expectation of Eq. (4.7) and rearrange the contents using the cyclic property of the trace

$$\langle \hat{V}(t)\hat{V}(0) \rangle_{\rho(0)} = \text{Tr}\{e^{i\hat{H}t}\hat{V}e^{-i\hat{H}t}\hat{V}\rho(0)\} \quad (4.16)$$

$$= \text{Tr}\{\hat{V}e^{-i\hat{H}t}\hat{V}\rho(0)e^{i\hat{H}t}\}, \quad (4.17)$$

where Tr denotes the trace over all system and environment coordinates, and $\rho(0)$ is the initial system+environment density matrix in the original, non-T-TEDOPA-mapped,

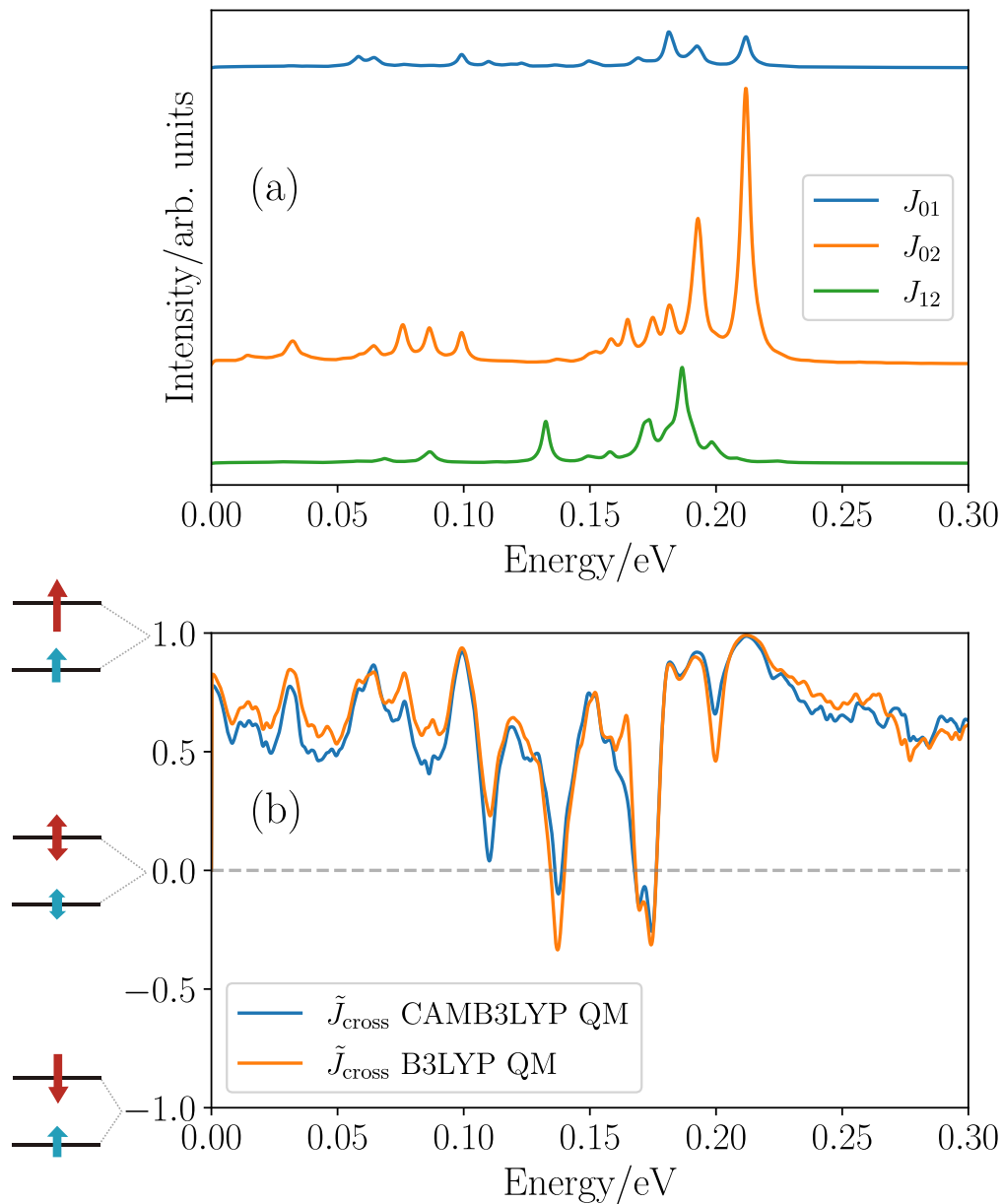


Figure 4.2: (a) Spectral densities of the diabatic S_1 and S_2 states, as well as the S_1/S_2 coupling spectral density as computed for the CAM-B3LYP data set in 6 Å explicit QM solvent. (b) The normalised cross-correlation spectral density, defined by $\tilde{J}_{\text{cross}}(\omega) = J_{\text{cross}}(\omega)/\sqrt{J_{01}(\omega)J_{02}(\omega)}$, shows the strength and parity of the correlations in the S_1 and S_2 energy fluctuations across the bath spectrum.

picture. We have also dropped the subscript from \hat{H}_{LVC} . Making use of the Condon approximation, we perform the trace over the environment degrees of freedom first giving

$$\langle \hat{V}(t)\hat{V}(0) \rangle_{\rho(0)} = \text{Tr}_{\text{S}}\{\hat{V}\text{Tr}_{\text{E}}\{e^{-i\hat{H}t}\hat{V}\rho(0)e^{i\hat{H}t}\}\} \quad (4.18)$$

$$= \text{Tr}_{\text{S}}\{\hat{V}\rho'_{\text{R}}(t)\} \quad (4.19)$$

$$= \langle \hat{V} \rangle_{\rho'_{\text{R}}(t)}. \quad (4.20)$$

Thus, the response function can be expressed as the expectation value of \hat{V} with respect to the reduced system density matrix $\rho'_{\text{R}}(t)$, which represents a state that has been time-evolved from the initial condition $\hat{V}\rho(0)$. Unfortunately, $\hat{V}\rho(0)$ does not represent a valid initial state, since it contains only off-diagonal components: $|S_1\rangle\langle S_0|$ and $|S_2\rangle\langle S_0|$; therefore, it is not possible to construct a simulation with $\hat{V}\rho(0)$ as an initial condition. Indeed, because \hat{V} is a Hermitian operator, its expectation cannot equate to that of a multi-time correlation function since the latter may be complex valued.

However, using the initial state $\rho'_{\text{S}}(0) = |\psi\rangle\langle\psi|$, where $|\psi\rangle = c(|S_0\rangle + V_{01}|S_1\rangle + V_{02}|S_2\rangle)$ and measuring the *non-Hermitian* operator $\hat{V}' = V_{01}|S_0\rangle\langle S_1| + V_{02}|S_0\rangle\langle S_2|$, we find exactly the same expectation value as we would have found had we measured \hat{V} with the invalid initial condition $\hat{V}\rho(0)$:

$$\chi(t) = \langle \hat{V}' \rangle_{\rho'_{\text{S}}(t)}. \quad (4.21)$$

This is because the LVC Hamiltonian does not mix S_1 or S_2 with S_0 , and thus the additional terms in ρ'_{S} , such as $|S_1\rangle\langle S_2|$, will be projected out by the measurement of \hat{V}' . As ρ'_{S} is a valid initial state, and as nothing prevents us from measuring a non-Hermitian operator, it is now straightforward to construct a simulation for $\chi(t)$.

	CAM-B3LYP		B3LYP	
	MM	6Å QM	MM	6Å QM
$ V_{01} $ (a.u.)	4.4027	4.3762	3.6116	3.6355
$ V_{02} $ (a.u.)	0.3752	0.3635	0.2147	0.2024
Δ_{01} (eV)	2.7371	2.6168	2.3543	2.2353
Δ_{02} (eV)	2.7983	2.7040	2.3286	2.2400
Δ_{12} (eV)	0.0612	0.0872	-0.0257	0.0046
λ_{01}^{R} (eV)	0.0525	0.0614	0.0572	0.0640
λ_{02}^{R} (eV)	0.2327	0.2659	0.2085	0.2363
ω_{12}^{av} (eV)	0.2409	0.2905	0.1251	0.1758
λ_{12}^{R} (eV)	0.0701	0.0698	0.0746	0.0725

Table 4.1: LVC Hamiltonian parameters obtained from the different data sets considered in this work.

4.1.5 Bath Correlations

Previously, we have assumed that the three fluctuation motions, corresponding to the energies of the two excited states and the coupling between them, were completely uncorrelated and could thus be treated as arising from three independent baths. While it is normally justified to assume that there is no correlation between the fluctuations of the coupling and those of the energy levels - the bath motions required for these two kinds of fluctuations being of very different natures - the same is not in general true for the fluctuations of the energy levels between themselves. Indeed, by measuring the cross-correlator of the S_1 and S_2 energy fluctuation operators along the MD trajectory

$$C_{\text{cross}}(t) = \langle \delta U_{01}(\hat{\mathbf{q}}, t) \delta U_{02}(\hat{\mathbf{q}}, 0) \rangle, \quad (4.22)$$

we find a strong, principally positive, correlation between these two motions for MB. Following Eq. (4.4), we are able to define a cross-correlation spectral density, which describes the nature of the correlations across frequency space:

$$J_{\text{cross}}(\omega) = i\theta(\omega) \int dt e^{i\omega t} \text{Im}\{C_{\text{cross}}(t)\}. \quad (4.23)$$

As a means of assessing quantitatively the strength and parity of these correlations, we define a dimensionless quantity which we call the normalised cross-correlation spectral density:

$$\tilde{J}_{\text{cross}} = \frac{J_{\text{cross}}}{\sqrt{J_{01}J_{02}}}. \quad (4.24)$$

This function takes values in the range $[1, -1]$ and is plotted for the CAM-B3LYP/QM and B3LYP/QM treatments in Fig. 4.2(b). The interpretation of this quantity is as follows. When $\tilde{J}_{\text{cross}} = 1$, the energy fluctuations of S_1 and S_2 are *fully positively correlated*; that is, a raising (or lowering) of the S_1 energy is associated with a simultaneous raising (or lowering) of the S_2 energy (although the amplitudes, which are determined by J_{01} and J_{02} , need not be the same) - the fluctuations have no independent character, so if we know the value of the S_1 energy at some point in time we immediately know the energy of S_2 . Conversely, when $\tilde{J}_{\text{cross}} = -1$, the fluctuations are *fully negatively correlated*; a raising (or lowering) of the S_1 energy is associated with a lowering (or raising) of the S_2 energy. Finally, when $\tilde{J}_{\text{cross}} = 0$, the fluctuating motions are *uncorrelated*; the excitation energies vary independently, as though connected to two independent sources of Gaussian noise.

From Fig. 4.2(b) we see that, with a few exceptions, the environmental modes are between 40% and 100% positively correlated. In particular, the most strongly coupled mode at 1690 cm^{-1} (0.21 eV) is almost completely fully positively correlated, while only at 890 cm^{-1} (0.11 eV), 1120 cm^{-1} (0.14 eV), and $1370/1400 \text{ cm}^{-1}$ (0.1699/0.1736 eV) are the motions uncorrelated or slightly anti-correlated.

In order to include these correlations into the LVC Hamiltonian we must modify the energy-level interaction Hamiltonian of the LVC. We do so by replacing the coupling

coefficients $g_{\alpha,k}$ of \hat{H}_I^{EL} with the 2×2 coupling *matrix* $g_{\alpha\beta,k}$:

$$\hat{H}_I^{\text{EL}} \mapsto \sum_k \sum_{\alpha\beta} g_{\alpha\beta,k} |S_\alpha\rangle \langle S_\alpha| (a_{\beta,k}^\dagger + a_{\beta,k}) \quad (4.25)$$

$$= \sum_k \left(|S_1\rangle \langle S_1| \quad |S_2\rangle \langle S_2| \right) \begin{pmatrix} g_{11,k} & g_{12,k} \\ g_{21,k} & g_{22,k} \end{pmatrix} \begin{pmatrix} a_{1,k}^\dagger + a_{1,k} \\ a_{2,k}^\dagger + a_{2,k} \end{pmatrix}. \quad (4.26)$$

Now, each harmonic bath couples to both the S_1 and S_2 energy levels. This interaction Hamiltonian is capable of describing arbitrary correlations between the S_1 and S_2 energy fluctuations. The coefficients $g_{\alpha\beta,k}$ must be chosen so as to reproduce the known spectral densities J_{01} , J_{02} , and J_{cross} . Since these three spectral densities offer a complete description of the reduced system dynamics, there exists a redundancy in our general prescription of H_I^{EL} above, which contains four free parameters. Introducing the parameters c_k , we therefore make the following simplification without any loss of generality:

$$g_{12,k} = c_k \gamma_{1,k}, \quad \text{where } \gamma_{1,k} = g_{11,k} \quad \text{and} \quad (4.27)$$

$$g_{21,k} = c_k \gamma_{2,k}, \quad \text{where } \gamma_{2,k} = g_{22,k}, \quad (4.28)$$

yielding

$$\hat{H}_I^{\text{EL}} = \sum_k \left(|S_1\rangle \langle S_1| \quad |S_2\rangle \langle S_2| \right) \begin{pmatrix} \gamma_{1,k} & c_k \gamma_{1,k} \\ c_k \gamma_{2,k} & \gamma_{2,k} \end{pmatrix} \begin{pmatrix} a_{1,k}^\dagger + a_{1,k} \\ a_{2,k}^\dagger + a_{2,k} \end{pmatrix}. \quad (4.29)$$

Before entering into the details of how to obtain $\gamma_{1,k}$, $\gamma_{2,k}$ and c_k from the spectral densities, we describe two limiting cases of the above interaction Hamiltonian.

Firstly, when the off-diagonal elements vanish ($c_k = 0 \forall k$), the coupling reduces to that of the BOM, whereby each excited state couples to its own independent bosonic bath. In this case there are no correlations between the fluctuation and thus we refer to this limit as the *uncorrelated* (UC) limit.

The second, opposing, limiting case occurs when the one of the eigenvalues of the matrix $g_{\alpha\beta,k}$ is zero, which implies $c_k = \pm 1 \forall k$. In this case, diagonalising the coupling matrix yields a collective electronic coordinate which couples to just *one* bath. For example, if $c_k = 1 \forall k$ we have

$$\hat{H}_I^{\text{EL}} = \sum_k (\gamma_{1,k} |S_1\rangle \langle S_1| + \gamma_{2,k} |S_2\rangle \langle S_2|) (b_k^\dagger + b_k), \quad (4.30)$$

where the bath operators are the linear combinations: $b_k^{(\dagger)} = a_{1,k}^{(\dagger)} + a_{2,k}^{(\dagger)}$. Here, the energy fluctuations of the two excited states are induced by the same set of modes and thus have no independent character, but instead move in synchrony. It is clear that this limit corresponds to the case where all modes are fully positively correlated, i.e. where $\tilde{J}_{\text{cross}}(\omega) = 1 \forall \omega$. We thus refer to this limit as the fully positively correlated (FPC) limit. One could also consider the case where $c_k = -1 \forall k$. In this case we would again

have a coupling of one bath to a collective electronic coordinate, except now the coupling operator would be $\gamma_{1,k} |S_1\rangle \langle S_1| - \gamma_{2,k} |S_2\rangle \langle S_2|$. We recognise this as the fully negatively correlated (FNC) limit where $\tilde{J}_{\text{cross}}(\omega) = -1 \forall \omega$.

We interest ourselves in this FPC limit for two reasons: first, it is interesting to consider, from a theoretical point of view, the effect of correlated energy fluctuations on the absorption spectra and excited state dynamics; second, given that for MB most modes are strongly positively correlated, the FPC limit represents a reasonable approximation which carries with it a significant reduction in computational overhead, because of the need to simulate only one bath. The FNC limit on the other hand is less interesting for MB and we will not consider it further.

In general of course, and in particular for MB, one will be in neither of these two limits; instead correlations will be partial and frequency dependent. We refer to the model in this general case, in what follows, as *Molecular dynamics Correlated* (MDC), since one is using the information contained in J_{cross} , obtained from MD.

In the next section we will derive the relations between the correlated LVC parameters and the spectral densities.

4.1.6 Parameterising the Correlated LVC Hamiltonian

The task is to determine the parameters $\gamma_{1,k}$, $\gamma_{2,k}$ and c_k in terms of the known spectral densities $J_{01}(\omega)$, $J_{02}(\omega)$ and $J_{\text{cross}}(\omega)$. The following derivation is independent of the TEDOPA thermal mapping, thus, to include the effects of temperature, one can simply apply the following to the thermal spectral densities $J_{01}(\omega, \beta)$, etc.

We begin by defining continuous spectral densities based on the parameters:

$$G_\alpha(\omega) := \sum_k |\gamma_{\alpha,k}|^2 \delta(\omega - \omega_k), \text{ for } \alpha \in [1, 2] \quad (4.31)$$

$$C(\omega) := \sum_k |c_k|^2 \delta(\omega - \omega_k). \quad (4.32)$$

The link is provided by the definitions (4.4) and (4.23) which relate the spectral densities to the energy gap autocorrelation functions. The energy gap fluctuation operators for the correlated LVC Hamiltonian are given by

$$\delta U_{01} = \int d\omega \sqrt{G_1(\omega)} (a_1^\dagger(\omega) + a_1(\omega)) + \sqrt{C(\omega)G_1(\omega)} (a_2^\dagger(\omega) + a_2(\omega)), \quad (4.33)$$

$$\delta U_{02} = \int d\omega \sqrt{G_2(\omega)} (a_2^\dagger(\omega) + a_2(\omega)) + \sqrt{C(\omega)G_2(\omega)} (a_1^\dagger(\omega) + a_1(\omega)). \quad (4.34)$$

Substituting these expressions into the definitions (4.4) and (4.23) we obtain

$$J_{0\alpha}(\omega) = G_\alpha(\omega)(1 + C(\omega)), \text{ for } \alpha \in [1, 2] \quad (4.35)$$

$$J_{\text{cross}}(\omega) = 2\sqrt{G_1(\omega)G_2(\omega)C(\omega)}. \quad (4.36)$$

Equations (4.35) and (4.36) constitute a system of non-linear equations with G_1 , G_2 , and C as unknowns. Solving for C we obtain two solutions:

$$C(\omega) = \frac{2J_{01}(\omega)J_{02}(\omega)}{J_{\text{cross}}(\omega)^2} \left(1 \pm \sqrt{1 - \frac{J_{\text{cross}}(\omega)^2}{J_{01}(\omega)J_{02}(\omega)}} \right) - 1, \quad (4.37)$$

of which, the solution with the positive root may be discarded as it diverges in the uncorrelated limit ($J_{\text{cross}} = 0$). With the function $C(\omega)$ determined, we obtain the spectral densities $G_\alpha(\omega)$ via the expression

$$G_\alpha(\omega) = \frac{J_{\text{cross}}(\omega)^2}{2J_{0\bar{\alpha}}(\omega) \left(1 - \sqrt{1 - \frac{J_{\text{cross}}(\omega)^2}{J_{01}(\omega)J_{02}(\omega)}} \right)}, \quad (4.38)$$

where $\bar{\alpha} = 1(2)$ when $\alpha = 2(1)$. It is easy to check that in the FPC (FNC) and limits, where $J_{\text{cross}}(\omega) = +(-)\sqrt{J_{01}(\omega)J_{02}(\omega)}$, these expressions reduce to $C(\omega) = +(-)1$ and $G_\alpha(\omega) = \frac{1}{2}J_{0\alpha}(\omega)$; while, in the UC limit, with $J_{\text{cross}}(\omega) = 0$, we have $C(\omega) = 0$ and $G_\alpha(\omega) = J_{0\alpha}(\omega)$.

In the next section we will apply the chain mapping to the correlated LVC Hamiltonian and explore the various TN structures that arise in the UC, FPC and MDC cases.

4.1.7 The Chain Mapping in the Correlated LVC model

In order to render the correlated LVC model amenable to MPS methods, it is necessary to perform the chain mapping that will transform it into a 1D or quasi-1D topology. However, the correlated LVC model is not of the form that one typically associates with the chain mapping. Writing the interaction operator in terms of the continuous spectral densities

$$H_I^{\text{EL}} = \sum_{\alpha=1}^2 \int d\omega \left(\sqrt{G_\alpha(\omega)} |S_\alpha\rangle \langle S_\alpha| + \sqrt{C(\omega)G_{\bar{\alpha}}(\omega)} |S_{\bar{\alpha}}\rangle \langle S_{\bar{\alpha}}| \right) \left(a_\alpha^\dagger(\omega) + a_\alpha(\omega) \right), \quad (4.39)$$

we see that each bath essentially couples to the system via two spectral densities: $G_\alpha(\omega)$ and $C(\omega)G_{\bar{\alpha}}(\omega)$. As a result, there is no unique spectral density for which one can construct orthogonal polynomials. We choose, nonetheless, to perform chain mappings with respect to $G_\alpha(\omega)$. The new chain modes are defined as

$$b_{\alpha,n}^{(\dagger)} = \int d\omega U_{\alpha,n}(\omega) a_\alpha^\dagger(\omega), \quad (4.40)$$

where the unitary transformation is given by

$$U_{\alpha,n}(\omega) = \sqrt{G_\alpha(\omega)} \tilde{p}_{\alpha,n}(\omega) \quad (4.41)$$

and $\tilde{p}_{\alpha,n}(\omega)$ are orthonormal polynomials satisfying

$$\int d\omega G_\alpha(\omega) \tilde{p}_{\alpha,n}(\omega) \tilde{p}_{\alpha,m}(\omega) = \delta_{n,m}. \quad (4.42)$$

Expressing the interaction Hamiltonian in terms of these new modes yields,

$$H_1^{\text{EL}} = \sum_{\alpha=1}^2 \sum_{n=0}^{\infty} \left(\underbrace{\int d\omega G_{\alpha}(\omega) \tilde{p}_{\alpha,n}(\omega) |S_{\alpha}\rangle \langle S_{\alpha}|}_{=\delta_{n,0}/\tilde{p}_{\alpha,0}} + \underbrace{\frac{1}{2} \int d\omega J_{\text{cross}}(\omega) \tilde{p}_{\alpha,n}(\omega) |S_{\bar{\alpha}}\rangle \langle S_{\bar{\alpha}}|}_{:=\kappa_{\alpha,n}} \right) (b_{\alpha,n}^{\dagger} + b_{\alpha,n}), \quad (4.43)$$

where we have used Eq. (4.36) to substitute in $J_{\text{cross}}(\omega)$. Note that it is important to use the original $J_{\text{cross}}(\omega)$ in this expression rather than substituting the solution for $C(\omega)$ into Eq. (4.37), as in doing so one would lose the information pertaining to the parity of the correlations.

As indicated in Eq. 4.43, the diagonal couplings reduce to a local interaction between the system energy level and the first site on the chain. For the off-diagonal couplings however, no such simplification is possible as J_{cross} bears no relationship in general to the polynomials $\tilde{p}_{\alpha,n}(\omega)$. Instead, the energy level couples to every chain mode via the long-range coupling coefficients $\kappa_{\alpha,n}$, determined via the integrals.

Figure 4.3 depicts the MPS structures for the correlated LVC model in the three limits. In the UC limit, shown in panel ‘a’ of Fig. 4.3, the baths necessitate a tree structure but, due to the absence of off-diagonal couplings, there are no long-range interactions. In the FPC limit on the other hand, shown in panel ‘b’, there is only one bath controlling the excited state energy fluctuations and thus we return to a simple chain topology; however, the off-diagonal couplings lead to long-range couplings. Finally, panel ‘c’ shows the general, MDC, case. Here, we have both a tree structure *and* long-range couplings, making this the most computationally expensive model.

4.1.8 Results

Having described our methodologies in some detail, we move on to the presentation and discussion of the resulting spectra and to the comparison with experiment. We note that, whenever a calculated spectrum is compared with experiment, a frequency shift has been applied to the calculated spectrum such that the main peaks coincide. Whenever this occurs, the size of the shift will be indicated. In addition, absorption intensities have been normalised such that the main peak intensities match. We take our reference experimental MB absorption spectrum from Ref. [137]. The spectrum was measured at low MB concentration in water and so should represent the monomeric spectrum. All spectra were calculated at room temperature which we took to be 300 K.

We begin by justifying the use of the innovative, and computationally expensive, techniques described above by presenting some results obtained by our collaborators, which demonstrate the failure of Condon-based approaches to explain the experimental lineshape.

Failure of the Condon approximation

Figure 4.4(a) shows the experimental lineshape of MB compared against two static Frank-Condon (FC) lineshapes: Adiabatic Hessian Frank-Condon (AHFC) and Vertical

Gradient Frank-Condon (VGFC); and a lineshape based on a third order cumulant expansion. These approaches are all based on the Condon approximation for a single bright excited state.

The FC lineshapes are computed from static information about the environment; namely the frequencies of the ground and excited states in the optimised structures. For the VGFC lineshape, the underlying model is the purely linear BOM, whereas the AHFC lineshape is based on the GBOM and thus accounts for the non-linear effects of differing curvatures of excited state PESs and rotations of the oscillator basis between ground and excited states (Duschinsky rotations). The third order cumulant lineshape, on the other hand, takes dynamical input from the bath via the second and third order autocorrelation functions of the energy gap fluctuation operators. Including the third order cumulant allows some non-linear, beyond-BOM, effects to be taken into account.

The VGFC lineshape is significantly under-broadened and the high energy tail is dominated by two vibronic peaks. In the AHFC approach these vibronic peaks are smoothed into two shoulders and the whole spectrum is broader, suggesting that Duschinsky rotations are important for treating low frequency solvent modes. The third order cumulant lineshape is broader still and, inline with the experimental spectrum, the high energy tail consists of a single shoulder, albeit with a highly under-estimated intensity. The general conclusion, however, is that all of these lineshapes fail to reproduce the experimental spectrum - being all under-broadened and lacking in shoulder intensity. This motivates the move beyond the Condon approximation.

Finally, we comment on the results presented in Fig. 4.4(b), which compare the second and third order cumulant lineshapes. The relative similarity of these two lineshapes can be taken as evidence that non-linear couplings to the excited states are small, thus supporting the BOM as the underlying model for the energy level fluctuations, despite the differences between the AHFC and VGFC results. We note however that this result does not tell us anything about how well the S_1 - S_2 coupling is modelled by the LVC model.

While all results presented here pertain to the CAM-B3LYP functional, these conclusions are robust with respect to functional choice [123].

Bath correlations

In this section we will compare spectra and excitation dynamics computed with T-TEDOPA for the different treatments of bath correlations discussed in Sec. 4.1.5. In Fig. 4.5 we plot the lineshapes, alongside the excited state population dynamics, obtained for the LVC model with fluctuations treated as UC, FPC, and MDC. Also plotted in Fig. 4.5(a) is a lineshape obtained with the S_1 - S_2 coupling turned off (labelled ‘No Coupling’) in the LVC Hamiltonian. This latter should be almost identical to the second-order cumulant lineshape presented in the previous section (the only difference should be the tiny contribution of S_2) and can thus be used to validate our method. The ‘No Coupling’ lineshape also serves as a benchmark for evaluating the effects of S_1 - S_2 state mixing.

We find that turning on S_1 - S_2 coupling, however the correlations are treated, has

the effect of causing population transfer to the dark S_2 state which in turn lowers the intensity of the main peak in the absorption and raises the shoulder, thus improving agreement with experiment. Since spectra intensity are normalised, the lowering of the main peak intensity has the effect of decreasing the sharpness of the low energy absorption onset. We also observe from the values of the frequency shifts given in the legend of Fig. 4.5(a) that turning on the coupling also causes a red-shift of $\approx 0.03\text{eV}$.

The initial 8 fs of the excited state dynamics, which sees a $\sim 15\%$ depopulation of S_1 into S_2 , is largely independent of how bath correlations are treated. Following this initial 8 fs, the bath correlations begin to play a role. For the UC baths, after 8 fs, apart from some minor oscillations, there is little further population transfer and the system settles into a mixed S_1/S_2 steady state. For the correlated baths, however, after 8 fs there is a second, significant population transfer to S_2 after the first oscillation, and instead of forming a steady state with a fixed proportion of S_2 , oscillations persist until at least 240 fs. These effects are most acute for the FPC baths since the correlations are the strongest. While the change in the spectrum was quite small for the uncorrelated baths, the correlation driven S_2 population transfer improves experimental agreement significantly by raising the shoulder further and smoothing the onset. Indeed, the onset for the FPC and MDC lineshapes agrees very well with experiment. We note that, while the FPC lineshape seems a better match to experiment, this treatment should actually be considered less accurate than MDC since the detailed information contained in \tilde{J}_{cross} is not taken into account. Broadly speaking however the FPC and MDC lineshapes do not differ by much, which can be rationalised by the fact that, according to the \tilde{J}_{cross} , bath modes are on average 80% correlated.

While it is clear that the inclusion of non-Condon effects in conjunction with correlated baths improves agreement with experiment, there remains a significant discrepancy to overcome.

Influence of the S_1 - S_2 gap

In the preceding section we established the importance of population transfer to the dark S_2 state on the absorption lineshape and showed that increased S_1 - S_2 mixing lead to improved agreement with experiment. In Sec. 4.1.3 we noted that the S_1 - S_2 gap ω_{12}^{av} was highly dependent on the choice of density functional (CAM-B3LYP vs B3LYP) and to a lesser extent on the solvent treatment (QM/MM). Indeed, we see from Tab. 4.1 that ω_{12}^{av} has a range of 0.165eV (i.e. 56% of its maximum value). Considering a wider selection of density functionals increases this range still further; results reported in Ref. [123] have values for ω_{12}^{av} in the range 0.06 to 0.67eV. This sensitivity can be attributed to the strong charge transfer character of the S_2 state. Given the role of excited state mixing on the lineshape, we may expect a strong sensitivity to functional choice, since a narrower gap will lead to increased mixing.

This expectation is born out by the results shown in Fig. 4.6 where we compare parameter sets while treating bath correlations in the most accurate way (MDC). We see that the lineshape is highly dependent on functional choice, and to a lesser extent, solvent treatment. From Fig. 4.6(b) we see that when the S_1 - S_2 gap is smaller there is

increased mixing and thus a greater proportion of S_2 in the steady state. On the other hand, in comparing the lineshapes with the population dynamics shown, respectively, in Fig. 4.6(a) and Fig. 4.6(b), we see that, while there is clearly a strong correlation between excited state mixing and the intensity of the spectral shoulder, the differing bath structures, that is, the spectral densities J_{01} , J_{02} , J_{12} and J_{cross} , also play a role. This is clear from the comparison of CAM-B3LYP/QM and CAM-B3LYP/MM. The gap is smaller in CAMB3LYP/MM leading to greater mixing, however the lineshape is less broad and its shoulder less rounded. It appears, nonetheless, that population transfer to the S_2 state is the main factor in accounting for the broad shoulder in the linear absorption spectrum of MB in water.

Ideally, one would be able to accurately determine the S_1 - S_2 gap using higher-level electronic structure methods; however, the size of the MB molecule, along with the importance of solvent polarisation effects, means that this is not currently possible. Instead, in order to see whether, with the right amount of dark state mixing, it is possible to fully reproduce the experimental shoulder, we take the CAM-B3LYP/QM parameter set and artificially reduce the S_1 - S_2 gap by increments of 20%. With the gap reduced by 80% we reach the lowest value found in Ref.[123] of 0.06eV. The results are shown in Fig. 4.7 for the MDC treatment of fluctuations. We find that reducing the gap by 60% gives the best agreement to experiment, while reducing the gap by 80% gives an over-broadened lineshape. Looking at the population dynamics in Fig. 4.7(b) we see that beyond 40% the steady state is actually dominated by S_2 suggesting an inversion of S_1 and S_2 in the relaxed system. Also notable in Fig. 4.7(b) is the fact that the oscillation structure in the population dynamics is very similar across the different gap values, in contrast to the population dynamics in Fig. 4.6(b) where the bath structures are also changing.

Regarding the initial oscillation in the S_1/S_2 populations, we find that the frequency is proportional to the S_1 - S_2 gap, suggesting that this initial population transfer takes place in the FC region.

To highlight the importance of fluctuation correlations in the MB spectrum, we repeat this experiment of reducing the gap for the uncorrelated LVC model. As shown in Fig. 4.8(a) even with the gap reduced by 80% (the lowest reasonable value) the main peak is still under-broadened and the shape highly unsatisfactory.

While the shoulder intensity increases as the gap is reduced, its shape simultaneously deteriorates. Thus, even with an artificially reduced gap, we are unable to fully reproduce the experimental lineshape. This is no doubt in part down to the fact that, in addition to the gap, the bath spectral densities (in particular the coupling and cross-correlation spectral densities) are not perfectly accurate. Better electronic structure methodologies may, in the future, lead to more accurate parameterisations and finally close the gap between theory and experiment. It is also likely that, to fully explain the absorption spectrum of MB in water, one would need to go beyond the LVC model to include non-linear effects. Where non-linear effects may be especially important is in the S_1 - S_2 coupling fluctuations, as we were unable to determine their strength, unlike the energy-level fluctuations which were shown to be weak by the comparison between second and

third order cumulants.

4.2 Conclusion

In this chapter we have presented a novel methodology for computing absorption spectra of chromophores in complex condensed phase environments at finite temperatures, which combines *ab initio* molecular dynamics and TDDFT with numerically exact quantum dynamics using tensor networks. This methodology is highly attractive; being able to capture the effects of solvent polarisation, anharmonicity, and non-Condon effects, in a computationally efficient way. Cross correlations in environment induced fluctuations are able to be treated via the inclusion of long-range interaction terms in the chain-mapped Hamiltonian.

We presented these methods through the case study of Methylene blue, whose spectrum presents a large and unexplained shoulder. We were able to demonstrate the role of vibrationally driven population transfer from the bright S_1 state to the dark S_2 state in the formation of this shoulder.

The method can readily be applied to more complex systems with a larger number of states and environmental interactions. In addition, it should also be possible to extract higher-order response functions for computing more complex spectroscopic signals [117]. Another possibility for future work is the calculation of emission spectra which would most likely require combining real-time evolution with DMRG, used to determine the emitting state.

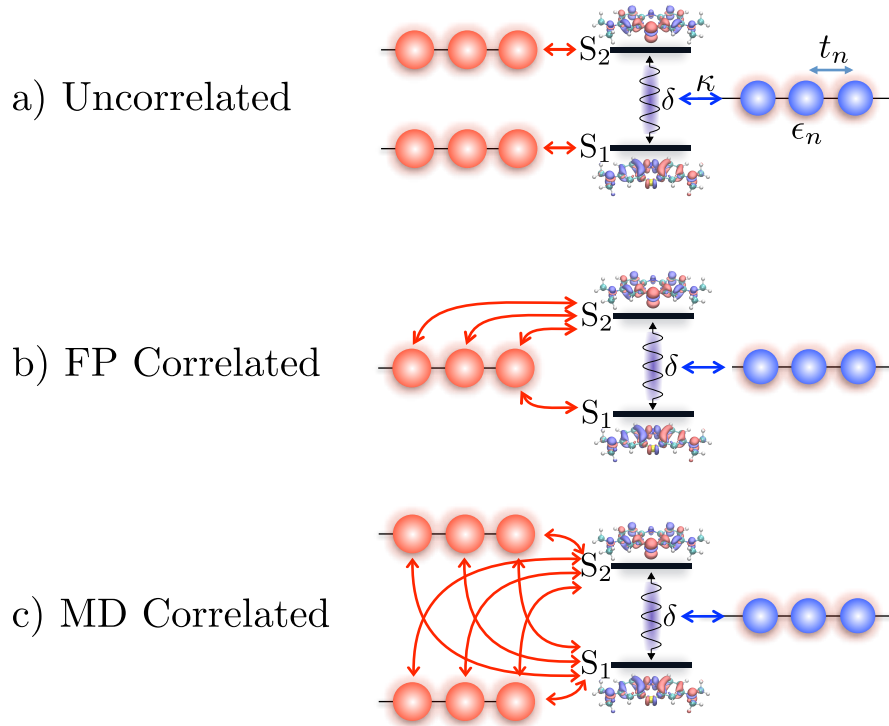


Figure 4.3: Tensor network structures used for the various bath configurations considered. (a) Uncorrelated baths, tree-MPS with local interactions only. (b) FPC baths, chain-MPS with some long-range interactions. (c) MDC baths, tree-MPS with long-range couplings. Bath modes involved in H_1^δ (coupling) are shown in blue, while bath modes involved in H_1^{EL} are shown in red (tuning). While interactions between the system and the tuning modes may become long-ranged, all intra-chain couplings are nearest-neighbour (t_n) for oscillators of frequency ϵ_n .

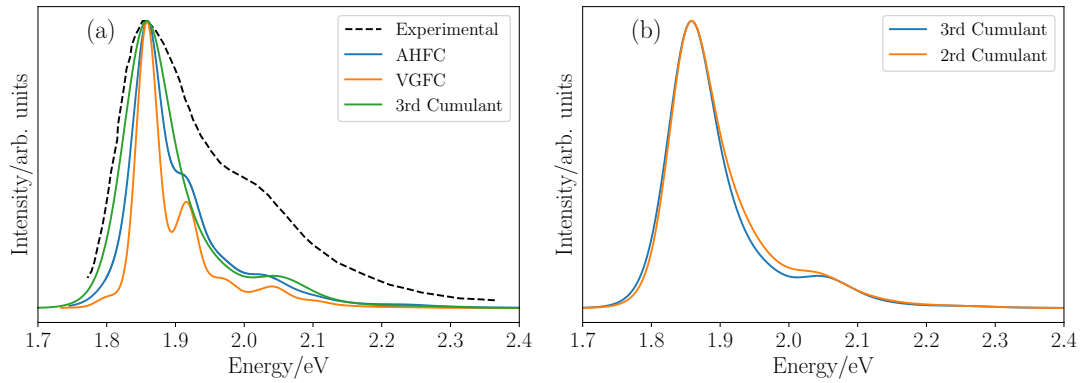


Figure 4.4: (a) Condon type spectra compared against the experimental MB absorption spectrum. All spectra are under-broadened and do not reproduce the strong shoulder. (b) Comparison of second and third order cumulant lineshapes - the similarity suggests that non-linear effects are small.

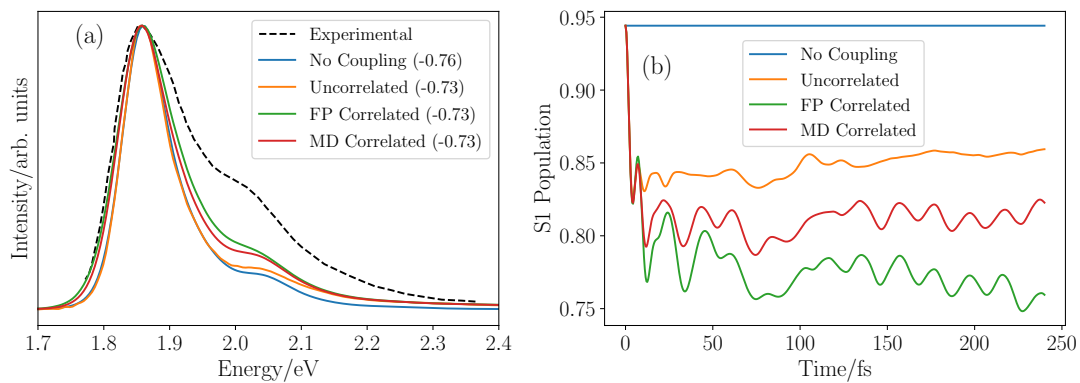


Figure 4.5: Spectra (panel ‘a’) and population dynamics (panel ‘b’) for the different treatments of bath correlations. Frequency shifts are given in eV in the legend of panel ‘a’. These data pertain to the CAM-B3LYP/QM parameter set for which the average gap in the Condon region is given by $\omega_{12}^{\text{av}} = 0.29\text{eV}$.

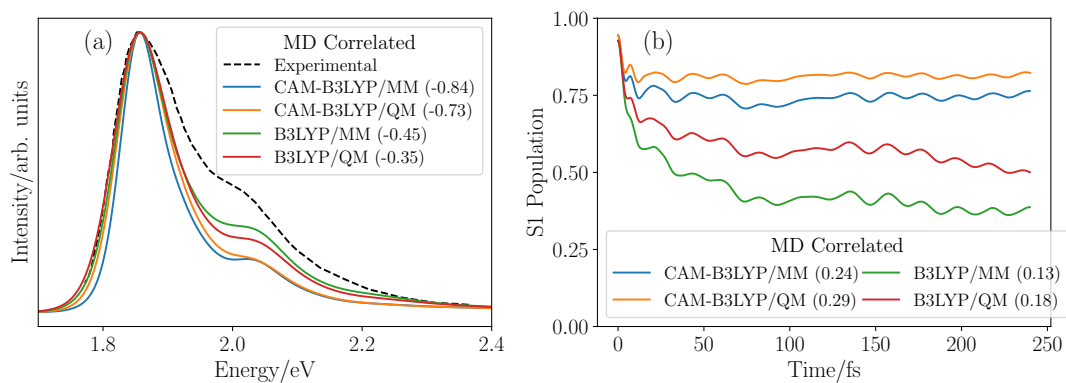


Figure 4.6: Spectra (panel ‘a’) and population dynamics (panel ‘b’) for the different LVC parameter sets considered. Fluctuations are MDC, which is the most accurate treatment. Frequency shifts are given in eV in the legend of panel ‘a’ and S_1 - S_2 gap values, also in eV, are given in the panel ‘b’ legend.

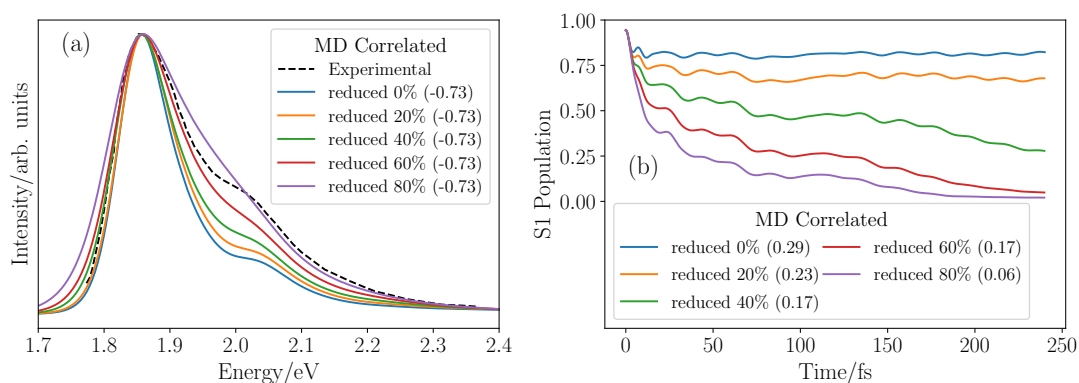


Figure 4.7: Reducing the S_1 - S_2 gap in the CAM-B3LYP/QM parameter set for MDC fluctuations. Frequency shifts are given in eV in the legend of panel ‘a’ and S_1 - S_2 gap values, also in eV, are given in the panel ‘b’ legend.

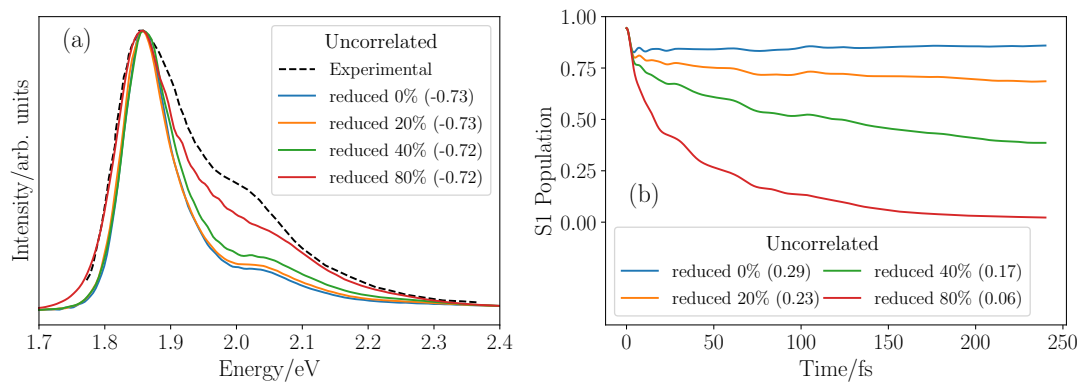


Figure 4.8: Reducing the S_1 - S_2 gap in the CAM-B3LYP/QM parameter set for UC fluctuations. Frequency shifts are given in eV in the legend of panel 'a' and S_1 - S_2 gap values, also in eV, are given in the panel 'b' legend.

Chapter 5

Adaptive 1TDVP

In this final chapter we shall return to the underlying MPS time evolution algorithms that have been central to all results presented in this thesis. In particular, we shall address the questions raised in Sec. 2.2.2 regarding the problem of fixed bond dimensions in the one-site TDVP (1TDVP) method. We concluded in that section that 1TDVP possessed a major disadvantage in the fixed nature of the MPS bond dimensions, and that this was a particular problem for the class of model we consider in this work, in which the initial condition is a product state. We further concluded that, despite the existence of a two-site variant of TDVP (2TDVP), there was no satisfactory solution; that either, in sticking with 1TDVP, one had to embed the initial MPS into one with a chosen set of bond dimensions, in which case the MPS would inevitably be highly non-optimal, and furthermore, the only way to determine appropriate bond dimensions would be to perform multiple costly converge runs; or, one had to accept the bad scaling and non-unitarity of 2TDVP.

The consideration of these issues has lead us to develop a new variant of TDVP which attempts to combine the best of both one- and two-site TDVP. This new variant, which we call adaptive one-site TDVP (A1TDVP) [138], has the same scaling properties as 1TDVP, is unitary and will conserve any constants of motion, while, at the same time, allowing bond dimensions to grow adaptively in response to emerging entanglement.

Towards the completion of this work we became aware of the paper by Yang and White [139], in which the authors develop a variant of 1TDVP aimed at tackling the same problem as presented above, by using global Krylov vectors to enrich the MPS in between 1TDVP sweeps. The resulting time evolution algorithm allows bond dimensions to grow adaptively, whilst preserving unitarity and conserving constants of motion. While both their method and ours achieve the same goal, they do so in distinct ways; in particular, they differ in the means of expanding the state space. A comparison between A1TDVP and the method of Yang and White would make an interesting subject for future work. Progress towards an adaptive version of TDVP has also been made by Zauner-Stauber et al. [140], who used a TDVP inspired, projector based approach as a means of optimally approximating an MPS. Such an approach can provide better fidelity compared to traditional MPS approximation methods based on truncation of singular

values, which are only locally optimal. Importantly, their framework also allows for the variational MPS to have a larger bond dimension than in its initial state, and could thus be potentially combined with 1TDVP to produce a bond adaptive version. Such an approach could be especially versatile as it could also include the possibility of bond dimensions *decreasing* during the time evolution. The current version of the algorithm, however, is limited to uniform MPS.

The structure of this chapter is as follows: in Sec. 5.1 we describe the A1TDVP method and show that it is efficient and scales no worse than 1TDVP; then, in Sec. 5.2 we provide a numerical verification of the method by revisiting the two-bath spin-boson model, showing that A1TDVP is capable of producing converged dynamics in a fraction of the time required by either one- or two-site TDVP; and finally, in Sec. 5.3 we give some consideration to the deficiencies of the method in its current form and to how these might be alleviated in future work. Much of the material presented in this chapter has also been published in Ref. [138].

5.1 Method

The A1TDVP method is based on the idea of sub-space expansion which has its origin in DMRG [141]. In Sec. 2.1.5 we introduced the so called ‘thin’ version of the QR decomposition which was central to MPS manipulation and to the construction of the projectors in one- and two-site TDVP. In A1TDVP, the projectors will be constructed using a different version of QR known as ‘full’ QR.

5.1.1 Full QR Decomposition

The full QR decomposition takes an $m \times n$ matrix M , where $m \geq n$ and writes it as the product of an $m \times m$ unitary matrix Q and an $m \times n$ upper-triangular matrix R :

$$\text{---}m\text{---} \textcircled{M} \text{---}n\text{---} = \text{---}m\text{---} \textcircled{Q} \text{---}m\text{---} \textcircled{R} \text{---}n\text{---} . \quad (5.1)$$

Since R is upper triangular, its bottom $m - n$ rows are all zero. Thus, when multiplying Q and R together, the right-most $m - n$ columns of Q will meet these $m - n$ zero-rows and be nullified. This is most usefully expressed by separating Q and R into blocks:

$$M = QR = \begin{pmatrix} Q_1 & Q_2 \end{pmatrix} \begin{pmatrix} R_1 \\ 0 \end{pmatrix} = Q_1 R_1, \quad (5.2)$$

where Q_1 is an $m \times n$ matrix whose columns are mutually orthonormal, Q_2 is an $m \times m - n$ matrix whose columns are also mutually orthonormal and are also orthogonal to the columns of Q_1 , and R_1 is an $n \times n$ upper-triangular matrix. Since the result of the multiplication is independent of Q_2 , this block is often discarded to yield the thin QR decomposition $Q_1 R_1$, which is the version introduced in Sec. 2.1.5 (cf. Eq. (2.50)). We recognise the matrix Q_1 as providing the left orthogonal MPS site tensors which output the n most relevant linear combinations of the m input states ($m = dD_L$).

The matrix Q_2 is not unique and is defined only by its orthogonality properties; its $m - n$ orthogonal columns complete the set of basis states contained in Q_1 . Rather than retaining *all* the columns of Q_2 , one could choose to keep just some, to obtain something in between a full and a thin QR. By keeping just *some* of the columns of Q_2 , one can progressively *expand* the basis of output states. This is precisely the idea of sub-space expansion which is central to A1TDVP.

Just as with the thin QR, the mirror image of the above, known as the full LQ, is necessary for obtaining right orthogonal MPS site tensors with expanded sub-spaces:

$$-m-\textcircled{M}-n- = -m-\diamond L-n-\triangleleft Q-n-, \quad (5.3)$$

where now $n \geq m$. This concept of full versus thin can also be extended to the SVD.

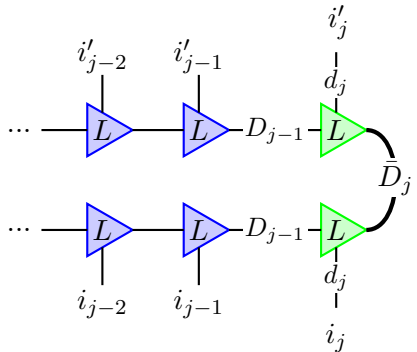
5.1.2 Sub-space Expansion in the one-site Projector

The vectors contained in Q_2 can thus be used to expand the sub-spaces of individual MPS site tensors such that the truncations that they affect are made less severe. One could imagine replacing the thin QRs (or SVDs) in the procedure for forming the left canonical gauge (cf. Eq. (2.21)-(2.25)) with full ones as a means of increasing the MPS bond dimension. Doing so would of course produce a rank-deficient MPS, since the additional states have been added artificially and the MPS was originally full-ranked; the left bond dimension of each site would need to be augmented with zero-rows in order to accommodate the extra states output by the site to its left. In fact, this procedure is completely equivalent to the embedding strategy of Eq. (2.75).

Alternatively, one can apply sub-space expansion to the projectors used in TDVP. Recalling the expression for the projector onto the space of one-site variations:

$$\hat{P}_{T|\psi, \mathcal{M}} = \sum_{j=1}^N \hat{P}_{j-1}^{L, |\psi\rangle} \otimes \hat{\mathbf{1}}_j \otimes \hat{P}_{j+1}^{R, |\psi\rangle} - \sum_{j=1}^{N-1} \hat{P}_j^{L, |\psi\rangle} \otimes \hat{P}_{j+1}^{R, |\psi\rangle}, \quad (5.4)$$

one can modify $\hat{P}_j^{L(R), |\psi(t)\rangle}$ by adding states from Q_2 so as to form a projector onto a higher dimensional manifold:

$$\hat{P}_j^{L, |\psi\rangle} \mapsto \hat{P}_j^{L, |\psi'\rangle}(\bar{D}_j) :=$$


$$(5.5)$$

where $D_j \leq \bar{D}_j \leq d_j D_{j-1}$; and

$$\hat{P}_j^{R,|\psi\rangle} \mapsto \hat{P}_j^{R,|\psi'\rangle}(\bar{D}_{j-1}) := \bar{D}_{j-1} \begin{array}{c} \begin{array}{c} i'_j \\ | \\ d_j \\ \downarrow \\ \text{R} \end{array} \text{---} D_j \text{---} \begin{array}{c} i'_{j+1} \\ | \\ \text{R} \end{array} \text{---} \begin{array}{c} i'_{j+2} \\ | \\ \text{R} \end{array} \text{---} \dots \\ \bar{D}_{j-1} \\ \begin{array}{c} \text{R} \\ | \\ d_j \\ \downarrow \\ i_j \end{array} \text{---} D_j \text{---} \begin{array}{c} i_{j+1} \\ | \\ \text{R} \end{array} \text{---} \begin{array}{c} i_{j+2} \\ | \\ \text{R} \end{array} \text{---} \dots \end{array}, \quad (5.6)$$

where $D_{j-1} \leq \bar{D}_{j-1} \leq d_j D_j$. In the above expressions, we have used green to indicate the site tensors that have been expanded. The projector is now determined by the rank-deficient MPS $|\psi'\rangle$. In this way, the one-site projector $\hat{P}_{T_{|\psi\rangle}, \mathcal{M}}$ becomes dependent on the set of bond dimensions $\bar{\mathbf{D}} := \{\bar{D}_j \text{ for } j \in [1, N-1]\}$, which may be chosen to be larger than the current set of MPS bond dimensions $\mathbf{D} := \{D_j \text{ for } j \in [1, N-1]\}$:

$$\hat{P}_{T_{|\psi'\rangle}, \mathcal{M}}(\bar{\mathbf{D}}) = \sum_{j=1}^N \hat{P}_{j-1}^{L,|\psi'\rangle}(\bar{D}_{j-1}) \otimes \hat{\mathbf{1}}_j \otimes \hat{P}_{j+1}^{R,|\psi'\rangle}(\bar{D}_j) - \sum_{j=1}^{N-1} \hat{P}_j^{L,|\psi'\rangle}(\bar{D}_j) \otimes \hat{P}_{j+1}^{R,|\psi'\rangle}(\bar{D}_j). \quad (5.7)$$

Of course, one may also choose $\bar{\mathbf{D}} = \mathbf{D}$, in which case we recover the fixed bond dimension projector of 1TDVP: $\hat{P}_{T_{|\psi'\rangle}, \mathcal{M}}(\mathbf{D}) = \hat{P}_{T_{|\psi\rangle}, \mathcal{M}}$. Then, substituting for these projectors in Eq. (2.62) and Eq. (2.63) we obtain 1TDVP effective Hamiltonians which allow bond dimensions to increase:

$$\hat{H}_{\text{eff}}^j(\bar{D}_{j-1}, \bar{D}_j) = \begin{array}{c} \begin{array}{c} D_{j-1} \\ | \\ F_L^{j-1} \end{array} \text{---} \begin{array}{c} H^j \\ | \\ \bar{D}_j \end{array} \text{---} \begin{array}{c} D_j \\ | \\ F_R^{j+1} \end{array} \\ \bar{D}_{j-1} \quad \bar{D}_j \end{array}; \quad \hat{K}_{\text{eff}}^j(\bar{D}_j) = \begin{array}{c} \begin{array}{c} D_j \\ | \\ F_L^j \end{array} \text{---} \begin{array}{c} D_j \\ | \\ F_R^{j+1} \end{array} \\ \bar{D}_j \quad \bar{D}_j \end{array}, \quad (5.8)$$

where the left and right environment tensors are now given by:

$$F_L^j := \begin{array}{c} \dots \text{---} \begin{array}{c} \text{R} \\ | \\ \text{R} \\ | \\ \text{R} \end{array} \text{---} \begin{array}{c} L^j \\ | \\ H^j \\ | \\ L^j \end{array} \text{---} \dots \\ F_L^j \\ \dots \text{---} \begin{array}{c} \text{R} \\ | \\ \text{R} \\ | \\ \text{R} \end{array} \text{---} \dots \end{array}; \quad F_R^j := \begin{array}{c} \dots \text{---} \begin{array}{c} \text{R}^j \\ | \\ H^j \\ | \\ \text{R}^j \end{array} \text{---} \dots \\ F_R^j \\ \dots \text{---} \begin{array}{c} \text{R}^j \\ | \\ \text{R}^j \\ | \\ \text{R}^j \end{array} \text{---} \dots \end{array}. \quad (5.9)$$

Replacing the effective Hamiltonians of 1TDVP with $\hat{H}_{\text{eff}}^j(\bar{D}_{j-1}, \bar{D}_j)$ and $\hat{K}_{\text{eff}}^j(\bar{D}_j)$ yields an algorithm which is almost identical to 1TDVP but which gives us the control to increase the bond dimensions as, when, and where we choose. However, the basic problem of how to choose appropriate bond dimensions, providing the right balance between speed and accuracy, still remains.

5.1.3 Projection Error

Ideally, bond dimensions would be chosen so as to guarantee that the projection error $\epsilon_{\mathcal{P}}$ does not exceed a certain acceptable value: $\epsilon_{\mathcal{P}} \leq \epsilon'_{\mathcal{P}}$. The projection error arises from the fact that the true time evolution vector $\hat{H}|\psi\rangle$ differs from the projected one $\hat{\mathcal{P}}_{T_{|\psi\rangle}, \mathcal{M}} \hat{H}|\psi\rangle$ by a residue $|\phi\rangle$

$$|\phi\rangle := \hat{H}|\psi\rangle - \hat{\mathcal{P}}_{T_{|\psi\rangle}, \mathcal{M}}|\psi\rangle. \quad (5.10)$$

We can thus define the projection error as being the norm of this residue

$$\epsilon_{\mathcal{P}}(\bar{\mathbf{D}}) := \langle\phi|\phi\rangle = \langle\psi|\hat{H}^2|\psi\rangle - \langle\psi|\hat{H}\hat{\mathcal{P}}_{T_{|\psi'\rangle}, \mathcal{M}}(\bar{\mathbf{D}})\hat{H}|\psi\rangle, \quad (5.11)$$

where we have inserted the bond dimension dependent projectors to obtain the projection error as a function of $\bar{\mathbf{D}}$. In principle, one could evaluate the function $\epsilon_{\mathcal{P}}(\bar{\mathbf{D}})$ in advance of each 1TDVP sweep and find the smallest set of bond dimensions \mathbf{D}' such that $\epsilon_{\mathcal{P}}(\mathbf{D}') \leq \epsilon'_{\mathcal{P}}$. Doing so however would require evaluating the MPO expectation value $\langle\psi|\hat{H}^2|\psi\rangle$ which, for large bond dimensions can be prohibitively expensive, even when 1TDVP and single site observable calculations are still feasible [141]. However, the full evaluation of $\epsilon_{\mathcal{P}}(\bar{\mathbf{D}})$ may not always be necessary. For example, when the Hamiltonian is nearest-neighbour, i.e. only contains terms which act on neighbouring pairs of sites, it is possible to reduce the projection error to zero by choosing the maximum values for all bond dimensions in $|\psi'\rangle$. This is because, $\hat{\mathcal{P}}_{T_{|\psi'\rangle}, \mathcal{M}}(\bar{\mathbf{D}}_{\text{max}})$, like the two-site projector $\hat{\mathcal{P}}_{T_{|\psi(t)\rangle}, \mathcal{M}}^{[2]}$, projects onto a manifold that contains the full space of two-site variations about the wave-function $|\psi\rangle$. Indeed, performing 1TDVP with the projector $\hat{\mathcal{P}}_{T_{|\psi'\rangle}, \mathcal{M}}(\bar{\mathbf{D}}_{\text{max}})$ is very similar to performing 2TDVP without any truncation, and one can easily see that the bond dimension growth is the same in both cases.

Given then that $\epsilon_{\mathcal{P}}(\bar{\mathbf{D}}_{\text{max}}) = 0$, for a nearest-neighbour \hat{H} we have

$$\langle\psi|\hat{H}^2|\psi\rangle = \langle\psi|\hat{H}\hat{\mathcal{P}}_{T_{|\psi'\rangle}, \mathcal{M}}(\bar{\mathbf{D}}_{\text{max}})\hat{H}|\psi\rangle. \quad (5.12)$$

On the other hand, if the Hamiltonian is not nearest-neighbour the above expression will only be approximately true. This statement is completely equivalent to the theorem from DMRG which states that the full variance¹ is equal to the so called 2-site variance for a nearest-neighbour Hamiltonian and is an approximation when longer-range interactions are involved [141]. In general, we know that the n -site variance will be exact when the Hamiltonian only contains terms which couple up to n neighbouring sites. We could

¹The full variance is defined as $\langle\psi|\hat{H}^2|\psi\rangle - \langle\psi|\hat{H}|\psi\rangle^2$

follow in this spirit and define projectors based on the MPS $|\psi''\rangle$ in which we expand the sub-spaces of two consecutive sites. In this case we would have projectors

$$\hat{P}_j^{L,|\psi''\rangle}(\bar{D}_j) := \begin{array}{c} \dots \text{---} L \text{---} D_{j-2} \text{---} L \text{---} d_{j-1} D_{j-2} \text{---} L \text{---} \bar{D}_j \\ \begin{array}{ccc} i'_{j-2} & i'_{j-1} & i'_j \\ | & | & | \\ & d_{j-1} & d_j \end{array} \\ \dots \text{---} L \text{---} D_{j-2} \text{---} L \text{---} d_{j-1} D_{j-2} \text{---} L \text{---} \bar{D}_j \\ \begin{array}{ccc} i_{j-2} & i_{j-1} & i_j \\ | & | & | \\ & d_{j-1} & d_j \end{array} \end{array} \quad (5.13)$$

where now $D_j \leq \bar{D}_j \leq d_j d_{j-1} D_{j-2}$, and similarly for $\hat{P}_j^{R,|\psi''\rangle}(\bar{D}_j)$. Then, by choosing the maximum values for all bond dimensions we could eliminate the projection error for any \hat{H} containing terms coupling *three* neighbouring sites.

Given that the Hamiltonians we are principally interested in are essentially nearest-neighbour, we will assume that Eq. (5.12) is either exact or a good approximation. Under this assumption, the only quantity we need calculate in order to determine the projection error is $\langle \psi | \hat{H} \hat{\mathcal{P}}_{T_{|\psi\rangle}, \mathcal{M}}(\bar{\mathbf{D}}) \hat{H} | \psi \rangle$. If we know this quantity for every $\bar{\mathbf{D}}$, including $\bar{\mathbf{D}}_{\max}$, we also know $\epsilon_{\mathcal{P}}(\bar{\mathbf{D}})$ for every $\bar{\mathbf{D}}$. Inserting the decomposition of the projector, we have

$$f(\bar{\mathbf{D}}) := \langle \psi | \hat{H} \hat{\mathcal{P}}_{T_{|\psi\rangle}, \mathcal{M}}(\bar{\mathbf{D}}) \hat{H} | \psi \rangle \quad (5.14)$$

$$= \sum_{j=1}^N \|\hat{H}_{\text{eff}}^j(\bar{D}_{j-1}, \bar{D}_j) A_C^j\|^2 - \sum_{j=1}^{N-1} \|\hat{K}_{\text{eff}}^j(\bar{D}_j) C^j\|^2 \quad (5.15)$$

$$= \sum_{j=1}^N \left\| \begin{array}{c} \text{---} F_L^{j-1} \text{---} A_C^j \text{---} F_R^{j+1} \text{---} \\ | \quad | \\ \bar{D}_{j-1} \quad \bar{D}_j \\ | \quad | \\ \text{---} H^j \text{---} \end{array} \right\|^2 - \sum_{j=1}^{N-1} \left\| \begin{array}{c} \text{---} F_L^j \text{---} C^j \text{---} F_R^{j+1} \text{---} \\ | \quad | \\ \bar{D}_j \quad \bar{D}_j \\ | \quad | \end{array} \right\|^2 \quad (5.16)$$

where the tensors A_C^j and C^j refer to the orthogonality centres of the MPS $|\psi\rangle$. Calculating $f(\bar{\mathbf{D}})$ requires performing an additional left-to-right QR sweep in advance of the time evolution step in order to calculate the tensors A_C^j , C^j and F_L^j ; the tensors F_R^j do not need to be calculated as they will already be available from the previous time evolution step (except of course on the initial step). Following this, the $2N - 1$ tensors $\hat{H}_{\text{eff}}^j(\bar{D}_{j-1}, \bar{D}_j) A_C^j$ and $\hat{K}_{\text{eff}}^j(\bar{D}_j) C^j$ can be computed. If one computes these tensors for the maximum bond dimensions $\bar{\mathbf{D}}_{\max}$, $f(\bar{\mathbf{D}})$ may be evaluated for any $\bar{\mathbf{D}}$ simply by truncating the expanded bonds to the desired values of D and taking norms - a step

which requires negligible computational effort. Once we have $f(\bar{\mathbf{D}})$, one can find the set of bond dimensions \mathbf{D}' which are the smallest whilst ensuring the projection error lies within the accepted tolerance: $\epsilon_{\mathcal{P}}(\mathbf{D}') \leq \epsilon'_{\mathcal{P}}$. Then, applying a left-to-right 1TDVP sweep using the expanded effective Hamiltonians of Eq. (5.8) constructed from the appropriately truncated F_{R}^j tensors, will produce an MPS with these new bond dimensions. The subsequent right-to-left 1TDVP sweep completes the time evolution step and returns the MPS to its original, right canonical gauge, without producing a further change in the bond dimensions.

In order for the A1TDVP algorithm to be useful, the bond update step must be relatively cheap; ideally, one should not spend more time deciding on what the next bond dimensions ought to be, than one spends on actually performing the time evolution. The cost of the bond update step can be broken down as follows. First, there is the cost of the QR sweep and the tensor contractions required to compute the tensors F_{L}^j . There is not much scope for parallelism in this step, however, its cost can be mitigated by using the A_{C}^j tensors as a shortcut to computing observables along the chain. Second, there is the cost of the tensor contractions required to compute $\hat{H}_{\text{eff}}^j(\bar{D}_{j-1}, \bar{D}_j)A_{\text{C}}^j$ and $\hat{K}_{\text{eff}}^j(\bar{D}_j)C^j$. Once all tensors A_{C}^j , C^j , F_{L}^j and F_{R}^j are available, these $2N - 1$ contractions can be performed in parallel. In comparing the cost of the bond update step to 1TDVP, we note that by far the most expensive operation in 1TDVP is the computation of the exponentiated effective Hamiltonians, which, under the Krylov method, involves dozens of applications of the effective Hamiltonians. In the bond update step, however, each effective Hamiltonian only has to be applied once, suggesting that the bond update step should not take longer than a 1TDVP step. On the other hand, in taking $\bar{\mathbf{D}} = \bar{\mathbf{D}}_{\text{max}}$, the size of the F tensors increases by a factor of d . This is a problem as it means that computing $f(\bar{\mathbf{D}})$ will have the same complexity as 2TDVP - precisely what we are aiming to avoid.

5.1.4 Convergence criterion

So that A1TDVP retain the same complexity as 1TDVP, instead of calculating f for all $\bar{\mathbf{D}}$ up to $\bar{\mathbf{D}}_{\text{max}}$ to obtain the full projection error, we do something cheaper, which is to look at how f changes as the bond dimensions are increased. Assuming that each additional state that one adds has a smaller effect on the projection error, we should be able to define a convergence measure that will allow us to determine appropriate values for $\bar{\mathbf{D}}$. We find that choosing bond dimensions to satisfy the requirement

$$\frac{1}{f_j(\bar{D}_j)} \frac{\partial f}{\partial \bar{D}_j} \leq p, \quad (5.17)$$

where p defines a precision and f_j is the part of the projection error that depends on \bar{D}_j , works well in economising resources whilst providing fast convergence. The presence of the factor of $f_j(\bar{D}_j)$ in the denominator makes the convergence criterion independent of the scale of f . This is important because the magnitude of $f_j(\bar{D}_j)$ has no meaning on its own as it only represents half of the expression for the projection error (Eq. (5.11)). A

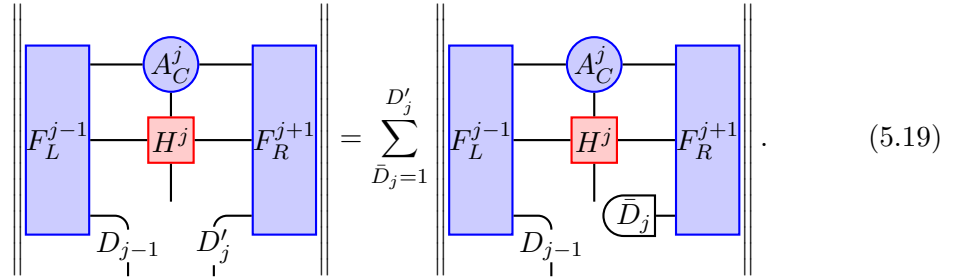
smaller value of p will lead to faster growing bond dimensions and thus a more accurate simulation. The dependence of the projection error on the single bond dimension \bar{D}_j is contained in three of the terms of $f(\bar{\mathbf{D}})$ and thus we have

$$f_j(\bar{D}_j) := \|\hat{H}_{\text{eff}}^j(D_{j-1}, \bar{D}_j)A_C^j\|^2 - \|\hat{K}_{\text{eff}}^j(\bar{D}_j)C^j\|^2 + \|\hat{H}_{\text{eff}}^{j+1}(\bar{D}_j, D_{j+1})A_C^{j+1}\|^2. \quad (5.18)$$

In only considering the dependence of the projection error on each bond dimension individually, we ignore any possible co-dependence of the bond dimensions, which may arise from the \hat{H}_{eff}^j terms in Eq. (5.15). New values, D'_j for each bond dimension can be determined by evaluating the left hand side of (5.17) at incrementally increasing values of \bar{D}_j for each site j until the inequality is satisfied. Since each bond dimension is determined independently of the others, these operations may be done in parallel, leading to a speed-up of up to $N - 1$ times (the individual terms in Eq. (5.18) may also be computed in parallel). During the course of this bond determination step, the tensors F_R^j with the new bond dimensions will be constructed; these should be saved as they will be required for the subsequent left-to-right 1TDVP sweep during which the MPS will take on the new bond dimensions.

If ever we find that the inequality (5.17) is satisfied for $\bar{D}_j < D_j$, i.e. for a bond dimension smaller than its current value, we do not decrease the MPS bond dimension but instead leave it unchanged: $D'_j = D_j$. Indeed, we wish to emphasise that the effective Hamiltonians used in A1TDVP do not provide a means of *decreasing* the MPS bond dimensions, only increasing them.

Defining the new bond dimensions using the inequality (5.17) removes the need to evaluate $f(\bar{\mathbf{D}})$ at $\bar{\mathbf{D}} = \bar{\mathbf{D}}_{\text{max}}$. Instead of calculating the tensors $\hat{H}_{\text{eff}}^j(\bar{D}_{j-1}, \bar{D}_j)A_C^j$ and $\hat{K}_{\text{eff}}^j(\bar{D}_j)C^j$ at the maximum values of \bar{D}_j and then truncating to obtain f at different values of \bar{D}_j , one can evaluate them ‘row-by-row’ such that they are only constructed up to the values of \bar{D}_j which will eventually become the new bond dimensions for the MPS. To illustrate what we mean by ‘row-by-row’ we note that



$$\left(\begin{array}{c} \text{---} \\ \left| \begin{array}{c} F_L^{j-1} \text{---} \text{---} A_C^j \text{---} \text{---} F_R^{j+1} \\ | \quad | \quad | \\ D_{j-1} \quad H^j \quad D'_j \end{array} \right. \\ \text{---} \end{array} \right) = \sum_{\bar{D}_j=1}^{D'_j} \left(\begin{array}{c} \text{---} \\ \left| \begin{array}{c} F_L^{j-1} \text{---} \text{---} A_C^j \text{---} \text{---} F_R^{j+1} \\ | \quad | \quad | \\ D_{j-1} \quad H^j \quad \text{---} \\ \quad \quad \quad \text{---} \bar{D}_j \end{array} \right. \\ \text{---} \end{array} \right). \quad (5.19)$$

On the right hand side of Eq. (5.19) the white, semi-circular tensor is used to select the ‘slice’ of F_R^{j+1} for which the index takes the value \bar{D}_j . One can thus evaluate the right hand side of (5.17) at incremental values of \bar{D}_j by performing tensor contractions of the form above until the convergence threshold is satisfied. In this way we solve the issue of ‘over-stepping’ present in 2TDVP, in which one has to spend time in computing an object which is partially discarded later on. Crucially, this ‘row-by-row’ evaluation ensures that the bond update step will scale no worse in any of the MPS dimensions

than a 1TDVP sweep and will in fact, because of the absence of a need to exponentiate any linear maps, be many times faster.

5.1.5 Summary

We can summarise the steps of A1TDVP as follows. First, ahead of any time evolution, one computes new bond dimensions of the MPS using the convergence criterion (5.17). This step involves a QR sweep of the MPS followed by a number of tensor contractions which are highly parallelisable. Then, 1TDVP is performed, using projectors with subspaces expanded accordingly, to produce an MPS evolved by one time step with the new, increased, bond dimensions.

We expect A1TDVP to be faster than 1TDVP due to the acceleration gained from having more optimised bond dimensions; the bond update step is cheap and so its cost should not normally outweigh this advantage. We should also expect A1TDVP to be significantly faster than 2TDVP (at least when the local physical dimension is relatively large), due to the improved scaling with d . Another reason why A1TDVP should be more efficient than 2TDVP is the fact that the much cheaper QR decomposition may be used instead of the SVD.

In practice, we find A1TDVP to be a highly advantageous method which, as we shall demonstrate below, offers a significant speed-up compared to both 1TDVP and 2TDVP. Indeed, a number of the results presented in this thesis were obtained with A1TDVP. In previous chapters, it was not deemed necessary to state when a particular result was obtained with A1TDVP, since, provided the result is converged, the difference lies purely in the computational efficiency of the simulation rather than in the quality of the dynamics. The A1TDVP method is implemented in the MPSDynamics.jl package [92].

5.2 Numerical Verification

We tested our bond adaptive TDVP against the unbiased two-bath spin-boson model, which was introduced in Sec. 3.4. This model provides a good testing ground for A1TDVP as the presence of the two baths gives the model a spatial inhomogeneity. The two baths will have different requirements in terms of bond dimensions, and any bond adaptive algorithm should be sensitive to this, allocating the most resources where they are the most necessary.

The Hamiltonian is exactly that of Eq. (3.43). For convenience, we repeat it here:

$$\hat{H} = -\frac{\Delta}{2}\sigma_x + \frac{\sigma_z}{2} \otimes \sum_{\alpha \in [\text{h,c}]} \sum_k g_{\alpha,k} (b_{\alpha,k}^\dagger + b_{\alpha,k}) + \sum_{\alpha \in [\text{h,c}]} \sum_k \omega_{\alpha,k} b_{\alpha,k}^\dagger b_{\alpha,k}. \quad (5.20)$$

As before, we take identical, Ohmic spectral densities for both baths $J_c(\omega) = J_h(\omega) = 2\alpha\omega\theta(\omega - \omega_c)$, and set up a temperature gradient, with $\omega_c\beta_c = 100$ for the cold bath and $\omega_c\beta_h = 1$ for the hot bath. We choose a non-perturbative coupling strength of $\alpha = 0.2$, and take as our initial condition $|\uparrow_x\rangle$. It was found that a local Hilbert space dimension of $d = 15$ for all chain oscillators present in the simulation, was sufficient to give well

converged results. The chains for both baths were truncated so as to contain 40 sites each. The structure of the MPS is as shown in Fig. 3.13 with the TLS on site 41, between the two baths.

We ran A1TDVP on this model for several values of the precision p and compared the resulting dynamics and bond dimensions against those obtained using 2TDVP, also for different precisions. We also calculated the dynamics with 1TDVP at a very large bond dimension ($D_{\max} = 120$) to provide a highly converged, benchmark result for evaluating the convergence of the bond adaptive simulations. As is common in bond adaptive methods, to avoid exploding memory usage, we set an upper bound D_{\lim} for the bond dimensions. We chose $D_{\lim} = 120$ for both the A1TDVP and 2TDVP simulations.

Figure 5.1 shows the observable $\langle \sigma_x \rangle$ obtained using A1TDVP at four different precisions. We find that a precision of $p = 10^{-4}$ gives well converged results up to a time of $\omega_c t = 25$. In Fig. 5.2 we compare the convergence of A1TDVP against that of 2TDVP and find that 2TDVP gives a similarly well converged result at a precision of $p = 10^{-4}$. It must be pointed out that, although we use the same symbol p to denote the precision of both A1TDVP and 2TDVP, this parameter is defined differently for each method: when referring to 2TDVP, p is the threshold below which singular values are discarded following the SVDs, while for A1TDVP, p is the parameter appearing in the inequality (5.17). The fact that convergence is obtained at roughly the same value of p for the two methods is purely a coincidence.

In Fig. 5.3 we plot the MPS bond dimensions at three snapshots in time for the different precisions of A1TDVP. We see that the bond dimensions grow in a way that mirrors the light-cone structure of the dynamics of a system coupled to initially unoccupied baths (cf. Sec. 2.4.1, Fig. 2.3). From this, it is clear how A1TDVP can be hugely advantageous for the class of OQS problems that we consider in this thesis: any chain mode outside of the light-cone will not participate in the dynamics and so may remain with trivial bond dimensions. Also clear from Fig. 5.3 is the fact that the bond dimensions are skewed towards the hot bath on the right of the grey dashed line. This is in line with the discussion of Sec. 3.5.1, in which we showed that, under the T-TEDOPA method, hotter baths will lead to more highly occupied chain modes and hence more entanglement. This illustrates another important point about A1TDVP and bond adaptive time evolution methods in general, which is that they automatically capture the spatial inhomogeneities of the model. Under 1TDVP, non-uniformity makes determining optimal bond dimensions exponentially more complex such that it is often easier to just use a fixed bond dimension for all sites, which is highly non-optimal.

Also shown in Fig. 5.3 are the bond dimensions given by 2TDVP at the precision of $p = 10^{-4}$ which was shown to give a similar quality of result as A1TDVP for $p = 10^{-4}$. Comparing the bond dimensions for these two cases, we see that they follow a similar distribution, which is encouraging for A1TDVP, although the bond dimensions for A1TDVP tend to be slightly larger.

All simulations were performed on nodes consisting of two 12-core Intel Xeon Haswell (E5-2670v3) processors. The total run times for the three methods are given in Tab. 5.1. The speed-up achieved by A1TDVP is quite striking, being almost 10 times faster than

1TDVP and 30 times faster than 2TDVP. Of course, the comparison between 1TDVP and A1TDVP would be less favourable to A1TDVP had we chosen the chains to be shorter; by the end of the simulation at $\omega_c t = 25$ the perturbation has travelled about 30 sites into the hot bath's chain and about 20 sites into the cold bath's chain, and so we could have truncated them more severely without affecting the results. However, such optimisations are only possible with hindsight, as we do not know how the light-cone will spread before we run the simulationⁱⁱ. The efficiency of A1TDVP on the other hand is relatively insensitive to the chosen chain length, since it takes very little time to update MPS sites for which the bond dimensions are trivial.

Method	Run Time (mins)
1TDVP ($D_{\max} = 120$)	338
2TDVP ($p = 10^{-4}, D_{\lim} = 120$)	1054
A1TDVP ($p = 10^{-4}, D_{\lim} = 120$)	35 ⁱⁱⁱ

Table 5.1: Run times for converged simulations under the three methods considered.

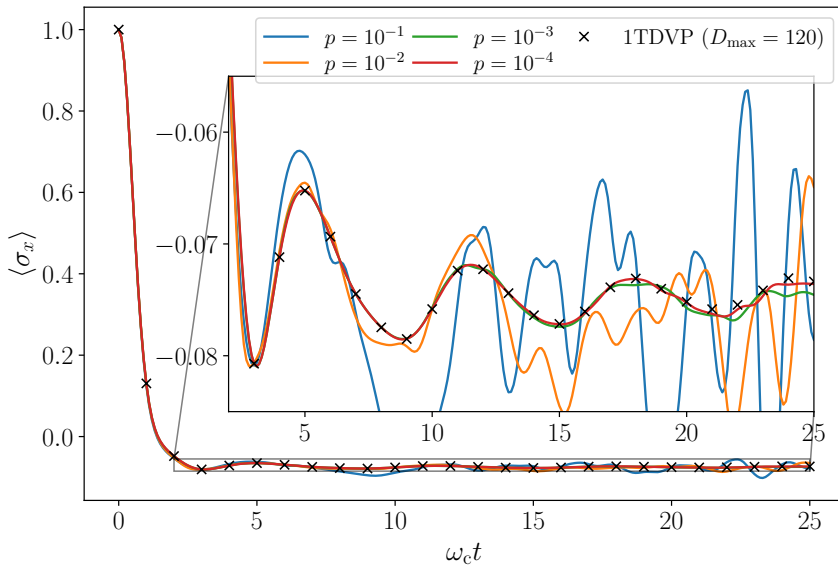


Figure 5.1: Dynamics of $\langle \sigma_x \rangle$ obtained using A1TDVP. Convergence up to $\omega_c t = 25$, measured with respect to a 1TDVP benchmark, is achieved at a precision of $p = 10^{-4}$.

ⁱⁱThis is true in general although for the simple case of a nearest-neighbour hopping chain one can quite easily estimate how fast the light-cone will spread.

ⁱⁱⁱThis time does not include the time required for the bond update step, which we were not able to obtain. However, since the bond update step is expected to take a small fraction of the time required for TDVP, this will not affect our conclusions.

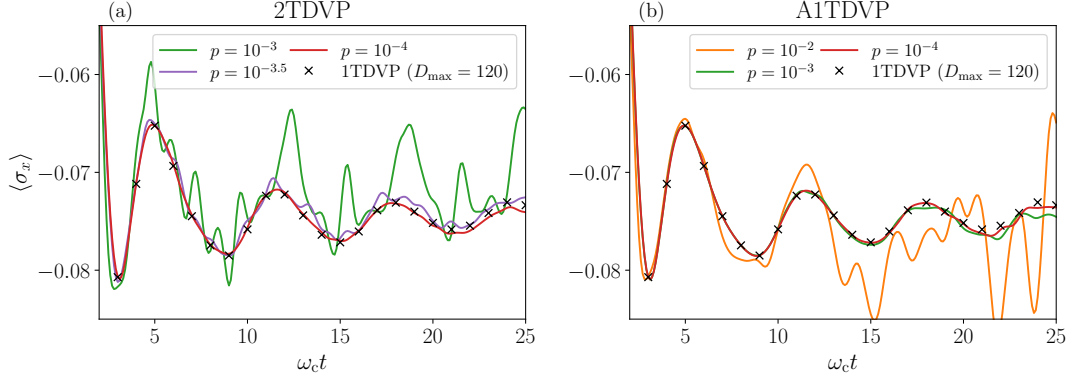


Figure 5.2: Comparing the convergence of 2TDVP (panel ‘a’) and A1TDVP (panel ‘b’). Convergence up to $\omega_c t = 25$ is achieved at a precision of $p = 10^{-4}$ for both 2TDVP and A1TDVP.

5.3 Optimising the Sub-space Expansion

Expanding the sub-spaces of the one-site projector using the Q_2 matrix is the cheapest possible means of doing so, since we get Q_2 for free as the output of the QR decomposition. As illustrated in Fig. 2.1 and discussed in Sec. 2.2.2, when the MPS is rank deficient, evolution under 1TDVP is gauge dependent. In the present case, this means that the choice of states used for sub-space expansion will affect the evolution, and thus there ought to exist some optimal expansion matrix which, for a given bond dimension growth, will minimise the projection error. This kind of problem has also been studied in the context of ML-MCTDH [142, 143].

There is no reason why the Q_2 matrix should be in any way optimised for the job of enriching the state space; indeed Q_2 was obtained using only information contained in the MPS at the current time step $|\psi(t)\rangle$, whereas, the projection error (5.11) also depends on the action of the Hamiltonian on $|\psi(t)\rangle$; thus, any optimised expansion matrix must be determined by taking this information into account. An optimised sub-space expansion could lead to slower bond dimension growth and thus a more efficient simulation. For example, we observed from Fig. 5.3 that A1TDVP leads to slightly larger bond dimensions than does 2TDVP for the same quality of result; this situation could perhaps be improved if sub-spaces were optimised.

The problem of optimising the sub-space expansion can be stated as follows. For simplicity we will assume that all current MPS bond dimensions are D and all physical dimensions are d . Suppose we want to increase the dimension of the bond linking sites j and $j + 1$ by an amount D^+ , in an optimal way, that is, such that the projection error is minimised. Then we must find the isometry matrix \mathbf{O}_j with dimensions $(d - 1)D \times D^+$, given by

$$\mathbf{O}_j = \arg \max_{\mathbf{O}'_j} \left\{ \left[\begin{array}{c} \left(\begin{array}{c} \text{---} F_L^{j-1} \text{---} A_C^j \text{---} F_R^{j+1} \text{---} \\ \text{---} H^j \text{---} \\ \text{---} \end{array} \right)^2 \\ \text{---} D \text{---} \\ \text{---} D' \text{---} \end{array} \right] - \left[\begin{array}{c} \left(\begin{array}{c} \text{---} F_L^j \text{---} C^j \text{---} F_R^{j+1} \text{---} \\ \text{---} \\ \text{---} \end{array} \right)^2 \\ \text{---} D' \text{---} \\ \text{---} D' \text{---} \end{array} \right] \right\}, \quad (5.21)$$

where

$$\text{---} dD \text{---} \blacktriangleright \text{---} D' \text{---} = \begin{pmatrix} \mathbb{1}_{D \times D} & 0 \\ 0 & \mathbf{O}'_j \end{pmatrix}. \quad (5.22)$$

and where $D' = D + D^+$ is the new value of the bond dimension. In the above, the tensor F_R^{j+1} is as defined in Eq. (5.9); the tensors F_L^{j-1} and F_L^j are also defined in Eq. (5.9) but have had their lower legs truncated to D and D' respectively.

The matrix \mathbf{O}_j finds the D^+ most relevant linear combinations of the $(d-1)D$ Q_2 states of the expanded, right normalised MPS site R_{j+1} . This optimisation is based on the assumption made in Sec. 5.1.3 that the Hamiltonian is principally nearest-neighbour. Applying the isometry $\text{---} \blacktriangleright \text{---}$, with $\mathbf{O}'_j = \mathbf{O}_j$, to R_{j+1} yields an MPS site whose set of output states have been optimally expanded for the next time evolution step:

$$\text{---} D' \text{---} \blacktriangleright \text{---} dD \text{---} \begin{array}{c} j+1 \\ \text{---} R \text{---} \\ d \\ \text{---} \end{array} \text{---} D \text{---}. \quad (5.23)$$

In Fig. 5.4(a) we plot the function $f_j(\bar{D}_j)$, which forms the basis of our bond update scheme, for three neighbouring sites, at a single time step of the converged, unbiased two-bath SBM simulation ($p = 10^{-4}$). The three values of j shown in the figure: 40, 41 and 42, correspond respectively to the bond between the first site of the cold bath and the TLS, the bond between the TLS and the first site of the hot bath, and the bond between the first and second sites of the hot bath. One can see how the convergence criterion (5.17) is effective in selecting appropriate bond dimensions: as the bond dimension is increased, the curves tend to plateau; once the plateaux are reached, increasing the bond dimension further will have a negligible effect on the projection error; the criterion (5.17) is able to detect the presence of these plateaux. Also shown in Fig. 5.4(a) are the current values of the bond dimensions D_{40} , D_{41} , and D_{42} , and their updated values (denoted with a prime) if they differ. For this particular time step, the two bond dimensions D_{40} and D_{42} remain constant, while D_{41} increases. We note that the curve of f_{42} has been curtailed due to the global bond dimension limit D_{lim} .

In the inset (Fig. 5.4(b)), we zoom in on the section of f_{40} for which \bar{D}_{40} lies above the current value of the bond dimension D_{40} . This is the part of f_{40} which tells us what the influence of increasing the bond dimension above its current value has on the projection error; each point corresponds to the expansion of the local sub-space by adding one state from Q_2 . While the trend of this section of the curve is similar to the global trend of f_{40} ; that is, the gradient decreases with increasing bond dimension until a plateau is reached; it is also clear that the gradient does not diminish monotonically and that there are several ‘shelves’ in the curve before the one attains the global maximum. These shelves are evidence of the non-optimality of the Q_2 states for expanding the local sub-space; with an optimal sub-space expansion, as obtained via the solution of Eq. (5.21), each additional state that one adds should have a smaller effect upon the projection error.

In Fig. 5.4(c) we re-plot this section of the curve using different sub-space expansions, obtained via different choices for the isometry \mathbf{O}'_{40} . First, we compare the expansion based on the original Q_2 states ($\mathbf{O}'_{40} = \mathbb{1}_{(d-1)D \times D^+}$) with two expansions for which \mathbf{O}'_{40} is a random isometry. We see that these three curves are broadly similar, showing that the Q_2 states are no better for sub-space expansion than random states.

Next, we compare against a *partially* optimised sub-space expansion. By partially optimised we mean that we solve Eq. (5.21) ignoring the second term in the bracket; that is, the isometry is given by

$$\mathbf{O}_j^{\text{partial}} = \arg \max_{\mathbf{O}'_j} \left\{ \left(\begin{array}{c} \left[\begin{array}{c} F_L^{j-1} \\ H^j \\ F_R^{j+1} \end{array} \right] \begin{array}{c} A_C^j \\ H^j \end{array} \left[\begin{array}{c} F_R^{j+1} \\ H^j \\ F_L^{j-1} \end{array} \right] \\ \left[\begin{array}{c} D \\ D' \end{array} \right] \end{array} \right)^2 \right\}, \quad (5.24)$$

with $j = 40$, where \blacktriangle is again given by Eq. (5.22). Considering only this first term means that the solution can be obtained via a single SVD, allowing us to demonstrate the effect of sub-space optimisation, without over-complication. As can be seen from Fig. 5.4(c), this partially optimised sub-space expansion leads to an f_{40} curve which increases more sharply and plateaus sooner than the Q_2 (or random) sub-space expansion. Also clear is that, while the gradient of f_{40} is still non-monotonic, the shelves are much less horizontal for the partially optimised sub-space than for the non-optimised ones. Moreover, the difference between the partially optimised curve and the non-optimised curves is much greater than the variation amongst the non-optimised curves themselves, suggesting that these features are genuine consequences of the optimisation step and not down to chance. Incorporating this optimisation step into the A1TDVP algorithm would thus lead to more slowly growing bond dimensions and therefore a more efficient

simulation.

Of course, any potential speed-up that could be gained by having smaller bond dimensions should be balanced against the computational cost of obtaining the improved set of expansion states. Indeed, optimising over the full set of dD states as we do above would have a complexity similar to 2TDVP and so may become unfavourable for large d . There are ways in which this cost could potentially be mitigated. For example, instead of solving Eq. (5.24) with a full SVD to obtain the isometry $\mathbf{O}_j^{\text{partial}}$ up to the maximum value of D^+ , one could ask for just the first few, most significant rows, which may be obtained at a lower computational cost via the Krylov method. One could also aim for a limited optimisation by truncating the basis of dD input states to a more manageable number.

Since A1TDVP, regardless of which set of states are used for sub-space expansion, retains the desirable properties of 1TDVP, namely its unitarity and the fact that it gives no error in conserved quantities, for certain problems, when the scaling with d is less important, it may even be possible that a full optimisation of the sub-space expansion could be favourable.

5.4 Conclusion

In this chapter we have presented a bond adaptive variant of 1TDVP, which we have demonstrated to be highly advantageous for the OQS problem that we consider in this thesis. The features of the OQS problem that make it particularly well suited to A1TDVP are its light-cone structure and the fact that the scaling in the local physical dimension d is important since it is a convergence parameter. While we have only tested our method in the context of OQS, we also believe that our approach could be readily applied to a broad range of problems in condensed or atomic quantum matter.

The extension of A1TDVP to tree-MPS is straightforward although not currently implemented in the MPSDynamics.jl package. This extension would allow the A1TDVP method to be applied to systems with complex multi-environment interactions, such as Methylene blue as studied in chapter 4, whereupon, the advantages demonstrated here would become even more important, and could be further combined with the ‘entanglement renormalisation’ techniques introduced in Ref. [30].

We have also set out a means of optimising the sub-space expansion of A1TDVP as a way of slowing the bond dimension growth, although there remain open questions as to the best strategy to adopt. While the A1TDVP method is applicable to any Hamiltonian, regardless of the range of the interactions, it is likely that the optimisation procedure as set out above will only be effective when the strongest interactions are to the nearest-neighbours. In the opposite limit, when long-range couplings are of comparable strength, it is likely that the expansion strategy of Yang and White [139] will yield states of higher quality since their method incorporates global information by directly applying the Hamiltonian’s MPO to the MPS.

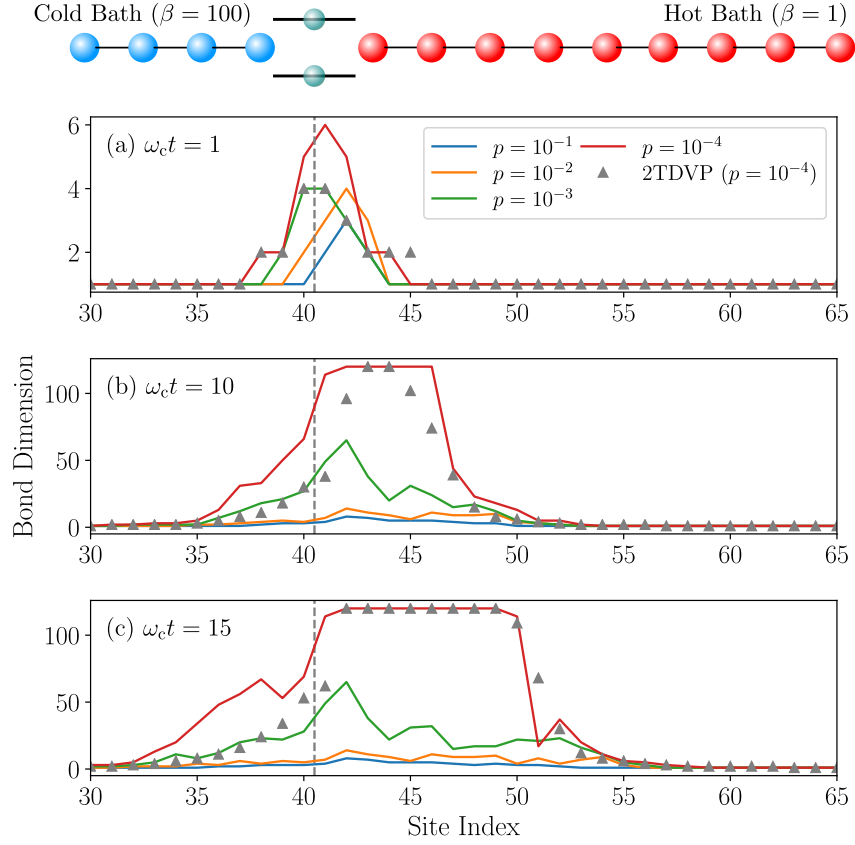


Figure 5.3: MPS bond dimensions for snapshots at times $\omega_c t = 1$ (panel ‘a’), $\omega_c t = 10$ (panel ‘b’), and $\omega_c t = 15$ (panel ‘c’) during A1TDVP simulations at various precisions and the converged 2TDVP simulation at precision $p = 10^{-4}$. The grey dashed line, plotted at x -position 40.5, indicates the position of the TLS; all bond dimensions to the right of this line pertain to the hot bath sites, and all bond dimensions to its left pertain to the cold bath sites.

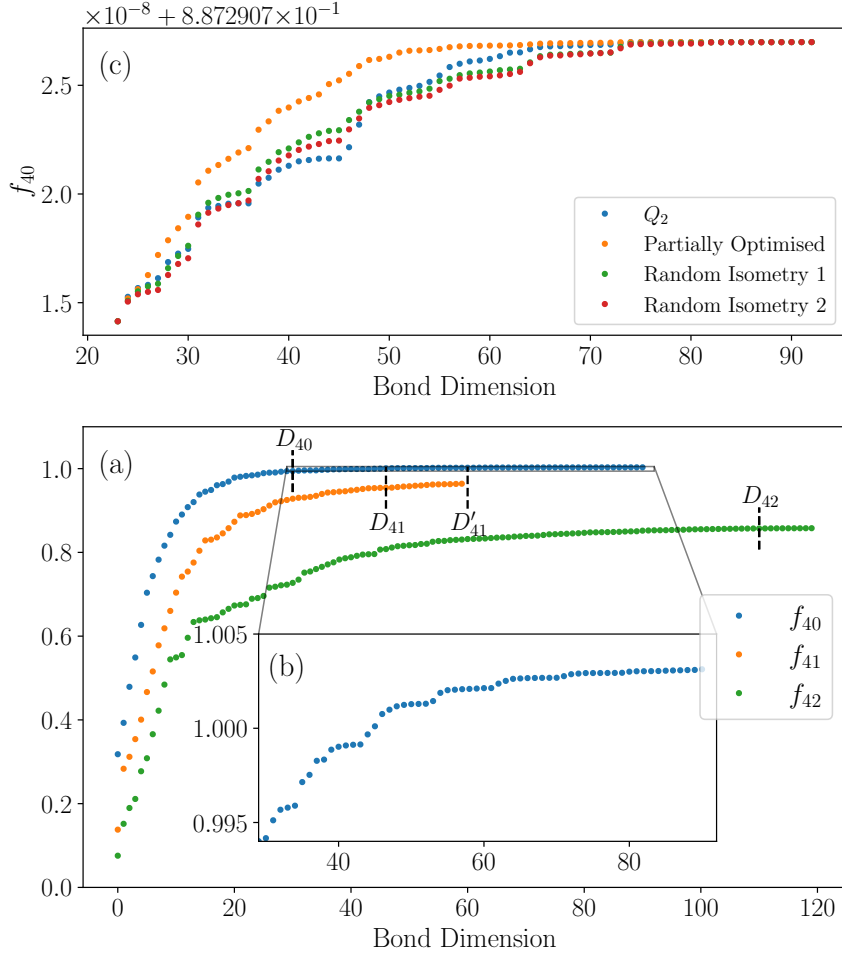


Figure 5.4: (a) Representative plots of the function f_j which is the basis of the bond update step in A1TDVP. The function is shown for three consecutive bonds: 40, 41 and 42, in the converged simulation ($p = 10^{-4}$) of the unbiased two-bath SBM as set out in Sec. 5.2. The functions are shown at the time $\omega_c t = 4$; that is, they are obtained from the MPS $|\psi(4/\omega_c)\rangle$. The bond dimensions, D_{40} , D_{41} , and D_{42} of the MPS $|\psi(4/\omega_c)\rangle$ are indicated, as are the updated bond dimensions D'_{40} , D'_{41} , and D'_{42} where they differ. The inset (b) shows the section of f_{40} for which the bond dimension is increased beyond its current value. This is the part of the curve which is dependent on the choice of states used in the expansion. In panel (c) we re-plot the section of f_{40} shown in inset (b) for different sub-space expansions. These are the expansion based on the bare Q_2 matrix, two expansions based on random states, and a partially optimised expansion.

Chapter 6

Conclusions and Prospects

In this thesis we have presented and applied a powerful methodology for computing numerically exact OQS dynamics at finite temperatures, and in non-perturbative regimes. Our approach, which was inspired by the need to obtain accurate quantum dynamics in complex molecular systems, was based on doing away with the system-environment boundary which is assumed in the traditional approach to OQS, and instead, treating the system+environment as one, using many-body methods. These many-body methods consisted of time evolving MPS/tree-MPS representing the chain-mapped system+environment wave-function, using the time-dependent variational principle.

In chapter 3 this methodology was applied to a number of model systems, allowing us to investigate the physics of electron transfer, quantum heat flow and non-equilibrium steady states. A detailed study of the spin-boson model was also carried out, which has led to the creation of a reference data set, providing the full dynamical map over a large volume of parameter space. In this chapter we also studied the chain dynamics generated under spectral densities resulting from the Tamascelli temperature mapping. We revealed that chain mode occupations grow in an unbounded way at a rate proportional to the temperature, and that this growth was independent of the underlying spectral density. An explanation was provided in the form of a continuous heating cycle, set up by the presence of positive and negative energy modes.

Then, in chapter 4 we combined our approach with *ab initio* electronic structure methods to enable us to calculate the absorption spectrum of Methylene blue in water with unprecedented accuracy, including effects of: correlated fluctuations, non-Condon dynamics, solvent polarisation, and anharmonicity. The resulting investigation revealed the how non-adiabatic dynamics resulting from a conical intersection can lead to intensity borrowing between bright and dark excited states. The approach could be applied to a wide-range of systems, and could be further developed to be able to predict emission and multi-dimensional spectroscopic signals.

Finally, in chapter 5 we developed a variant of the one-site time-dependent variational principle method which allows bond dimensions to be dynamically optimised to capture the growth of entanglement in the quantum state. This variant, which we called A1TDVP, was shown to improve performance by almost 30 times compared with

2TDVP for a particular simulation of the two-bath spin-boson model; and, while evidence of improved efficiency was limited to a specific example, we argued that the benefits of A1TDVP will apply to all chain-mapped open quantum system problems due to their general properties. We believe that time evolution methods based on the TDVP and state space expansion could become very popular in the future because of their unique advantages. The challenge of determining the most optimal basis for subspace expansion remains however, and it is likely that the best strategy will be model dependent.

An additional output of this work is the open-source MPSDynamics.jl package [92], with which all tensor network simulations were performed. The package collects a number of methods, including the A1TDVP, into what is intended to be an easy-to-use interface. There are a number of ways in which MPSDynamics.jl could be improved. These include: implementing A1TDVP for tree-MPS, adding an implementation of the entanglement renormalisation [30] method, integrating the functionality of the ORTHPOL [94] package, and expanding the documentation. Some early work was also carried out showing that our methods can also be applied to interacting fermion problems, so this is another avenue for future projects.

The rapid growth in the field of tensor network methods means that a large number of new algorithms are written every year by many different authors. However, even when code is made openly available, the existence of a large number of separately maintained code bases makes new methods difficult to access. In order to render these innovations easily available to the wider community, there are number of open source projects, such as ITensors [91] and TeNPy [144] which accept contributions from many authors. Thus, future work could look at integrating the new methods into these ecosystems.

Bibliography

- [1] A. Acín et al. “The quantum technologies roadmap: a European community view”. In: *New Journal of Physics* 20.8 (Aug. 15, 2018), p. 080201. ISSN: 1367-2630. DOI: 10.1088/1367-2630/aad1ea (cit. on p. 1).
- [2] C. Monroe, M. G. Raymer, and J. Taylor. “The U.S. National Quantum Initiative: From Act to action”. In: *Science* 364.6439 (May 3, 2019). Publisher: American Association for the Advancement of Science, pp. 440–442. DOI: 10.1126/science.aax0578 (cit. on p. 1).
- [3] M. G. Raymer and C. Monroe. “The US National Quantum Initiative”. In: 4.2 (Feb. 2019). Publisher: IOP Publishing, p. 020504. ISSN: 2058-9565. DOI: 10.1088/2058-9565/ab0441 (cit. on p. 1).
- [4] M. Atatüre et al. “Material platforms for spin-based photonic quantum technologies”. In: *Nature Reviews Materials* 3.5 (May 2018), pp. 38–51. ISSN: 2058-8437. DOI: 10.1038/s41578-018-0008-9 (cit. on p. 1).
- [5] A. W. Chin, S. F. Huelga, and M. B. Plenio. “Coherence and Decoherence in Biological Systems: Principles of Noise Assisted Transport and the Origin of Long-lived Coherences”. In: *Philosophical Transactions of the Royal Society A: Mathematical, Physical and Engineering Sciences* 370.1972 (Aug. 2012), pp. 3638–3657. ISSN: 1364-503X, 1471-2962. DOI: 10.1098/rsta.2011.0224 (cit. on pp. 2, 5).
- [6] C. Schnedermann et al. “A molecular movie of ultrafast singlet fission”. In: *Nature Communications* 10.1 (Dec. 2019), p. 4207. ISSN: 2041-1723. DOI: 10.1038/s41467-019-12220-7 (cit. on pp. 2, 5).
- [7] M. B. Smith and J. Michl. “Singlet Fission”. In: *Chemical Reviews* 110.11 (Nov. 2010), pp. 6891–6936. ISSN: 0009-2665, 1520-6890. DOI: 10.1021/cr1002613 (cit. on p. 2).
- [8] G. S. Engel et al. “Evidence for wavelike energy transfer through quantum coherence in photosynthetic systems”. In: *Nature* 446.7137 (Apr. 2007), pp. 782–786. ISSN: 1476-4687. DOI: 10.1038/nature05678 (cit. on p. 2).
- [9] S. Valleau et al. “Absence of Selection for Quantum Coherence in the FennaMatthewsOlson Complex: A Combined Evolutionary and Excitonic Study”. In: *ACS Central Science* 3.10 (Oct. 2017). Publisher: American Chemical Society, pp. 1086–1095. ISSN: 2374-7943. DOI: 10.1021/acscentsci.7b00269 (cit. on p. 2).

- [10] H.-G. Duan et al. “Disentangling Dynamical Quantum Coherences in the Fenna-Matthews-Olson Complex”. In: *arXiv:2104.01462 [cond-mat]* (Apr. 2021). arXiv: 2104.01462 (cit. on p. 2).
- [11] A. W. Chin et al. “The role of non-equilibrium vibrational structures in electronic coherence and recoherence in pigmentprotein complexes”. In: *Nature Physics* 9.2 (Feb. 2013), pp. 113–118. ISSN: 1745-2481. DOI: 10.1038/nphys2515 (cit. on p. 2).
- [12] H.-P. Breuer and F. Petruccione. *The Theory of Open Quantum Systems*. Oxford: Oxford University Press, 2007. 656 pp. ISBN: 978-0-19-921390-0. DOI: 10.1093/acprof:oso/9780199213900.001.0001 (cit. on pp. 2, 4, 47).
- [13] A. G. Redfield. “Nuclear magnetic resonance saturation and rotary saturation in solids”. In: *Physical Review* 98.6 (1955), p. 1787. DOI: 10.1103/PhysRev.98.1787 (cit. on p. 4).
- [14] K. Blum. *Density matrix theory and applications*. Vol. 64. Springer Science & Business Media, 2012. DOI: 10.1007/978-3-642-20561-3 (cit. on p. 4).
- [15] A. Rivas and S. F. Huelga. *Open quantum systems*. Springer, 2012. DOI: 10.1007/978-3-642-23354-8 (cit. on p. 4).
- [16] U. Weiss. *Quantum Dissipative Systems*. 4th ed. WORLD SCIENTIFIC, Mar. 2012. ISBN: 978-981-4374-91-0 978-981-4374-92-7. DOI: 10.1142/8334 (cit. on pp. 4, 57, 60).
- [17] A. Rivas, S. F. Huelga, and M. B. Plenio. “Quantum non-Markovianity: characterization, quantification and detection”. In: *Reports on Progress in Physics* 77.9 (2014), p. 094001. DOI: 10.1088/0034-4885/77/9/094001 (cit. on p. 4).
- [18] R. Puthumpally-Joseph et al. “Basic mechanisms in the laser control of non-Markovian dynamics”. In: *Physical Review A* 97.3 (Mar. 2018), p. 033411. ISSN: 2469-9926, 2469-9934. DOI: 10.1103/PhysRevA.97.033411 (cit. on pp. 4, 5).
- [19] T. Lacroix et al. “Unveiling non-Markovian spacetime signalling in open quantum systems with long-range tensor network dynamics”. In: *arXiv:2107.11217 [quant-ph]* (July 2021). arXiv: 2107.11217 (cit. on pp. 4, 42).
- [20] I. De Vega and D. Alonso. “Dynamics of non-Markovian open quantum systems”. In: *Reviews of Modern Physics* 89.1 (2017), p. 015001. DOI: 10.1103/RevModPhys.89.015001 (cit. on p. 4).
- [21] Y. Tanimura and R. Kubo. “Time Evolution of a Quantum System in Contact with a Nearly Gaussian-Markoffian Noise Bath”. In: *Journal of the Physical Society of Japan* 58.1 (Jan. 1989). Publisher: The Physical Society of Japan, pp. 101–114. ISSN: 0031-9015. DOI: 10.1143/JPSJ.58.101 (cit. on p. 5).
- [22] A. Ishizaki and Y. Tanimura. “Quantum Dynamics of System Strongly Coupled to Low-Temperature Colored Noise Bath: Reduced Hierarchy Equations Approach”. In: *Journal of the Physical Society of Japan* 74.12 (Dec. 2005). Publisher: The Physical Society of Japan, pp. 3131–3134. ISSN: 0031-9015. DOI: 10.1143/JPSJ.74.3131 (cit. on p. 5).

- [23] Y. Tanimura. “Stochastic Liouville, Langevin, FokkerPlanck, and Master Equation Approaches to Quantum Dissipative Systems”. In: *Journal of the Physical Society of Japan* 75.8 (Aug. 2006). Publisher: The Physical Society of Japan, p. 082001. ISSN: 0031-9015. DOI: 10.1143/JPSJ.75.082001 (cit. on p. 5).
- [24] Y. Tanimura. “Numerically exact approach to open quantum dynamics: The hierarchical equations of motion (HEOM)”. In: *The Journal of Chemical Physics* 153.2 (July 2020). Publisher: American Institute of Physics, p. 020901. ISSN: 0021-9606. DOI: 10.1063/5.0011599 (cit. on p. 5).
- [25] R. P. Feynman and F. L. Vernon. “The theory of a general quantum system interacting with a linear dissipative system”. In: *Annals of Physics* 24 (Oct. 1963), pp. 118–173. ISSN: 0003-4916. DOI: 10.1016/0003-4916(63)90068-X (cit. on p. 5).
- [26] N. Makri and D. E. Makarov. “Tensor propagator for iterative quantum time evolution of reduced density matrices. I. Theory”. In: *The Journal of Chemical Physics* 102.11 (Mar. 1995). Publisher: American Institute of Physics, pp. 4600–4610. ISSN: 0021-9606. DOI: 10.1063/1.469508 (cit. on p. 5).
- [27] N. Makri and D. E. Makarov. “Tensor propagator for iterative quantum time evolution of reduced density matrices. II. Numerical methodology”. In: *The Journal of Chemical Physics* 102.11 (Mar. 1995). Publisher: American Institute of Physics, pp. 4611–4618. ISSN: 0021-9606. DOI: 10.1063/1.469509 (cit. on p. 5).
- [28] A. Strathearn et al. “Efficient non-Markovian quantum dynamics using time-evolving matrix product operators”. In: *Nature Communications* 9.1 (Dec. 2018), p. 3322. ISSN: 2041-1723. DOI: 10.1038/s41467-018-05617-3 (cit. on p. 5).
- [29] G. E. Fux et al. “Efficient Exploration of Hamiltonian Parameter Space for Optimal Control of Non-Markovian Open Quantum Systems”. In: *Physical Review Letters* 126.20 (May 17, 2021), p. 200401. ISSN: 0031-9007, 1079-7114. DOI: 10.1103/PhysRevLett.126.200401 (cit. on p. 5).
- [30] F. A. Y. N. Schröder et al. “Tensor network simulation of multi-environmental open quantum dynamics via machine learning and entanglement renormalisation”. In: *Nature Communications* 10.1 (Dec. 2019), p. 1062. ISSN: 2041-1723. DOI: 10.1038/s41467-019-09039-7 (cit. on pp. 5, 115, 120).
- [31] H. Wang and M. Thoss. “Multilayer formulation of the multiconfiguration time-dependent Hartree theory”. In: *The Journal of Chemical Physics* 119.3 (July 15, 2003). Publisher: American Institute of Physics, pp. 1289–1299. ISSN: 0021-9606. DOI: 10.1063/1.1580111 (cit. on pp. 5, 35).
- [32] R. Orus. “A Practical Introduction to Tensor Networks: Matrix Product States and Projected Entangled Pair States”. In: *Annals of Physics* 349 (Oct. 2014), pp. 117–158. ISSN: 00034916. DOI: 10.1016/j.aop.2014.06.013 (cit. on pp. 8, 9).

- [33] I. V. Oseledets. “Tensor-Train Decomposition”. In: *SIAM Journal on Scientific Computing* 33.5 (Jan. 1, 2011). Publisher: Society for Industrial and Applied Mathematics, pp. 2295–2317. ISSN: 1064-8275. DOI: 10.1137/090752286 (cit. on p. 9).
- [34] W. Hackbusch. *Tensor Spaces and Numerical Tensor Calculus*. Vol. 42. Jan. 2012. ISBN: 978-3-642-28026-9. DOI: 10.1007/978-3-642-28027-6 (cit. on p. 9).
- [35] A. Cichocki et al. “Tensor Networks for Dimensionality Reduction and Large-scale Optimization: Part 1 Low-Rank Tensor Decompositions”. In: *Foundations and Trends in Machine Learning* 9 (Jan. 2016), pp. 249–429. DOI: 10.1561/22000000059 (cit. on p. 9).
- [36] A. Cichocki et al. “Tensor Networks for Dimensionality Reduction and Large-scale Optimization: Part 2 Applications and Future Perspectives”. In: *Foundations and Trends in Machine Learning* 9 (Jan. 2016), pp. 431–673. DOI: 10.1561/22000000067 (cit. on p. 9).
- [37] R. J. Baxter. “Dimers on a Rectangular Lattice”. In: *Journal of Mathematical Physics* 9.4 (Apr. 1, 1968). Publisher: American Institute of Physics, pp. 650–654. ISSN: 0022-2488. DOI: 10.1063/1.1664623 (cit. on p. 9).
- [38] M. Fannes, B. Nachtergaele, and R. F. Werner. “Finitely correlated states on quantum spin chains”. In: *Communications in Mathematical Physics* 144.3 (Mar. 1, 1992), pp. 443–490. DOI: <https://doi.org/10.1007/BF02099178> (cit. on p. 9).
- [39] I. Affleck et al. “Rigorous results on valence-bond ground states in antiferromagnets”. In: *Physical Review Letters* 59.7 (Aug. 17, 1987), pp. 799–802. ISSN: 0031-9007. DOI: 10.1103/PhysRevLett.59.799 (cit. on p. 9).
- [40] S. R. White. “Density matrix formulation for quantum renormalization groups”. In: *Physical Review Letters* 69.19 (Nov. 1992), pp. 2863–2866. ISSN: 0031-9007. DOI: 10.1103/PhysRevLett.69.2863 (cit. on p. 9).
- [41] S. R. White. “Density-matrix algorithms for quantum renormalization groups”. In: *Physical Review B* 48.14 (Oct. 1993), pp. 10345–10356. ISSN: 0163-1829, 1095-3795. DOI: 10.1103/PhysRevB.48.10345 (cit. on p. 9).
- [42] S. Östlund and S. Rommer. “Thermodynamic Limit of Density Matrix Renormalization”. In: *Physical Review Letters* 75.19 (Nov. 6, 1995), pp. 3537–3540. ISSN: 0031-9007, 1079-7114. DOI: 10.1103/PhysRevLett.75.3537 (cit. on p. 9).
- [43] F. Verstraete, D. Porras, and J. I. Cirac. “Density Matrix Renormalization Group and Periodic Boundary Conditions: A Quantum Information Perspective”. In: *Physical Review Letters* 93.22 (Nov. 2004), p. 227205. ISSN: 0031-9007, 1079-7114. DOI: 10.1103/PhysRevLett.93.227205 (cit. on p. 9).
- [44] A. J. Daley et al. “Time-dependent density-matrix renormalization-group using adaptive effective Hilbert spaces”. In: *Journal of Statistical Mechanics: Theory and Experiment* 2004.04 (Apr. 2004), P04005. ISSN: 1742-5468. DOI: 10.1088/1742-5468/2004/04/P04005 (cit. on p. 9).

- [45] U. Schollwöck. “The density-matrix renormalization group in the age of matrix product states”. In: *Annals of Physics* 326.1 (Jan. 2011), pp. 96–192. ISSN: 00034916. DOI: 10.1016/j.aop.2010.09.012 (cit. on p. 9).
- [46] S. R. White and A. E. Feiguin. “Real-Time Evolution Using the Density Matrix Renormalization Group”. In: *Physical Review Letters* 93.7 (Aug. 10, 2004). Publisher: American Physical Society, p. 076401. DOI: 10.1103/PhysRevLett.93.076401 (cit. on p. 9).
- [47] G. Vidal. “Efficient Simulation of One-Dimensional Quantum Many-Body Systems”. In: *Physical Review Letters* 93.4 (July 19, 2004), p. 040502. ISSN: 0031-9007, 1079-7114. DOI: 10.1103/PhysRevLett.93.040502 (cit. on pp. 9, 20).
- [48] A. Nüsseler et al. “Efficient simulation of open quantum systems coupled to a fermionic bath”. In: *Physical Review B* 101.15 (Apr. 2020), p. 155134. ISSN: 2469-9950, 2469-9969. DOI: 10.1103/PhysRevB.101.155134 (cit. on p. 9).
- [49] S. Backens, A. Shnirman, and Y. Makhlin. “JordanWigner transformations for tree structures”. In: *Scientific Reports* 9.1 (Dec. 2019), p. 2598. ISSN: 2045-2322. DOI: 10.1038/s41598-018-38128-8 (cit. on p. 9).
- [50] F. Verstraete and J. I. Cirac. “Continuous Matrix Product States for Quantum Fields”. In: *Physical Review Letters* 104.19 (May 14, 2010). Publisher: American Physical Society, p. 190405. DOI: 10.1103/PhysRevLett.104.190405 (cit. on p. 9).
- [51] D. Bauernfeind and M. Aichhorn. “Time Dependent Variational Principle for Tree Tensor Networks”. In: *SciPost Physics* 8.2 (Feb. 7, 2020), p. 024. ISSN: 2542-4653. DOI: 10.21468/SciPostPhys.8.2.024 (cit. on p. 9).
- [52] F. Verstraete and J. I. Cirac. “Renormalization algorithms for Quantum-Many Body Systems in two and higher dimensions”. In: *arXiv:cond-mat/0407066* (July 2, 2004). arXiv: cond-mat/0407066 (cit. on p. 9).
- [53] Z. Li, M. J. O’Rourke, and G. K.-L. Chan. “On the generalization of the exponential basis for tensor network representations of long-range interactions in two and three dimensions”. In: *Physical Review B* 100.15 (Oct. 14, 2019), p. 155121. ISSN: 2469-9950, 2469-9969. DOI: 10.1103/PhysRevB.100.155121 (cit. on p. 9).
- [54] G. Vidal. “Efficient Classical Simulation of Slightly Entangled Quantum Computations”. In: *Physical Review Letters* 91.14 (Oct. 1, 2003), p. 147902. ISSN: 0031-9007, 1079-7114. DOI: 10.1103/PhysRevLett.91.147902 (cit. on p. 11).
- [55] M. Srednicki. “Entropy and area”. In: *Physical Review Letters* 71.5 (Aug. 1993), pp. 666–669. ISSN: 0031-9007. DOI: 10.1103/PhysRevLett.71.666 (cit. on p. 16).
- [56] M. B. Plenio et al. “Entropy, Entanglement, and Area: Analytical Results for Harmonic Lattice Systems”. In: *Physical Review Letters* 94.6 (Feb. 2005), p. 060503. ISSN: 0031-9007, 1079-7114. DOI: 10.1103/PhysRevLett.94.060503 (cit. on p. 16).

- [57] G. Vidal et al. “Entanglement in Quantum Critical Phenomena”. In: *Physical Review Letters* 90.22 (June 2003), p. 227902. ISSN: 0031-9007, 1079-7114. DOI: 10.1103/PhysRevLett.90.227902 (cit. on p. 16).
- [58] S. Paeckel et al. “Time-evolution methods for matrix-product states”. In: *Annals of Physics* 411 (Dec. 2019), p. 167998. ISSN: 00034916. DOI: 10.1016/j.aop.2019.167998 (cit. on pp. 20, 21).
- [59] M. Suzuki. “Generalized Trotter’s formula and systematic approximants of exponential operators and inner derivations with applications to many-body problems”. In: *Communications in Mathematical Physics* 51.2 (1976). Publisher: Springer-Verlag, pp. 183–190. ISSN: 0010-3616, 1432-0916. DOI: 10.1007/BF01609348 (cit. on p. 20).
- [60] F. Verstraete, J. I. Cirac, and J. I. Latorre. “Quantum circuits for strongly correlated quantum systems”. In: *Physical Review A* 79.3 (Mar. 16, 2009). Publisher: American Physical Society, p. 032316. DOI: 10.1103/PhysRevA.79.032316 (cit. on p. 20).
- [61] D. Bauernfeind et al. “Fork Tensor-Product States: Efficient Multiorbital Real-Time DMFT Solver”. In: *Physical Review X* 7.3 (July 20, 2017), p. 031013. ISSN: 2160-3308. DOI: 10.1103/PhysRevX.7.031013 (cit. on p. 20).
- [62] T. Barthel and Y. Zhang. “Optimized Lie-Trotter-Suzuki decompositions for two and three non-commuting terms”. In: *Annals of Physics* 418 (July 2020), p. 168165. ISSN: 00034916. DOI: 10.1016/j.aop.2020.168165 (cit. on p. 20).
- [63] M. P. Zaletel et al. “Time-evolving a matrix product state with long-ranged interactions”. In: *Physical Review B* 91.16 (Apr. 7, 2015), p. 165112. ISSN: 1098-0121, 1550-235X. DOI: 10.1103/PhysRevB.91.165112 (cit. on p. 20).
- [64] Y. Saad. *Iterative Methods for Sparse Linear Systems*. Other Titles in Applied Mathematics. Society for Industrial and Applied Mathematics, Jan. 1, 2003. 537 pp. ISBN: 978-0-89871-534-7. DOI: 10.1137/1.9780898718003 (cit. on p. 21).
- [65] T. J. Park and J. C. Light. “Unitary quantum time evolution by iterative Lanczos reduction”. In: *The Journal of Chemical Physics* 85.10 (Nov. 15, 1986). Publisher: American Institute of Physics, pp. 5870–5876. ISSN: 0021-9606. DOI: 10.1063/1.451548 (cit. on p. 21).
- [66] R. Kosloff. “Time-dependent quantum-mechanical methods for molecular dynamics”. In: *The Journal of Physical Chemistry* 92.8 (Apr. 1, 1988). Publisher: American Chemical Society, pp. 2087–2100. ISSN: 0022-3654. DOI: 10.1021/j100319a003 (cit. on p. 21).
- [67] J. J. García-Ripoll. “Time evolution of Matrix Product States”. In: *New Journal of Physics* 8.12 (Dec. 2006). Publisher: IOP Publishing, pp. 305–305. ISSN: 1367-2630. DOI: 10.1088/1367-2630/8/12/305 (cit. on p. 21).

- [68] P. E. Dargel et al. “Lanczos algorithm with matrix product states for dynamical correlation functions”. In: *Physical Review B* 85.20 (May 11, 2012). Publisher: American Physical Society, p. 205119. DOI: 10.1103/PhysRevB.85.205119 (cit. on p. 21).
- [69] C. Lubich, I. Oseledets, and B. Vandereycken. “Time integration of tensor trains”. In: *SIAM Journal on Numerical Analysis* 53.2 (Jan. 2015), pp. 917–941. ISSN: 0036-1429, 1095-7170. DOI: 10.1137/140976546 (cit. on pp. 21, 22, 24).
- [70] J. Haegeman et al. “Unifying time evolution and optimization with matrix product states”. In: *Physical Review B* 94.16 (Oct. 10, 2016), p. 165116. ISSN: 2469-9950, 2469-9969. DOI: 10.1103/PhysRevB.94.165116 (cit. on pp. 21, 22).
- [71] P. Secular et al. “Parallel time-dependent variational principle algorithm for matrix product states”. In: *Physical Review B* 101.23 (June 5, 2020). Publisher: American Physical Society, p. 235123. DOI: 10.1103/PhysRevB.101.235123 (cit. on pp. 22, 29).
- [72] C. Lubich et al. “Dynamical Approximation by Hierarchical Tucker and Tensor-Train Tensors”. In: *SIAM Journal on Matrix Analysis and Applications* 34.2 (Jan. 1, 2013). Publisher: Society for Industrial and Applied Mathematics, pp. 470–494. ISSN: 0895-4798. DOI: 10.1137/120885723 (cit. on p. 22).
- [73] B. Kloss, D. Reichman, and Y. B. Lev. “Studying dynamics in two-dimensional quantum lattices using tree tensor network states”. In: *SciPost Physics* 9.5 (Nov. 11, 2020), p. 070. ISSN: 2542-4653. DOI: 10.21468/SciPostPhys.9.5.070 (cit. on p. 22).
- [74] S. Goto and I. Danshita. “Performance of the time-dependent variational principle for matrix product states in long-time evolution of a pure state”. In: *Physical Review B* 99.5 (Feb. 2019), p. 054307. ISSN: 2469-9950, 2469-9969. DOI: 10.1103/PhysRevB.99.054307 (cit. on p. 29).
- [75] E. Leviatan et al. “Quantum thermalization dynamics with Matrix-Product States”. In: *arXiv:1702.08894 [cond-mat, physics:quant-ph]* (Oct. 2017). arXiv: 1702.08894 (cit. on p. 29).
- [76] W. Li, J. Ren, and Z. Shuai. “Numerical Assessment for Accuracy and GPU Acceleration of TD-DMRG Time Evolution Schemes”. In: *The Journal of Chemical Physics* 152.2 (Jan. 14, 2020), p. 024127. ISSN: 0021-9606, 1089-7690. DOI: 10.1063/1.5135363 (cit. on p. 29).
- [77] A. W. Chin et al. “Exact mapping between system-reservoir quantum models and semi-infinite discrete chains using orthogonal polynomials”. In: *Journal of Mathematical Physics* 51.9 (Sept. 2010), p. 092109. ISSN: 0022-2488, 1089-7658. DOI: 10.1063/1.3490188 (cit. on pp. 33, 38).
- [78] M. P. Woods, M. Cramer, and M. B. Plenio. “Simulating Bosonic Baths with Error Bars”. In: *Physical Review Letters* 115.13 (Sept. 2015), p. 130401. ISSN: 0031-9007, 1079-7114. DOI: 10.1103/PhysRevLett.115.130401 (cit. on p. 34).

- [79] J. Prior et al. “Efficient Simulation of Strong System-Environment Interactions”. In: *Physical Review Letters* 105.5 (July 30, 2010). Publisher: American Physical Society, p. 050404. DOI: 10.1103/PhysRevLett.105.050404 (cit. on p. 34).
- [80] F. Verstraete, J. J. García-Ripoll, and J. I. Cirac. “Matrix Product Density Operators: Simulation of Finite-Temperature and Dissipative Systems”. In: *Physical Review Letters* 93.20 (Nov. 12, 2004), p. 207204. ISSN: 0031-9007, 1079-7114. DOI: 10.1103/PhysRevLett.93.207204 (cit. on p. 35).
- [81] A. E. Feiguin and S. R. White. “Finite-temperature density matrix renormalization using an enlarged Hilbert space”. In: *Physical Review B* 72.22 (Dec. 2, 2005), p. 220401. ISSN: 1098-0121, 1550-235X. DOI: 10.1103/PhysRevB.72.220401 (cit. on p. 35).
- [82] S. Goto and I. Danshita. “Cooling schemes for two-component fermions in layered optical lattices”. In: *Physical Review A* 96.6 (Dec. 1, 2017). Publisher: American Physical Society, p. 063602. DOI: 10.1103/PhysRevA.96.063602 (cit. on p. 35).
- [83] S. R. White. “Minimally Entangled Typical Quantum States at Finite Temperature”. In: *Physical Review Letters* 102.19 (May 11, 2009), p. 190601. ISSN: 0031-9007, 1079-7114. DOI: 10.1103/PhysRevLett.102.190601 (cit. on p. 35).
- [84] E. M. Stoudenmire and S. R. White. “Minimally Entangled Typical Thermal State Algorithms”. In: *New Journal of Physics* 12.5 (May 28, 2010), p. 055026. ISSN: 1367-2630. DOI: 10.1088/1367-2630/12/5/055026 (cit. on p. 35).
- [85] S. Goto and I. Danshita. “Minimally entangled typical thermal states algorithm with Trotter gates”. In: *Physical Review Research* 2.4 (Nov. 13, 2020). Publisher: American Physical Society, p. 043236. DOI: 10.1103/PhysRevResearch.2.043236 (cit. on p. 35).
- [86] D. Tamascelli. “Excitation Dynamics in Chain-Mapped Environments”. In: *Entropy* 22.11 (Nov. 2020). Number: 11 Publisher: Multidisciplinary Digital Publishing Institute, p. 1320. DOI: 10.3390/e22111320 (cit. on p. 36).
- [87] D. Tamascelli et al. “Efficient simulation of finite-temperature open quantum systems”. In: *Physical Review Letters* 123.9 (Aug. 2019). arXiv: 1811.12418, p. 090402. ISSN: 0031-9007, 1079-7114. DOI: 10.1103/PhysRevLett.123.090402 (cit. on pp. 36, 39).
- [88] M. P. Woods et al. “Mappings of open quantum systems onto chain representations and Markovian embeddings”. In: *Journal of Mathematical Physics* 55.3 (Mar. 2014), p. 032101. ISSN: 0022-2488, 1089-7658. DOI: 10.1063/1.4866769 (cit. on p. 39).
- [89] I. de Vega and M.-C. Bañuls. “Thermofield-based chain-mapping approach for open quantum systems”. In: *Physical Review A* 92.5 (Nov. 2015), p. 052116. ISSN: 1050-2947, 1094-1622. DOI: 10.1103/PhysRevA.92.052116 (cit. on p. 39).

- [90] C. Hubig, I. P. McCulloch, and U. Schollwöck. “Generic Construction of Efficient Matrix Product Operators”. In: *Physical Review B* 95.3 (Jan. 2017). arXiv: 1611.02498, p. 035129. ISSN: 2469-9950, 2469-9969. DOI: 10.1103/PhysRevB.95.035129 (cit. on p. 40).
- [91] M. Fishman, S. R. White, and E. M. Stoudenmire. *The ITensor Software Library for Tensor Network Calculations*. 2020. arXiv: 2007.14822 (cit. on pp. 40, 120).
- [92] A. J. Dunnett. *angusdunnett/MPSDynamics*: version v1.0. July 2021. DOI: 10.5281/zenodo.5106435 (cit. on pp. 42, 109, 120).
- [93] J. Haegeman et al. *Jutho/TensorOperations.jl: v1.1.0*. Version v1.1.0. June 2019. DOI: 10.5281/zenodo.3245497 (cit. on p. 42).
- [94] W. Gautschi. “Algorithm 726: ORTHPOL a package of routines for generating orthogonal polynomials and Gauss-type quadrature rules”. In: *ACM Transactions on Mathematical Software* 20.1 (Mar. 1994), pp. 21–62. ISSN: 0098-3500, 1557-7295. DOI: 10.1145/174603.174605 (cit. on pp. 45, 120).
- [95] A. J. Leggett. “Dynamics of the dissipative two-state system”. In: *Reviews of Modern Physics* 59.1 (1987), pp. 1–85. DOI: 10.1103/RevModPhys.59.1 (cit. on pp. 50, 57).
- [96] R. Silbey and R. A. Harris. “Variational calculation of the dynamics of a two level system interacting with a bath”. In: *The Journal of Chemical Physics* 80.6 (Mar. 1984), pp. 2615–2617. ISSN: 0021-9606, 1089-7690. DOI: 10.1063/1.447055 (cit. on pp. 52, 69).
- [97] Z. Blunden-Codd et al. “Anatomy of quantum critical wave functions in dissipative impurity problems”. In: *Physical Review B* 95.8 (Feb. 2017). Publisher: American Physical Society, p. 085104. DOI: 10.1103/PhysRevB.95.085104 (cit. on p. 53).
- [98] S. Florens et al. “Dissipative spin dynamics near a quantum critical point: Numerical renormalization group and Majorana diagrammatics”. In: *Physical Review B* 84.15 (Oct. 2011). Publisher: American Physical Society, p. 155110. DOI: 10.1103/PhysRevB.84.155110 (cit. on p. 53).
- [99] B. Bruognolo et al. “Two-bath spin-boson model: Phase diagram and critical properties”. In: *Physical Review B* 90.24 (Dec. 2014), p. 245130. ISSN: 1098-0121, 1550-235X. DOI: 10.1103/PhysRevB.90.245130 (cit. on pp. 53, 63).
- [100] S. Barnett and P. Radmore. *Methods in Theoretical Quantum Optics*. Oxford Series in Optical and Imaging Sciences. Oxford: Oxford University Press, 2002. ISBN: 978-0-19-856361-7. DOI: 10.1093/acprof:oso/9780198563617.001.0001 (cit. on pp. 54, 55).
- [101] A. W. Chin and A. J. Dunnett. *Real-time benchmark dynamics of the Ohmic Spin-Boson Model computed with Time-Dependent Variational Matrix Product States. (TDVMPS) coupling strength and temperature parameter space*. Dec. 2020. DOI: 10.5281/zenodo.4352729 (cit. on p. 57).

- [102] A. J. Dunnett and A. W. Chin. “Matrix Product State Simulations of Non-Equilibrium Steady States and Transient Heat Flows in the Two-Bath Spin-Boson Model at Finite Temperatures”. In: *Entropy* 23.1 (Jan. 2021). Number: 1 Publisher: Multidisciplinary Digital Publishing Institute, p. 77. DOI: 10.3390/e23010077 (cit. on pp. 57, 63).
- [103] D. Devault. “Quantum mechanical tunnelling in biological systems”. In: *Quarterly Reviews of Biophysics* 13.4 (Nov. 1980). Publisher: Cambridge University Press, pp. 387–564. ISSN: 1469-8994, 0033-5835. DOI: 10.1017/S003358350000175X (cit. on p. 58).
- [104] R. A. Marcus. “Electron transfer reactions in chemistry. Theory and experiment”. In: *Reviews of Modern Physics* 65.3 (July 1993), pp. 599–610. ISSN: 0034-6861, 1539-0756. DOI: 10.1103/RevModPhys.65.599 (cit. on p. 58).
- [105] V. May and O. Kühn. *Charge and energy transfer dynamics in molecular systems*. Weinheim; Chichester: Wiley-VCH ; John Wiley distributor, 2011. ISBN: 978-3-527-63379-1 978-3-527-63380-7. DOI: 10.1002/9783527633791 (cit. on p. 58).
- [106] A. J. Dunnett and A. W. Chin. *Exact Spin-Boson-Model Tunneling Dynamics with Time Dependent Variation Matrix Product States (TDVMPS). Barrier height and temperature parameter space*. Jan. 2021. DOI: 10.5281/zenodo.4432015 (cit. on p. 63).
- [107] A. J. Dunnett and A. W. Chin. “Simulating Quantum Vibronic Dynamics at Finite Temperatures With Many Body Wave Functions at 0 K”. In: *Frontiers in Chemistry* 8 (2021). Publisher: Frontiers. ISSN: 2296-2646. DOI: 10.3389/fchem.2020.600731 (cit. on pp. 63, 71).
- [108] G. Benenti et al. “Fundamental aspects of steady-state conversion of heat to work at the nanoscale”. In: *Physics Reports*. Fundamental aspects of steady-state conversion of heat to work at the nanoscale 694 (June 2017), pp. 1–124. ISSN: 0370-1573. DOI: 10.1016/j.physrep.2017.05.008 (cit. on p. 63).
- [109] Y. Dubi and M. Di Ventra. “Colloquium : Heat flow and thermoelectricity in atomic and molecular junctions”. In: *Reviews of Modern Physics* 83.1 (Mar. 2011), pp. 131–155. ISSN: 0034-6861, 1539-0756. DOI: 10.1103/RevModPhys.83.131 (cit. on p. 63).
- [110] A. Dhar. “Heat transport in low-dimensional systems”. In: *Advances in Physics* 57.5 (Sept. 2008), pp. 457–537. ISSN: 0001-8732, 1460-6976. DOI: 10.1080/00018730802538522 (cit. on p. 63).
- [111] C. Guo et al. “Critical and Strong-Coupling Phases in One- and Two-Bath Spin-Boson Models”. In: *Physical Review Letters* 108.16 (Apr. 2012), p. 160401. ISSN: 0031-9007, 1079-7114. DOI: 10.1103/PhysRevLett.108.160401 (cit. on pp. 63, 72).
- [112] N. Zhou et al. “Symmetry and the critical phase of the two-bath spin-boson model: Ground-state properties”. In: *Physical Review B* 91.19 (May 2015), p. 195129. ISSN: 1098-0121, 1550-235X. DOI: 10.1103/PhysRevB.91.195129 (cit. on p. 63).

- [113] D. Segal and A. Nitzan. “Spin-Boson Thermal Rectifier”. In: *Physical Review Letters* 94.3 (Jan. 2005), p. 034301. ISSN: 0031-9007, 1079-7114. DOI: 10.1103/PhysRevLett.94.034301 (cit. on p. 63).
- [114] T. Chen et al. “Steady-state quantum transport through an anharmonic oscillator strongly coupled to two heat reservoirs”. In: *Physical Review E* 102.1 (July 31, 2020). Publisher: American Physical Society, p. 012155. DOI: 10.1103/PhysRevE.102.012155 (cit. on p. 63).
- [115] S. Mukamel. *Principles of Nonlinear Optical Spectroscopy*. Vol. 6. New York, NY: Oxford University Press, 1995 (cit. on p. 75).
- [116] A. D. Somoza et al. “Dissipation-Assisted Matrix Product Factorization”. In: *Physical Review Letters* 123.10 (Sept. 2019). Publisher: American Physical Society, p. 100502. DOI: 10.1103/PhysRevLett.123.100502 (cit. on p. 75).
- [117] M. F. Gelin and R. Borrelli. “Simulation of Nonlinear Femtosecond Signals at Finite Temperature via a Thermo Field Dynamics-Tensor Train Method: General Theory and Application to Time- and Frequency-Resolved Fluorescence of the Fenna Matthews Olson Complex”. In: *Journal of Chemical Theory and Computation* 17.7 (July 2021), pp. 4316–4331. ISSN: 1549-9618, 1549-9626. DOI: 10.1021/acs.jctc.1c00158 (cit. on pp. 77, 95).
- [118] D. Heger, J. Jirkovský, and P. Klán. “Aggregation of methylene blue in frozen aqueous solutions studied by absorption spectroscopy”. In: *The Journal of Physical Chemistry. A* 109.30 (Aug. 4, 2005), pp. 6702–6709. ISSN: 1089-5639. DOI: 10.1021/jp050439j (cit. on p. 77).
- [119] O. V. Ovchinnikov et al. “Manifestation of intermolecular interactions in FTIR spectra of methylene blue molecules”. In: *Vibrational Spectroscopy* C.86 (2016), pp. 181–189. ISSN: 0924-2031. DOI: 10.1016/j.vibspec.2016.06.016 (cit. on p. 77).
- [120] G. A. Shahinyan, A. Y. Amirbekyan, and S. A. Markarian. “Photophysical properties of methylene blue in water and in aqueous solutions of dimethylsulfoxide”. In: *Spectrochimica Acta Part A: Molecular and Biomolecular Spectroscopy* 217 (June 15, 2019), pp. 170–175. ISSN: 1386-1425. DOI: 10.1016/j.saa.2019.03.079 (cit. on p. 78).
- [121] J. C. Dean et al. “Broadband Transient Absorption and Two-Dimensional Electronic Spectroscopy of Methylene Blue”. In: *The Journal of Physical Chemistry A* 119.34 (Aug. 27, 2015), pp. 9098–9108. ISSN: 1089-5639, 1520-5215. DOI: 10.1021/acs.jpca.5b06126 (cit. on p. 78).
- [122] T. B. de Queiroz et al. “First principles theoretical spectroscopy of methylene blue: Between limitations of time-dependent density functional theory approximations and its realistic description in the solvent”. In: *The Journal of Chemical Physics* 154.4 (Jan. 28, 2021). Publisher: American Institute of Physics, p. 044106. ISSN: 0021-9606. DOI: 10.1063/5.0029727 (cit. on p. 78).

- [123] A. J. Dunnett et al. "Influence of non-adiabatic effects on linear absorption spectra in the condensed phase: Methylene blue". In: *The Journal of Chemical Physics* 155.14 (Oct. 2021). Publisher: American Institute of Physics, p. 144112. ISSN: 0021-9606. DOI: 10.1063/5.0062950 (cit. on pp. 78, 84, 92–94).
- [124] T. J. Zuehlsdorff et al. "Optical spectra in the condensed phase: Capturing anharmonic and vibronic features using dynamic and static approaches". In: *The Journal of Chemical Physics* 151.7 (Aug. 21, 2019), p. 074111. ISSN: 0021-9606, 1089-7690. DOI: 10.1063/1.5114818 (cit. on p. 79).
- [125] S. A. Egorov, K. F. Everitt, and J. L. Skinner. "Quantum Dynamics and Vibrational Relaxation". In: *The Journal of Physical Chemistry A* 103.47 (Nov. 1999), pp. 9494–9499. ISSN: 1089-5639, 1520-5215. DOI: 10.1021/jp9919314 (cit. on p. 80).
- [126] J. S. Bader and B. J. Berne. "Quantum and classical relaxation rates from classical simulations". In: *The Journal of Chemical Physics* 100.11 (June 1, 1994). Publisher: American Institute of Physics, pp. 8359–8366. ISSN: 0021-9606. DOI: 10.1063/1.466780 (cit. on p. 80).
- [127] H. Kim and P. J. Rossky. "Evaluation of Quantum Correlation Functions from Classical Data". In: *The Journal of Physical Chemistry B* 106.33 (Aug. 1, 2002). Publisher: American Chemical Society, pp. 8240–8247. ISSN: 1520-6106. DOI: 10.1021/jp020669n (cit. on p. 80).
- [128] G. R. Medders et al. "Ultrafast Electronic Relaxation through a Conical Intersection: Nonadiabatic Dynamics Disentangled through an Oscillator Strength-Based Diabatization Framework". In: *The journal of physical chemistry. A* 121.7 (Feb. 2017), pp. 1425–1434. ISSN: 1089-5639. DOI: 10.1021/acs.jpca.6b12120 (cit. on p. 82).
- [129] I. S. Ufimtsev and T. J. Martinez. "Quantum Chemistry on Graphical Processing Units. 3. Analytical Energy Gradients, Geometry Optimization, and First Principles Molecular Dynamics". In: *Journal of Chemical Theory and Computation* 5.10 (Oct. 13, 2009). Publisher: American Chemical Society, pp. 2619–2628. ISSN: 1549-9618. DOI: 10.1021/ct9003004 (cit. on p. 83).
- [130] P. Eastman et al. "OpenMM 7: Rapid development of high performance algorithms for molecular dynamics". In: *PLoS computational biology* 13.7 (July 2017), e1005659. ISSN: 1553-7358. DOI: 10.1371/journal.pcbi.1005659 (cit. on p. 83).
- [131] W. L. Jorgensen et al. "Comparison of simple potential functions for simulating liquid water". In: *The Journal of Chemical Physics* 79.2 (July 15, 1983). Publisher: American Institute of Physics, pp. 926–935. ISSN: 0021-9606. DOI: 10.1063/1.445869 (cit. on p. 83).
- [132] J. T. Horton et al. "QUBEKit: Automating the Derivation of Force Field Parameters from Quantum Mechanics". In: *Journal of Chemical Information and Modeling* 59.4 (Apr. 22, 2019), pp. 1366–1381. ISSN: 1549-960X. DOI: 10.1021/acs.jcim.8b00767 (cit. on p. 83).

- [133] T. Yanai, D. P. Tew, and N. C. Handy. “A new hybrid exchange-correlation functional using the Coulomb-attenuating method (CAM-B3LYP)”. In: *Chemical Physics Letters* 393.1 (July 21, 2004), pp. 51–57. ISSN: 0009-2614. DOI: 10.1016/j.cplett.2004.06.011 (cit. on p. 83).
- [134] C. M. Isborn et al. “Excited-State Electronic Structure with Configuration Interaction Singles and TammDancoff Time-Dependent Density Functional Theory on Graphical Processing Units”. In: *Journal of Chemical Theory and Computation* 7.6 (June 14, 2011), pp. 1814–1823. ISSN: 1549-9618, 1549-9626. DOI: 10.1021/ct200030k (cit. on p. 83).
- [135] P. J. Stephens et al. “Ab Initio Calculation of Vibrational Absorption and Circular Dichroism Spectra Using Density Functional Force Fields”. In: *The Journal of Physical Chemistry* 98.45 (Nov. 1, 1994). Publisher: American Chemical Society, pp. 11623–11627. ISSN: 0022-3654. DOI: 10.1021/j100096a001 (cit. on p. 83).
- [136] T. J. Zuehlsdorff et al. “Influence of Electronic Polarization on the Spectral Density”. In: *The Journal of Physical Chemistry B* 124.3 (Jan. 23, 2020). Publisher: American Chemical Society, pp. 531–543. ISSN: 1520-6106. DOI: 10.1021/acs.jpccb.9b10250 (cit. on p. 83).
- [137] A. Fernández-Pérez, T. Valdés-Solís, and G. Marbán. “Visible light spectroscopic analysis of Methylene Blue in water; the resonance virtual equilibrium hypothesis”. In: *Dyes and Pigments* 161 (Feb. 2019), pp. 448–456. ISSN: 0143-7208. DOI: 10.1016/j.dyepig.2018.09.083 (cit. on p. 91).
- [138] A. J. Dunnett and A. W. Chin. “Efficient bond-adaptive approach for finite-temperature open quantum dynamics using the one-site time-dependent variational principle for matrix product states”. In: *Phys. Rev. B* 104 (21 Dec. 2021), p. 214302. DOI: 10.1103/PhysRevB.104.214302 (cit. on pp. 101, 102).
- [139] M. Yang and S. R. White. “Time-dependent variational principle with ancillary Krylov subspace”. In: *Physical Review B* 102.9 (Sept. 2020). Publisher: American Physical Society, p. 094315. DOI: 10.1103/PhysRevB.102.094315 (cit. on pp. 101, 115).
- [140] V. Zauner-Stauber et al. “Variational optimization algorithms for uniform matrix product states”. In: *Physical Review B* 97.4 (Jan. 25, 2018), p. 045145. ISSN: 2469-9950, 2469-9969. DOI: 10.1103/PhysRevB.97.045145. arXiv: 1701.07035 (cit. on p. 101).
- [141] C. Hubig et al. “Strictly single-site DMRG algorithm with subspace expansion”. In: *Physical Review B* 91.15 (Apr. 2015), p. 155115. ISSN: 1098-0121, 1550-235X. DOI: 10.1103/PhysRevB.91.155115 (cit. on pp. 102, 105).
- [142] U. Manthe. “The multi-configurational time-dependent Hartree approach revisited”. In: *The Journal of Chemical Physics* 142.24 (June 28, 2015). Publisher: American Institute of Physics, p. 244109. ISSN: 0021-9606. DOI: 10.1063/1.4922889 (cit. on p. 112).

- [143] C. Lubich. “Time Integration in the Multiconfiguration Time-Dependent Hartree Method of Molecular Quantum Dynamics”. In: *Applied Mathematics Research eXpress* 2015.2 (2015), pp. 311–328. ISSN: 1687-1200, 1687-1197. DOI: 10.1093/amrx/abv006 (cit. on p. 112).
- [144] J. Hauschild and F. Pollmann. “Efficient numerical simulations with Tensor Networks: Tensor Network Python (TeNPy)”. In: *SciPost Phys. Lect. Notes* (2018). Code available from <https://github.com/tenpy/tenpy>, p. 5. DOI: 10.21468/SciPostPhysLectNotes.5. arXiv: 1805.00055 (cit. on p. 120).

Sujet : Décrire les systèmes quantiques ouverts à température non-nulle à l'aide de Réseaux de Tenseurs avec application à la Spectroscopie

Résumé : Comprendre la décohérence et la dissipation dans les systèmes quantiques est essentiel pour exploiter les effets quantiques dans les applications technologiques émergentes. Une bonne compréhension nécessite une modélisation précise de l'interaction entre l'environnement et le système qui ne peut être obtenue qu'en traitant ceux-ci sur un pied d'égalité. Simuler la fonction d'onde entière du système+environnement est une tâche difficile en raison de la croissance exponentielle de l'espace de Hilbert qui est caractéristique de la mécanique quantique. En utilisant des méthodes à plusieurs corps basées sur le concept puissant de réseaux de tenseurs, on peut, néanmoins, obtenir une dynamique quantique numériquement exacte pour des systèmes avec des centaines de degrés de liberté. De plus, une innovation récente a montré que cette approche à plusieurs corps peut être étendue à des températures non-nulle sans augmentation du coût de calcul ou de la complexité algorithmique. Cela nous a permis de comparer directement les simulations dynamiques quantiques avec des résultats expérimentaux. Plus précisément, des simulations de l'hamiltonien de couplage vibronique linéaire, paramétrés à l'aide de méthodes de structure électronique ab initio, ont été utilisés pour calculer le spectre d'absorption du colorant Méthylène bleu dans l'eau. Cette étude a élucidé certaines caractéristiques inexplicables de l'absorption et a montré comment la dynamique non-adiabatique résultant d'une intersection conique peut conduire à des emprunts d'intensité entre et les états excités brillant et sombres. Plusieurs avancées méthodologiques sont également réalisées, dont une amélioration de la méthode d'évolution temporelle TDVP qui apporte un ordre de grandeur d'accélération par rapport aux méthodes existantes.

Mots clés : Systèmes quantique ouverts, Réseaux de Tenseurs

Subject : Tensor Network approaches to Open Quantum Systems at Finite Temperature with applications to Spectroscopy

Abstract: Understanding decoherence and dissipation in quantum systems is essential for exploiting quantum effects in emerging technological applications. A proper understanding requires accurate modelling of the system-environment interaction which can only be achieved through treating the system and environment on an equal footing. Simulating the entire system+environment wave-function is a challenging task due to the exponential scaling which is characteristic of quantum mechanics. By using many-body methods based on the powerful concept of a tensor network, one can, nonetheless, obtain numerically exact quantum dynamics for systems with hundreds of degrees of freedom. In addition, a recent innovation has shown that this many-body approach can be extended to finite temperatures without a significant increase in computational cost or algorithmic complexity. This has allowed us to directly compare quantum dynamical simulations with experimental results. Specifically, simulations of the linear vibronic coupling Hamiltonian, parameterised using ab initio electronic structure methods, were used to compute the absorption spectrum of the dye Methylene blue in water. This study has elucidated certain unexplained features of the absorption and shown the how non-adiabatic dynamics resulting from a conical intersection can lead to intensity borrowing between bright and dark excited states. Several methodological advances are also made, including an improvement to the underlying time evolution method TDVP which brings with it an order of magnitude speed-up compared to existing methods.

Keywords : Open Quantum Systems, Tensor Networks